

Terahertz Spectroscopy of Individual Single-Walled Carbon Nanotubes
as a Probe of Luttinger Liquid Physics

A Dissertation
Presented to the Faculty of the Graduate School
of
Yale University
in Candidacy for the Degree of
Doctor of Philosophy

by
Joel David Chudow

Dissertation Director: Professor Daniel E. Prober

December 2014

© 2015 by Joel David Chudow
All rights reserved.

Abstract

Terahertz Spectroscopy of Individual Single-Walled Carbon Nanotubes as a Probe of Luttinger Liquid Physics

Joel David Chudow

2014

Carbon nanotubes are attractive candidates for diverse applications due to their unique electrical, chemical, thermal and mechanical properties. They also serve as a prototypical experimental system for verification of fundamental one-dimensional (1D) conduction models. For a 1D conductor, Luttinger liquid theory predicts collective electron excitations due to strong electron-electron interactions, resulting in a modification of the propagation velocity in the system. We present a high-frequency circuit model for an individual metallic single-walled carbon nanotubes and describe how studying the frequency-dependent terahertz (THz) absorption of the nanotube can probe this expected 1D behavior. We report on measurements of THz absorption in a carbon nanotube, distinguishing between two response mechanisms: bolometric detection due to heating a nanotube with a temperature-dependent resistance, and the response due to non-thermal electrical contact nonlinearities. The effect of the contact nonlinearity is not significantly decreased at THz frequencies, allowing for analysis of the parallel contact capacitance to an individual nanotube. By exploiting this nonlinear detection mechanism, we excite and observe THz standing wave charge resonances along the length of a nanotube and test predictions of the Luttinger liquid model.

Acknowledgements

The importance of collaboration in scientific research cannot be overstated, and it is my pleasure to acknowledge the contributions of others to this work. Not every individual who had an impact on my progress is named explicitly, but I appreciate the help each has given me throughout this journey.

First and foremost I would like to thank my advisor, Daniel Prober, whose ideas formed the basis for this work. He has provided continuous support during my studies as well as professional and personal advice on a great range of topics. I admire his passion for science education and enthusiasm for collaboration. I am grateful for his instructive comments, which guided the direction of the project, and his intuitive insights have been an inspiration through the years. I also value the energy Dan invested in my development beyond our research, encouraging me to pursue outside opportunities and engaging with me on issues of mutual interest.

I want to express immense gratitude to Daniel Santavicca, who has been an incredible colleague. I thank him for remaining in Prober Lab as a post-doc, offering me the opportunity to continue learning from him. His meticulousness, willingness to explain, and mentorship have been invaluable. Daniel has always made himself readily available with constructive advice on any subject and has been a phenomenal resource.

I thank all of the other members of the Prober Lab with whom I had the pleasure to work over the years, including Anthony Annunziata, Chris McKitterick, Faustin Carter, Luigi Frunzio, Zoe Pham-Jackel, Briana Jewczyn, Scott Jones, Danti Chen, Yan

Yin, Veronica Savu, and Matthew Reese, as well as officemate Archana Kamal. I want to thank our visiting researchers Aviad Frydman, Misha Reznikov, Bertrand Reulet, and Venkat Chandrasekhar for the insight they shared during their visits. Thank you to Mike Rooks, the Yale Institute of Nanoscience and Quantum Engineering, and the Yale Center for Microelectronic Materials and Structures for facilitating the device fabrication. This research was made possible by funding from the National Science Foundation and Yale University.

Outside of our lab, I have benefited from the phenomenal grouping of people, knowhow, and the unique atmosphere present on the fourth floor of Becton Center with the groups of Michel Devoret and Robert Schoelkopf. In particular, I thank Markus Brink for generously teaching me much about nanotube nanofabrication. This work also benefited from numerous other Yale collaborations. Thanks especially to the group of Charles Schmuttenmaer in the Chemistry Department for sharing their knowledge of terahertz spectroscopy and to the group of Lisa Pfefferle in Chemical Engineering for sharing in new material development.

Beyond Yale, I want to especially thank and acknowledge Philip Kim at Columbia University, for generously giving me my start in experimental condensed matter physics as an undergraduate when I had no background in the field, and then for continuing his support through our close partnership during my graduate studies, which provided the foundation for this work. Thanks to Meninder Purewal for providing samples and for giving me an introduction to carbon nanotube synthesis. I appreciate the efforts of all the members of the Columbia team who helped me over the years with the nanotube growth.

I thank the departmental administrators Maria Rao, Giselle Devito, Cara Gibilisco, Terri Evangeliste and Devon Cimini who provided the logistics to make this work possible. I thank the members of my committee, Victor Henrich, Charles Schmuttenmaer and outside reader Sigfrid Yngvesson for their careful reading of this dissertation. Finally, I owe all my accomplishments to my friends and family who have helped make me the person I am. Thanks to my friends, especially Samuel Graff and Avi Perez, who cheered me along the way. I thank my wife Rochel and entire family for being a constant source of love and encouragement, and especially my beloved daughter Ahuva who has been a recent inspiration.

Table of Contents

1 Introduction to Electron Transport in Single-Walled Carbon Nanotubes		
1.1	Reduced Dimensionality	1
1.2	The Many Forms of Carbon	2
1.2.1	Carbon Nanotubes	4
1.2.2	Electronic Band Structure of Carbon Nanotubes	7
1.2.3	Electron Transport in Carbon Nanotubes	12
1.3	One-Dimensional Nature	15
1.3.1	Quantum of Resistance	17
1.4	Metal-Nanotube Interface	19
1.5	Electron Mean-Free Path in Nanotubes	21
1.6	Summary	25
1.7	Overview of this dissertation	26
2 High-Frequency Luttinger Liquid Excitations in Carbon Nanotubes		
2.1	High-Frequency Applications	28
2.2	Luttinger Liquid Theory	29
2.2.1	Power-Law Suppression of Tunneling	30
2.2.2	Power-Law Measurement Results	37
2.2.3	Plasmon Velocity	40

2.3	Transmission Line Model of a Carbon Nanotube	41
2.3.1	Transmission Line Model	42
2.3.2	Electrostatic Capacitance	43
2.3.3	Quantum Capacitance	43
2.3.4	Magnetic and Kinetic Inductance	46
2.3.5	Four Parallel Channels	48
2.3.6	Contact Resistance and Capacitance	49
2.3.7	Intrinsic Impedance	50
2.3.8	Plasmon Velocity and Characteristic Impedance	52
2.3.9	Standing Wave Resonances	53
2.3.10	Microwave test of v_p	55
2.4	Terahertz Time-Domain Measurement	56
2.5	Summary	60
3	Device Fabrication	
3.1	Fabrication Overview	61
3.2	Carbon Nanotube Device Fabrication	62
3.3	Silicon Substrate	64
3.4	Alignment Marks	65
3.5	Carbon Nanotube Synthesis	67
3.5.1	Carbon Nanotube Synthesis Parameters	69
3.5.2	Methane Growth	73
3.5.3	Ethanol Growth	76
3.5.4	Chirality Selection	77

3.6	SEM Imaging	79
3.6.1	SEM Contamination	85
3.7	Fiducial Mark Array	86
3.8	Lithography	90
3.9	Metal Contacts	93
3.10	Planar Antenna	94
3.11	Suspended Nanotubes	95
3.12	dc Characterization	97
3.13	Electrostatic Discharge Damage and Device Yield	99
3.14	Summary	101
4	THz Measurement Setup	
4.1	THz Regime	103
4.2	Carbon Nanotubes at THz	106
4.3	THz Measurement Setup	107
4.3.1	Spectrometer	107
4.3.2	Quasi-Optical Coupling	113
4.3.3	Planar Antennas	115
4.3.4	THz radiation source	117
4.4	Superconducting Bolometer as Normalization	120
4.5	Summary	121
5	Carbon Nanotube THz Detection Mechanisms	
5.1	Introduction	123
5.2	Detection Mechanisms	123

5.2.1	Bolometric Detection	124
5.2.2	Nonlinear Detection	126
5.3	Temperature Dependent Behavior	127
5.3.1	Thermal Conductance	127
5.4	Zero-Bias Anomaly	132
5.5	rf Detection	133
5.6	THz Detection	136
5.6.1	THz Responsivity	143
5.7	Estimation of Contact Capacitance	145
5.8	Summary	146
6	Terahertz Spectral Response of Individual Single-walled Carbon Nanotubes	
6.1	Introduction	148
6.2	Background Spectral Response	149
6.3	Carbon Nanotube Device Interferogram	151
6.3.1	Noise in Carbon Nanotubes	151
6.4	Expected Response	155
6.4.1	Spectral Response Results	159
6.5	Beyond the Luttinger Liquid Picture	170
6.6	Conclusions and Future Work	174
	Bibliography	179

List of Figures

1.1	Family of carbon structures	5
1.2	Chart of carbon nanotube chirality	9
1.3	Cartoon of rolling up a graphene sheet	11
1.4	Conductance as a function of gate voltage	14
1.5	Length dependence of resistance	23
2.1	Power-law dependence plot from literature	34
2.2	Fitting power-law dependence curves	39
2.3	Transmission line model of carbon nanotube	45
2.4	Equivalent circuit model for carbon nanotube	51
2.5	Predicted THz frequency dependent impedance	51
2.6	Time-domain THz measurement results	57
3.1	Illustration of carbon nanotube growth mechanism	70
3.2	SEM micrographs of carbon nanotubes produced by methane growth	75
3.3	SEM micrographs of CVD growth from Muller catalyst	78
3.4	SEM micrographs under different conditions	87
3.5	Fiducial marker array pattern	89
3.6	SEM micrograph of fiducial marker array	89
3.7	AFM imaging of individual carbon nanotubes	91

3.8	Optical/SEM micrographs of antenna-coupled carbon nanotube devices	91
3.9	SEM micrographs of log-spiral antenna devices with plasma etching	96
3.10	SEM micrographs of suspended nanotube devices	98
3.11	SEM micrographs of nanotube devices before and after breakdown	100
4.1	Electromagnetic spectrum highlighting THz gap	105
4.2	Schematic FTIR system	105
4.3	Interferogram and spectral response of antenna geometries	110
4.4	Illustration of quasi-optical coupling scheme	110
4.5	Globar output temperature as a function of applied voltage	118
4.6	Equivalent circuit model of antenna-coupled carbon nanotube device	118
5.1	Resistance as a function temperature	129
5.2	Electron temperature as a function of bias current	129
5.3	Thermal conductance as a function of electron temperature	129
5.4	Responsivity as a function of bias current	135
5.5	THz response as a function of time	135
5.6	Resistance as a function of bias current	138
5.7	Measured THz response as a function of bias current	138
5.8	Characteristics of sample NT-B	142
5.9	Determination of C_c	142
6.1	Predicted spectral response	150
6.2	Contour plot of THz response with varying bias conditions	154
6.3	Interferogram and THz response over time	154
6.4	Simulation comparing symmetric and antisymmetric voltage source	158

6.5	Interferogram and spectral response of NT-2	160
6.6	Spectral response of NT-4	164
6.7	Spectral response of NT-5	165
6.8	Spectral response of NT-6	165
6.9	Spectral response of NT-7	167
6.10	Spectral response of NT-8	167
6.11	Frequency spacing as a function of inverse length for devices studied	169

List of Tables

2.1	Luttinger parameter g values reported in literature	36
5.1	Summary of THz detection sample characteristics	144
6.1	Summary of THz spectral response sample characteristics	169

Commonly used symbols and abbreviations

0D	zero-dimensional
1D	one-dimensional
2D	two-dimensional
3D	three-dimensional
nm	nanometer
μm	micron
THz	terahertz
GHz	gigahertz
IR	infrared
rf	radiofrequency
dc	direct current
ac	alternating current
$\vec{C}\hbar$	chiral vector
\vec{a}_i	lattice vector
n, m, q	integers
E, E_{gap}	energy, energy gap
k	electron momentum
v_F, v_F	Fermi velocity
C	nanotube circumference
K, K'	Dirac points
eV	electron volt

k_B	Boltzmann's constant
T	temperature
λ	wavelength
e	electron charge
h, \hbar	Planck's constant
$G(E)$	conductance
$M(E)$	number of modes
$T, T(E)$	transmission probability
G_Q	quantum of conductance
R_Q	quantum of resistance
Z_{fs}	impedance of free space
ε	dielectric constant
c	speed of light
R_c	contact resistance
C_c	contact capacitance
ℓ_m	mean free path
L, ℓ	nanotube length
R	electrical resistance
G	electrical conductance
R_{int}	total internal resistance
r_{int}	internal resistance per unit length
ω_o	optical-phonon frequency
C	capacitance

ZBA	zero-bias anomaly
dI/dV	differential conductance
dV/dI	differential resistance
I	electrical current
$V, V_{dc}, \Delta V$	voltage
V_{gate}	gate voltage
$\alpha, \alpha_{end}, \alpha_{bulk}$	power-law exponent
g	Luttinger liquid parameter
L_m	magnetic inductance
L_k	kinetic inductance
C_Q	quantum capacitance
C_{ES}	electrostatic capacitance
C_{tot}	total capacitance
v_p	propagation velocity
Z_o, Z_{char}	characteristic impedance
$f, \Delta f$	frequency, frequency spacing
Z_{in}	input impedance
Z_L	load impedance
ps	picosecond
ns	nanosecond
TEM	transmission electron microscope
SEM	scanning electron microscope
AFM	atomic force microscope

EFM	electrostatic force microscope
CVD	chemical vapor deposition
HSQ	hydrogen silsesquioxane e-beam resist
SE	secondary electron
TLD	through-lens dectector
ESD	electrostatic discharge
FTIR	Fourier transform infrared spectrometer
OPD	optical path difference
P	power
B	bandwidth
Z_{ant}	antenna impedance
η	coupling efficiency
G_{th}	thermal conductance
\mathcal{C}	heat capacity
I_{bias}, I_{dc}	dc current bias
S_V	responsivity
I_{THz}	terahertz current
R_L	load resistance
T_b	bath (substrate) temperature
T_e	electron temperature
P_{rf}	rf input power
NT	nanotube

Chapter 1

Introduction to Electron Transport in Single-Walled Carbon Nanotubes

1.1 Reduced Dimensionality

The past several decades have witnessed a technological drive for functional electronic devices that possess increased performance and affordability, often characterized by faster operation, lower energy consumption, cheaper fabrication, and reduced material usage. Electronic devices and integrated circuits have typically been miniaturized by shrinking the size of the features found in the latest processors. The scaling of the features in different dimensions can develop into two-dimensional (2D) sheets, one-dimensional (1D) lines, and ultimately zero-dimensional (0D) dot-like objects. However, if the wiring and features on chips begin to measure only a few tens of atoms across, the miniaturization process begins to confront fundamental challenges due to intrinsic material limitations. Unexpected behavioral shifts and functionality can emerge as the size shrinks from the macroscopic to atomic levels. The descriptions and governing laws of such systems cross over from the classical to quantum as quantum-mechanical effects begin to appear. Phenomena which do not occur in 3D begin to appear

in these reduced dimensions; for example, the fractional quantum hall effect in 2D conducting planes, quantized conductance and spin-charge separation in 1D conduction channels, and Coulomb blockade and single-electron charging effects in 0D quantum dots. New developments in materials science and chemistry encourage this progress into the nanoscale size domain and introduce new objects to investigate that exploit these quantum effects rather than view them as obstacles.

Our primary goal is to investigate the electronic properties of low-dimensional nanostructures, specifically probing the 1D nature of carbon nanotubes. To experimentally probe such fascinating phenomena, high-frequency measurement techniques are employed on nanofabricated devices at cryogenic temperatures.

1.2 The Many Forms of Carbon

Carbon, the sixth element of the periodic table, is an extremely versatile material which was known since ancient times. Carbon has experienced an interesting journey of discovery and usage over time. It can combine in a variety of manners yielding a family of stable crystalline structures possessing extremely varied mechanical and electrical properties. Amorphous configurations of carbon such as soot, ash, and charcoal have been known throughout history, even used by prehistoric artists. Allotropes of carbon, diamond and graphite, have been treasured since antiquity (Geim 2008). During the early eighteenth-century, it was found that the absorption of a certain substance into iron could produce steel. Towards the end of that century a trio of French scientists labeled that material as carbon and identified it as one of the fundamental elements (Wertime 1954).

In 1880, Thomas Edison utilized a carbon-fiber filament in his first incandescent light bulb, due to its ability to withstand high temperatures (Friedel 2010). The earliest published findings discussing hollow carbon cylinders were from Russian scientists Radushkevich and Lukyanovich in 1952 who used transmission electron microscopy (TEM) to image tubular structures measuring ~50 nanometers in diameter which were composed of carbon (Radushkevich 1952). However, since it occurred during the height of the Cold War, this breakthrough went largely unnoticed by Western scientists. As explained by Monthioux and Muznetsov, many other groups observed carbon nanotubes using TEM in the 1950s continuing through the 1970s, but at the time these structures were often understood as unwelcomed contaminants. Their formation was the result of processes focused on achieving other goals and these structures were subsequently not appreciated as an exciting new area of interest for potential further study (Monthioux 2006). However, this began to change in the late 1980s, when Buckminsterfullerene, also known as a buckyball, was discovered (Kroto 1985). This zero-dimensional spherical fullerene molecule resembles the shape of a soccer ball and is composed entirely of carbon at each vertex, with the chemical formula C_{60} . In addition to new systems sought for study, this time simultaneously witnessed the development of new characterization instruments with the concurrent need of the semiconductor industry to reduce the size of integrated circuits.

A major breakthrough in carbon research came in 1991 when Sumio Iijima synthesized multi-walled carbon nanotubes and carefully identified them as concentric, seamless carbon cylinders (Iijima 1991). Iijima's discovery, combined with concurrent theoretical studies of the properties of carbon nanotubes (Hamada 1992, Saito 1992),

launched unprecedented interest into nanotubes and fueled intense research. Soon after, in 1993, two research groups located the first single-walled carbon nanotubes (Iijima 1993, Bethune 1993), a single carbon sheet rolled into a tubule. The late 1990s and early 2000s experienced an explosion of research into the unique mechanical, optical, thermal and electrical properties of these nanotubes that was motivated by a wide variety of proposed potential applications (Ajayan 2001). A significant shift in carbon research came in 2004 with the development of the mechanical exfoliation method for cleaving three-dimensional graphite, composed of stacked, loosely bound graphene sheets, into a single layer of graphene (Geim 2008). Figure 1.1 shows the family of stable crystalline structures possible from hexagonal carbon-carbon bonding. Two-dimensional graphene and one-dimensional carbon nanotubes have emerged as novel environments for the study of exotic fundamental physics and as attractive candidates for the development of innovative applications by exploiting their unique fascinating properties.

1.2.1 Carbon Nanotubes

Carbon nanotubes are hollow cylinders of hexagonally bonded carbon atoms with a diameter measuring about one to a few nanometers and possessing lengths up to several centimeters. The small circumference and long lengths give rise to extreme aspect ratios (Wang 2009). They possess incredible mechanical, electrical, thermal, and optical properties, making them attractive topics of study unto themselves and appealing candidates for potential application by a wide range of scientists and engineers.

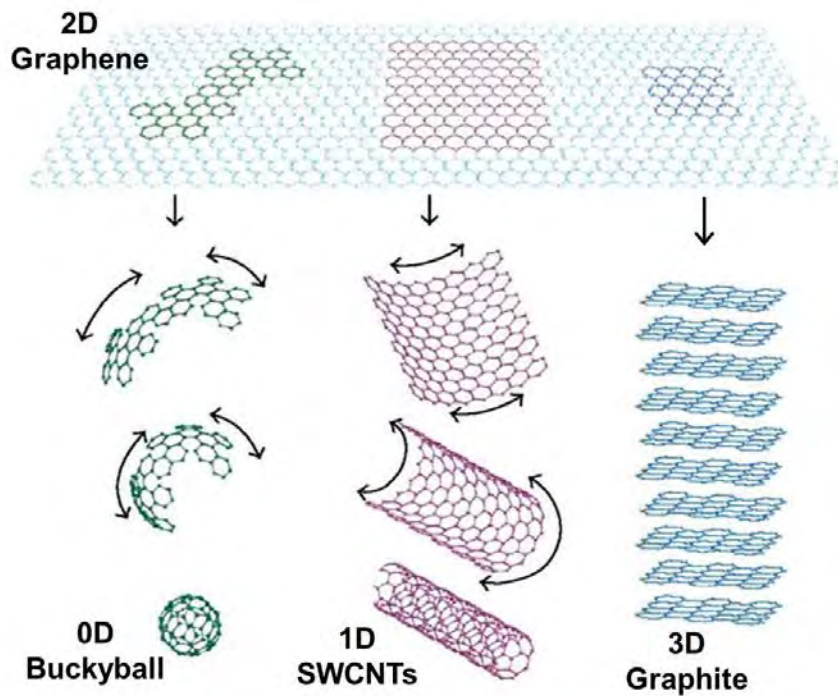


Figure 1.1 – Carbon is an amazing element which can produce extremely versatile materials. Combining in a variety of different manners yields a family of stable crystalline structures possessing extremely varied mechanical and electrical properties which allow for the study of different dimensional behavior. From the two-dimensional (2D) graphene sheet, one can conceptualize forming a zero-dimensional (0D) buckyball, a one-dimensional (1D) single-walled carbon nanotube, or three-dimensional (3D) graphite (adapted from Geim 2007).

Mechanically, the strong covalent carbon-carbon bonding, and low-density hollow structure, makes carbon nanotubes very stiff but also lightweight, earning them the title of “strongest synthesized material” known to date. Carbon nanotubes possess a large axial tensile strength and exceptionally high Young's moduli, in the terapascal range (Treacy 1996). Applications utilizing strong nanotube-based composites are already found in commercially available tennis rackets, bicycle frames, and structural aerospace elements to improve strength while not significantly contributing to weight.

Carbon nanotubes have been explored as a future basis for high-frequency, low-power, low-cost and flexible electronic devices as well as chemical and gas sensors (Endo 2008). Their chemically inert nature allows their structure to be physically unaffected by exposure to many substances. Their high sensitivity as chemical sensors is due to the fact that each carbon atom is on the outside of the nanotube, resulting in a very high surface area; the presence of even an additional individual molecule can lead to a significant and measureable impact on the nanotube's properties.

With the constant shrinkage of silicon transistor features in the semiconductor industry and the inherent associated difficulties, the advantages of self-assembled carbon nanotubes possessing superior electrical and thermal conductance are recognized. Top silicon chip manufacturers such as IBM and Intel have shown interest in replacing parts of modern computer chip circuitry, such as the interconnects or the transistors themselves, with nanotubes possessing widths on the order of one nanometer (Endo 2008). As the electronic properties of carbon nanotubes are most relevant to this dissertation, in particular, those of single-walled carbon nanotubes, these attributes are deserving of closer attention and examination.

1.2.2 Electronic Band Structure of Carbon Nanotubes

To understand the electrical properties of carbon nanotubes, one must begin from the physical and electrical properties that it inherits from its parent materials, graphite and graphene. As shown in Figure 1.1, graphite is composed of a three-dimensional stacking of single atomic layers of carbon atoms bonded to one another and arranged in a repeating network that form a hexagonal-honeycomb lattice structure in a plane one atom thick known as graphene. These two-dimensional graphene sheets are only weakly bound to one other, and it is possible to isolate a single layer of graphene using the mechanical exfoliation process (Geim 2008). Graphene is a hexagonal sheet of carbon atoms with a basis of two atoms. Each carbon atom possesses 6 electrons in a $1s^2 2s^2 2p^2$ configuration, where the two core electrons are strongly bonded to the nucleus, but the four valence electrons are only weakly bound. The energy difference between the atomic orbitals is small, allowing for these outer orbitals to mix with one another to form more energetically favorable bonds with neighboring atoms through special sp^2 hybridized orbitals (Saito 1998). The three sp^2 hybridized orbitals then form planar covalent sigma-bonds with nearest neighbor carbon atoms situated 120 degrees apart, resulting in a very strong two dimensional graphene hexagonal physical structure. This is the origin of the cohesive mechanical structural properties of this system, resulting in the high Young's modulus and mechanical applications mentioned earlier. A delocalized weak π -bond exists orthogonal to the plane, which explains the ease of separating graphite into individual graphene sheets. Simple variations in hybridization can lead to vastly different material properties. For example, diamond displays sp^3 hybridization where each carbon

atom has four covalent bonds with neighboring atoms. Diamond is the hardest material known, is highly transparent, and possesses a low electrical conductivity, whereas graphite, by comparison, is dark in color, soft in form, and is a very good electrical conductor. In 1947, P.R. Wallace used the tight-binding method to determine that the electronic characteristics of a network of hexagonal carbon atoms form a 2D energy dispersion relation composed of two bands that join as cones at the edges of the Brillouin zone, thereby producing a zero-gap semiconductor (Wallace 1947), as displayed in Figure 1.3b.

A carbon nanotube can be conceptualized as “wrapping up” a sheet of graphene into a seamless hollow cylinder, although the techniques to physically synthesize carbon nanotubes utilize a completely different process, as explained in Chapter 3. Rolling the sheet more or less “tightly” produces a nanotube with smaller or larger diameter. The crystal structure of a given nanotube is specified by the direction/angle that the sheet is “wrapped,” known as the chiral vector, given by $\vec{Ch} = n\vec{a}_1 + m\vec{a}_2$ where n and m are integers such that $0 \leq |m| \leq n$, and \vec{a}_1 and \vec{a}_2 are lattice vectors of the carbon sheet, which connects the origin (0,0) to the vector head at the carbon atom specified by coordinates (n,m) (Saito 1998, Biercuk 2008, Ilani 2010) as shown in Figure 1.2. The (n,m) lattice indices uniquely describe the carbon nanotube structure and due to symmetry m need only satisfy $0 < m < n$. The resulting nanotube diameter is given by the length of the chiral vector divided by π and can be as small as 0.7 nm.

The chiral angle, defining the nanotube’s helicity, can imply dramatically different electrical properties. The optical and electronic properties of a crystal come from understanding its energy dispersion relation, relating the energy and momentum of

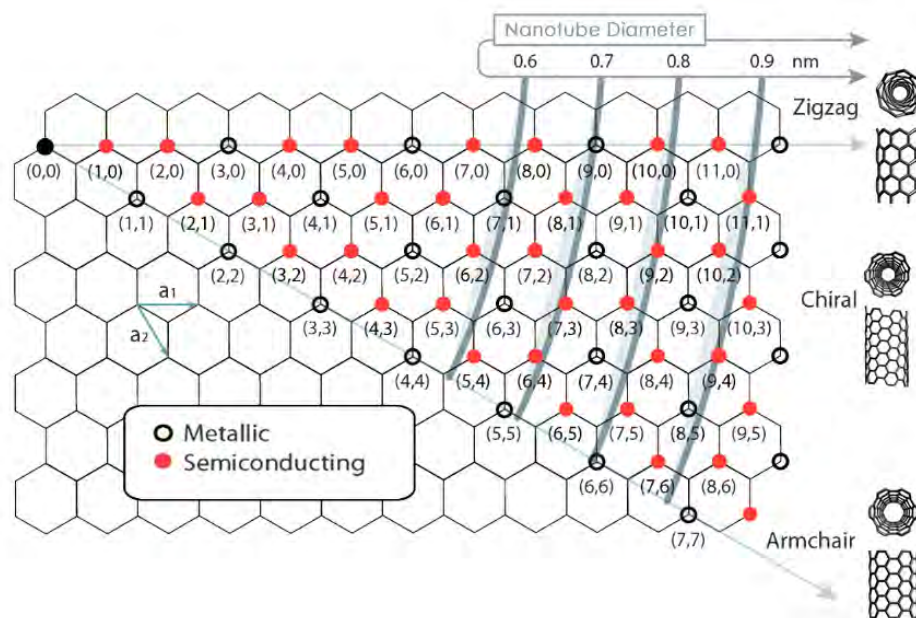


Figure 1.2 – Chart illustrating the carbon nanotube chirality, diameter, and electronic structure resulting from rolling up a graphene hexagonal sheet along a chiral vector from origin to (n,m) index (adapted from Landi 2009).

an electron in the system. The nanotube energy dispersion relation comes directly from considerations of the parent material, namely graphene. At the Fermi energy, located at the corners of the graphene Brillouin zone, the conduction and valence bands “touch” at what are referred to as Dirac points and the density of states vanishes. Hence, electrically, graphene is indeed a zero-gap semiconductor. For small momentum k around the Dirac points, the energy dispersion relation is linear with $E = \hbar v_F k$, where E and k are the energy and momentum measured from the center of the cone, and $v_F \approx 8 \times 10^5$ m/s is the Fermi velocity (Wallace 1947). Of the six Dirac points, only two, referred to as K and K’ points, are irreducible due to the two atom basis of the graphene structure and they are sufficient to consider for determining the electronic properties of graphene and nanotubes. Rolling the graphene into a tube imposes periodic boundary conditions on the electron wavefunction within the nanotube, resulting in quantization in the circumferential direction k_{\perp} , where $k_{\perp} = 2\pi n/C$, with C being the circumference of the nanotube, and n is an integer. This quantization cuts discrete slices out of the 2D Dirac dispersion of graphene highlighted in light blue in Figure 1.3c and 1.3d leading to a series of 1D subbands superimposed. If one of these subband slices intersects the Dirac point, the resulting nanotube will exhibit a linear dispersion relation and is said to be metallic; if not, the nanotube is semiconducting and possesses a section of its density of states at the Fermi energy that is zero, which displays an energy gap E_{gap} inversely proportional to the cylindrical diameter, that is, $E_{gap} \approx 0.7eV/d[nm]$ (Biercuk 2008, Ilani 2010). In general, a nanotube will be metallic if the (n,m) indices obey the relation $n-m = 3q$, where q is an integer, and is semiconducting otherwise. Thus, assuming no electron or hole doping, only one-third of a randomly distributed collection of nanotubes are expected to

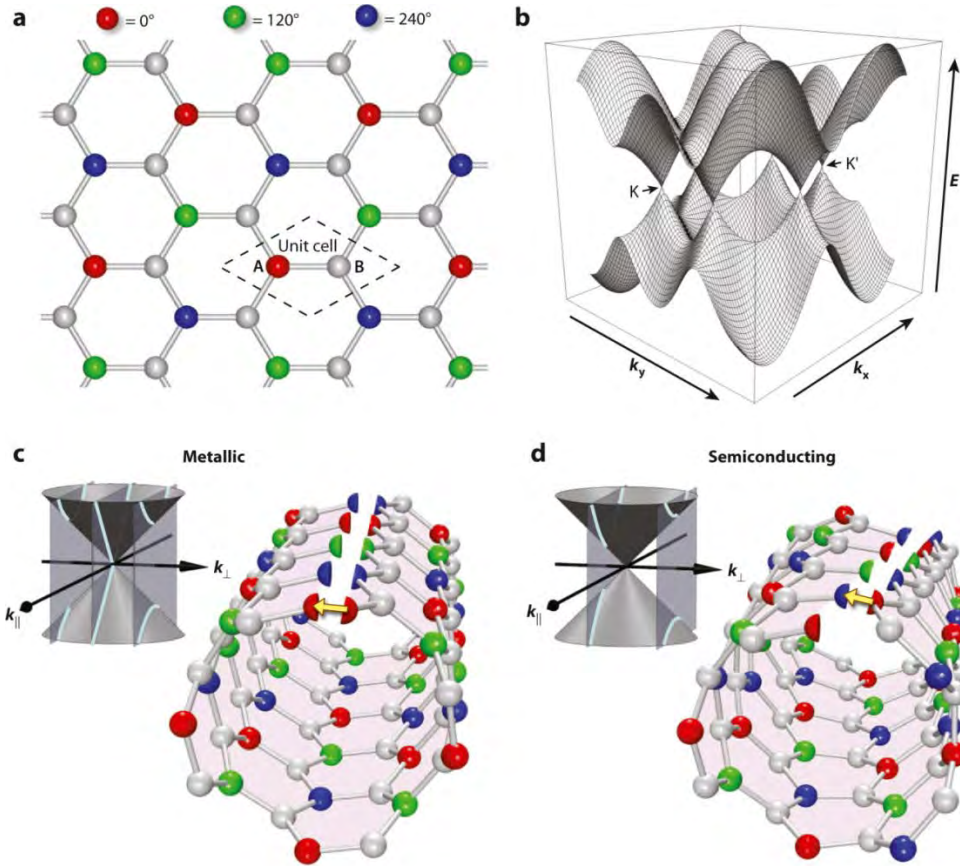


Figure 1.3 – (a) Graphene sheet hexagonal structure highlighting two carbon atom unit cell. (b) Energy band diagram of graphene with six Dirac points at position inverted valence and conduction band cones meet. There are two irreducible K and K' points in the Brillouin zone due to the two atom unit cell. (c) One possible metallic nanotube structure where carbon atom of hexagonal lattice is rolled to seamlessly occupy the position of another carbon atom with similar position. (d) A possible structure for a semiconducting nanotube where the atoms do not seamlessly match up. The quantization condition imposed by periodic boundary conditions overlaying the inverted cone Dirac point results in different dispersion relations for the metallic and semiconducting cases: in the metallic inset the quantization slices (light blue) intersect the Dirac point, producing a nonzero density of states throughout and a linear dispersion relation, while for semiconducting, the quantization slices do not intersect the Dirac point and a band gap results (adapted from Ilani 2010).

be metallic, whereas two-thirds will be semiconducting. However, this simple theory does not take into account perturbations due to mechanical deformations such as twists, strains, stretches and the overall tube curvature of the rolled graphene sheet. Due to such distortions, the carbon-carbon bonds parallel and perpendicular to the axis are slightly unequal, which will open a small bandgap in the continuous dispersion relation. Such deformations are unavoidable and always exist in real nanotube systems. Thus, truly metallic nanotubes are extremely rare, so that, in practice, small-bandgap nanotubes possessing gaps in the band structure around 10 to 100 meV are combined in the “metallic” labeled set (Biercuk 2008). This dissertation focuses on the properties of these more common “metallic” single-walled carbon nanotubes and they will be the assumed type of nanotube discussed in the subsequent text unless otherwise noted.

1.2.3 Electron Transport in Carbon Nanotubes

Electrical measurements of basic properties of carbon nanotubes are carried out by either running a direct or alternating current (dc or ac) through metal *source* and *drain* electrodes contacting both ends of the nanotube. Three-terminal conductance measurements can be used to determine the electrical properties of a metallic or semiconducting carbon nanotube. A field-effect transistor geometry is a configuration where the carbon nanotube is contacted by the two source and drain metal electrodes in the presence of a third nearby electrode not contacting the nanotube, commonly called the gate electrode. When utilizing a carbon nanotube in this geometry, the gate and nanotube act as two plates of a capacitor and the gate can capacitively influence the electrostatic

potential of the nanotube and electrostatically changes its charge density. A negative bias on the gate induces positive charges onto the nanotube, and a positive bias induces negative charges. Thus, electrostatic coupling of a gate voltage has the effect of shifting the energy of all the electrons so that one can tune the Fermi level into and out of the bandgap or through the Dirac point by applying a voltage to the gate as shown in Figure 1.4. Ohmic electrical contact to the nanotube with degenerately-doped silicon wafers as the gate electrode separated from the nanotube by a high-k dielectric, a gate configuration referred to as a back-gate, affords a nanodevice that has been shown to perform on par with silicon transistors currently used in microelectronics (Saito 1998). At room temperature and below, semiconducting nanotubes exhibit a broad region of zero conductance since the bandgap energy is much larger than thermal energy, i.e., $E_{gap} \gg k_B T$, where the gate can turn the conductance on and off. In contrast, small-bandgap “metallic” nanotubes exhibit a modest dip in conductance near zero gate voltage but do not reach a full off state at room temperature, since the energy of the bandgap is comparable to the thermal energy, i.e., $E_{gap} \sim k_B T$. In Figure 1.4, several transport traces of different nanotube devices are plotted with the source-drain conductance as a function of voltage applied to the back gate.

More details regarding the extraordinary nature of carbon nanotube electronic properties can be found in the literature. For example, metallic carbon nanotubes in theory can carry a current density up to $\sim 10^9$ A/cm² (Yao 2000, Javey 2003), which is three orders of magnitude greater than copper, the metal commonly used as an interconnect in modern electronic devices. Semiconducting nanotubes can possess considerable on/off ratios of $\sim 10^6$ (Javey 2003) which makes them attractive as

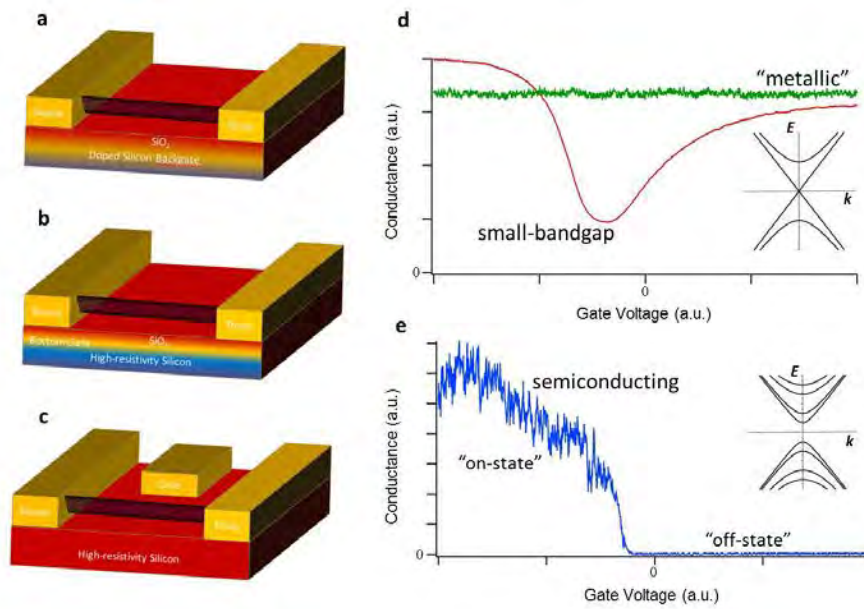


Figure 1.4 – Gate configuration for (a) back-gated (b) bottom-gated (c) side-gated nanotube device. (d) Typical conductance versus gate voltage plot for a “metallic” nanotube with $E_{gap} < k_B T$ and small band-gap nanotube with a dip in conductance $E_{gap} > k_B T$ and (e) typical conductance versus gate for semiconducting nanotube with complete turn-off in gap region. Insets shows zone-folded linear dispersion relation for ideal metallic nanotube (top) and semiconducting dispersion relation with energy gap (bottom).

replacements for transistors in circuits. Short length nanotubes can exhibit ballistic conduction. See Biercuk *et al.* (2008) and Ilani *et al.*(2010) for reviews of the surprising phenomena so far observed in these incredible systems. Beyond the impressive promise for potential technological applications and future nanoelectronics, individual carbon nanotubes also provide an intriguing and exciting laboratory for studying 1D electron transport physics and quantum mechanical phenomena which have no higher-dimensional counterparts.

1.3 One-Dimensional Nature

Landau's Fermi liquid theory is an approximation that describes the behavior of low energy conduction electron excitations in metals as an independent electron model by substituting non-interacting quasiparticles for the interacting electrons. In physical terms, a quasiparticle can be thought of as a bare electron which is dressed in a screening cloud formed by the collection of all the other electrons from the Fermi sea. The result is a renormalized electron mass and an effective screening of the Coulomb interaction between the electrons in the many-body system (Landau 1957). The Fermi liquid model is extremely successful in explaining the properties of 3D conductors.

However, the assumptions underlying this approximation no longer hold in 1D and the Fermi liquid model breaks down to reveal new and interesting phenomena. For instance, electrons in 2D and a low magnetic field are well described by this Fermi liquid model. At a higher magnetic field, the fractional quantum Hall effect can be observed, which requires the inclusion of electron-electron interactions. These excitations are

unlike bare electrons since they possess fractional charge. Unlike 3D systems, the effects of electron-electron interactions can transform a 2D electron system into a collective state of new quasiparticles under such extreme conditions. Such exciting collective behavior has been experimentally observed in graphene and other 2D electron gases (Bockrath 1999b, Zhang 2006).

Similarly, many intriguing phenomena of 1D electron systems, such as conductance quantization explained in the next section, can be explained in terms of non-interacting quasiparticles. However, other dramatic effects are predicted due to weak screening in 1D by the electron cloud. The inclusion of the Coulomb interactions significantly modifies the picture of free electrons employed by the Fermi liquid model thereby necessitating an alternative paradigm. An interacting 1D electron gas instead forms a strongly correlated state known as a Luttinger liquid, where, in contrast to a Fermi liquid, the low-energy excitations are bosonic sound-like density waves, known as plasmons (Tomonaga 1950, Luttinger 1963).

Probing such correlated effects of electron-electron interactions in physical systems has motivated the search for an experimental realization of a long, disorder-free 1D wire. When the size of the physical structure of a conductor becomes comparable to the Fermi wavelength of an electron, the wave properties of the electron must be accounted for as described earlier. Narrow quantum wires have been fabricated using conventional techniques employing cleaved-edge molecular beam epitaxy (Auslaender 2002). For a carbon nanotube, the diameter ~ 1 nanometer is on the order of the Fermi wavelength $\lambda_F = 2\pi/k_F \sim 0.75$ nm (Dekker 1999). As previously discussed, the small diameter of a carbon nanotube confines the electron wavefunction and leads to

quantization in the circumferential direction. Single-walled carbon nanotubes are thus a truly 1D natural structure and offer a unique tangible laboratory to study electrons in 1D. The predictions of correlated electron behavior in carbon nanotubes treated as a 1D Luttinger liquid will be examined in Chapter 2 and are the main focus of this dissertation.

1.3.1 Quantum of Resistance

As nanomaterials approach small size scales, more complex descriptions of electron transport crossover between classical and quantum regimes are required. Classically, according to Ohm's law, as the cross-sectional area of a conduction channel approaches zero, the device resistance will increase to infinity. Similarly, as the length approaches zero, the device resistance tends towards zero. However, experimentally, for an ideal conductor possessing a small number of conducting channels, the conductance tends towards a specific finite value known as the *quantum of conductance*, which is defined in terms of fundamental constants of the electron charge e and Planck's constant h . Such quantum behavior occurs due to the fundamental impedance mismatch between the large number of modes in the macroscopic contacts over which the current is distributed and the limited number of electronic modes accessible in these individual channels. The Landauer formula incorporates this in its equation for conductance of a quasi-1D system,

$$G(E) = \frac{2e^2}{h} M(E)T(E)$$

where $M(E)$ is the number of modes and $T(E)$ is the transmission probability of an electron at the Fermi energy, E (Datta 1995, Saito 1998). Fundamental *contact* resistance

comes from considering the current arising from the transmission and the Fermi-Dirac distribution of an electron injected from a macroscopic electron reservoir in thermodynamic equilibrium at a given electrochemical potential into a single ballistic quantum channel connected to another macroscopic reservoir transparent contact at a lower electrochemical potential (McEuen 1991).

For metallic carbon nanotubes, there are two 1D subbands available for electron transport, see Figure 1.3a and b. These arise from the two irreducible distinct K-points and the initial factor of two in the Landauer formula that accounts for the spin degeneracy of spin up and spin down electrons in each subband. This yields four parallel channels, or a fourfold-degenerate 1D subband, contributing to the conductance. A transmission probability of unity, $T(E)=1$, results in ballistic conduction where the voltage drops only occur at the contacts as an electron enters from the 3D macroscopic metal contact to the 1D conductor and emerges back out to the other 3D macroscopic metal contact. The resulting quantum conductance value of $G_Q = \frac{4e^2}{h}$ can be converted into a *quantum of resistance* for carbon nanotubes $R_Q = \frac{h}{4e^2} = 6.5 \text{ k}\Omega$ (McEuen 1991, Biercuk 2008, Ilani 2010). To achieve this fundamental lower limit for the impedance of a single nanotube device, one must create a device that is perfectly clean of defects, possessing Ohmic contacts, and be measured at low temperature. In comparison, typical microwave equipment is manufactured to have an impedance of 50Ω and the impedance of free space is $Z_{fs} = 1/\epsilon_0 c \approx 377 \Omega$, where ϵ_0 is the permittivity of free space and c is the speed of light. Thus, such a large intrinsic impedance results in very poor power transmission from any macroscopic system into a 1D system. This presents significant challenges for

electrical explorations of carbon nanotube devices and the measurement scheme that will be presented in Chapter 4. Additionally, further contact barriers in excess of this resistance quantum can form at the metal-tube interface and increase the contact resistance beyond this ideal value, as will be discussed next.

1.4 Metal-Nanotube Interface

A main source of excess electrical resistance beyond the fundamental quantum resistance of $6.5\text{ k}\Omega$ occurs at the interface between the metal electrodes and the nanotube. There are several different potential sources for this contact resistance, R_c , in nanotube devices. Any type of impurity located at the contact interface, including processing residue or water molecules from air exposure, can impede electrical conduction. Careful cleaning and handling of the silicon substrate chip and nanotube devices throughout the many processing steps (as will be described in Chapter 3) can reduce this sort of contact resistance, but cannot be fully prevented or eliminated. These contaminants degrade the nanotube device performance by increasing their electrical resistance and can prevent some phenomena from appearing.

Another type of contact resistance, known as a Schottky barrier, is more fundamental. This arises from the alignment of electronic states at the metal-nanotube interface (Biercuk 2008). Energy band misalignment between the metal electrode and the nanotube will result in a potential barrier. The height of this energy barrier depends on the metal electrode work function, the nanotube work function, and the nanotube energy gap. Due to their much larger band gap, semiconducting nanotubes exhibit a much higher

Schottky barrier than metal nanotubes. If the Fermi level of the metal contact lies in the middle of the nanotube band gap, then a Schottky barrier exists for both p- and n-types of conduction. When the Fermi energy of the metal electrode aligns with the nanotube valence band, a p-type contact forms, allowing holes to freely flow with no barrier; however, electrons will experience a large barrier. The type of conduction for nanotube device can be determined during fabrication depending on the metal chosen for the electrodes. High work function metals can lead to p-type conduction with the primary carriers as holes, whereas a low work function metal will lead to n-type contacts with the primary carriers as electrons.

In addition to the metal work function, the surface chemistry of the metal selected can determine how successfully it wets and adheres to the nanotube. Due to the small contact area of the nanotube, it is extremely difficult for the metal atoms to fully cover the tubular structure of its surface, where, instead of a uniformly coated contact region, the deposited metal atoms can form nanoclusters covering the nanotube surface discretely, producing poor electrical coupling, or at an atomic level, a physical vacuum gap barrier can exist between the metal and nanotube resulting in a large series contact resistance. Many different electrode metals have been examined to obtain stable and robust low-resistance Ohmic contact to nanotubes. Palladium and platinum have similar large work functions but produce very different device characteristics in that palladium electrodes yield low-resistance Ohmic electrical contacts due to good wetting interaction (Mann 2003), while platinum yields high contact resistance devices attributed to its poor wetting properties (Chen 2005, Lim 2009). Other groups use graphitic interfacial layers

to act as a mediator between the metal and nanotube to improve the metal-nanotube interface overlap (Chai 2012).

Additionally, the contact properties are highly sensitive to the environment and adsorbed dipoles can strongly shift the metal work functions. Different annealing processes, such as high-temperature thermal annealing of the entire device or electric-current-induced local Joule heating, have been found to reduce the contact resistance due to heat-induced desorption of adsorbates on the nanotube surface or the relaxation of structural imperfections and the tunneling barrier at the interface (Malapanis 2011). Large contact resistances can produce interesting devices such as quantum dots or exhibit interesting behavior such as Coulomb blockade (Ilani 2010). For this thesis, the role of these interface effects will be significant as a possible explanation for the appearance of a zero-bias anomaly at low bias and low temperature, as will be discussed in Chapter 5.

1.5 Electron Mean-Free Path in Nanotubes

In addition to the effects of contacts on the nanotube resistance, scattering processes within the nanotube channel itself will also contribute to the measured resistance of a nanotube device. The Kim Group at Columbia University has examined the conductance of very long individual nanotubes with multiple contacts, allowing for measurements of several different length segments of the same nanotube, enabling a determination of the resistance per unit length (Purewal 2007). This also allows for the determination of the mean free path, ℓ_m , the average distance traveled by an electron in the nanotube before it is scattered. For a nanotube channel length L less than ℓ_m , the transport is considered

ballistic with an absence of scattering. For a channel larger than ℓ_m , the transport is diffusive and an electron will undergo many collisions in the conduction channel, and the conductivity depends on average only on the concentration of scattering events. A selection of the limited published data on high-quality individual carbon nanotube room-temperature resistance is plotted on a single curve in Figure 1.5 showing the trend toward ballistic transport and long ℓ_m with a decrease in length. For non-unity transmission, within a diffusion regime of electron transport, the voltage drop will not only occur at contacts, but also over the length of the nanotube. The device two-terminal resistance is then given by:

$$R = \frac{1}{G} = \frac{h}{4e^2} \frac{1}{T} = \frac{h}{4e^2} + \frac{h}{4e^2} \frac{L}{\ell_m} + R_c$$

where G is the conductance, T is the transmission probability, L is the length, and R_c is the contact resistance. The first term is simply the quantum resistance, as described earlier. The second term gives the scattering associated with an electron as it travels through nanotube. These scattering events are typically triggered by other electrons, thermal lattice vibrations known as phonons, defects in the crystalline structure of the nanotube (including vacancies, substitutions, twists, strains or bends in the nanotube), electrostatic potential fluctuations resulting from trapped charges in the substrate oxide surface, adsorbates on the nanotube surface, or other impurities in the surrounding environment. The final term is the contact resistance as discussed in the previous section. Typical techniques for excluding contact resistance effects, such as four-terminal measurements, are not feasible for one-dimensional conductors since any electrode contacting the conductor will destroy its one-dimensional electrical nature; thus, only

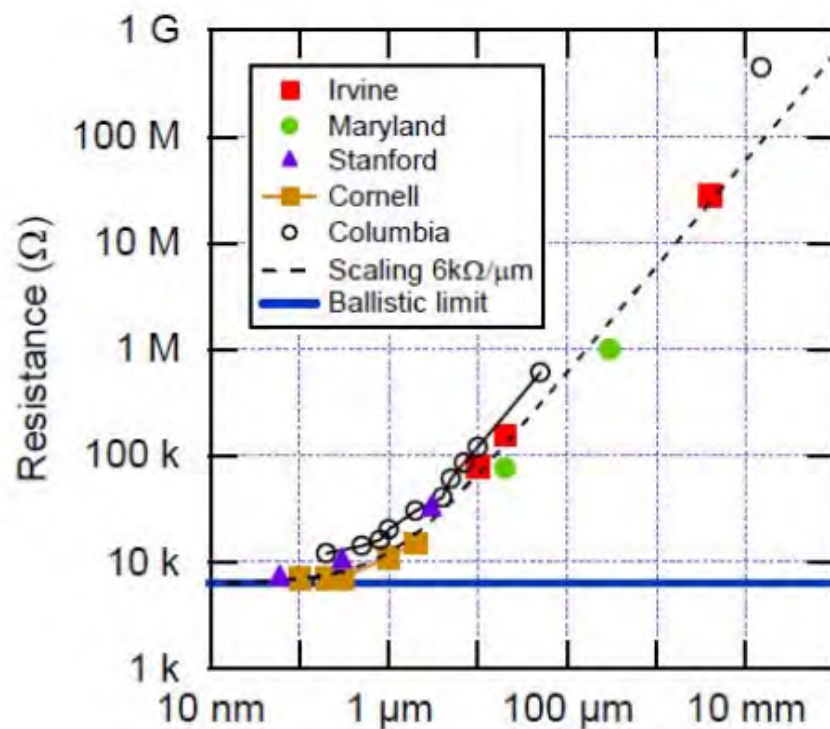


Figure 1.5 – Length dependence of room-temperature resistance for individual single-walled carbon nanotubes in the literature. The published data follow a single curve corresponding to a resistance per length of $6 \text{ k}\Omega/\mu\text{m}$ for longer nanotubes and approaching the ballistic quantum resistance limit (Burke 2007).

two-terminal measurements including the unavoidable contact resistance can be performed.

At finite temperature or high-biases, electron-phonon scattering is significant. At room temperature, inelastic scattering with acoustic-phonons dominates, and the mean free path can be limited to a few hundred nanometers in semiconducting nanotubes and nearly a micron in metallic nanotubes. Theoretical work predicts long mean free paths for metallic nanotubes where the scattering of electrons is strongly suppressed (Ando 1998, McEuen 1999). With decreasing temperature, acoustic-phonon scattering is reduced and the mean free path increases, until reaching a constant value due to elastic scattering from impurities. At low temperature, ballistic transport has been experimentally confirmed in metallic nanotubes, and an electron mean free path as high as 10 micron has been reported (Mann 2003), and for semiconducting nanotubes a mean free path on order of 1 micron has been observed (Purewal 2007). These values are exceptionally long when compared to conventional 2D electron gases or other materials such as copper or silicon. For the best metallic nanotubes measured at low temperature, there is an internal resistance per unit length, r_{int} , of about $1 \text{ k}\Omega/\mu\text{m}$ (Purewal 2007).

Nanotubes on substrates show strong elastic scattering; measurements on suspended nanotubes often show near-ideal transport characteristics, indicating that much disorder comes from interactions with the substrate. At large *source-drain* biases, electrons can accelerate to energies well above the Fermi energy and these hot electrons can scatter very efficiently by emitting optical and zone-boundary phonons. This scattering keeps any electron energy from exceeding the optical-phonon energy $\hbar\omega_o \sim 160 \text{ meV}$ above the Fermi energy. This sets a limit on the maximum current of

$I_{max} \sim \frac{4e^2}{h} \frac{\hbar\omega_0}{e} \sim 25 \mu A$ in most nanotubes since any electron possessing excess energy beyond that will rapidly emit a phonon (Yao 2000). The observation of this current saturation value is one method for determining that a nanotube device consists of an individual single-walled carbon nanotube. Polar optical phonons of the substrate have much lower energy, ~ 60 meV for SiO₂ phonons, and can also be a means of energy loss for the electron system. The excess energy created by the phonon emission can be substantial, significantly heating the nanotube. The heating of a nanotube by its internal resistance is central to the high-frequency bolometric detection mechanisms described in Chapter 5.

1.6 Summary

Carbon nanotubes exist at a pivotal intersection within the rich history of materials research engineering of carbon and the microelectronics industry. They present a plentiful treasure trove for scientific inquiry due to their unique properties offering extremely attractive potential for a wide variety of applications as well as providing an exciting test environment for interesting fundamental phenomena. Their electrical properties are remarkably distinct and these small molecules are truly one-dimensional electrical systems. It is this 1D nature that we aim to explore and probe in an attempt to verify a well-regarded fundamental model of electron transport in this reduced dimension. However, there are many challenges to such studies, including the quantum of resistance for traversing from 3D macroscopic leads to the 1D nanotube, the issues with establishing high-quality electrical contacts, as well as the many sources of internal scattering within

the nanotube. In the next chapter we discuss the motivation and background for probing the 1D nature of the nanotube system, and explain how we can actually take some of these seemingly insurmountable difficulties and exploit them for our advantage.

1.7 Overview of this dissertation

This dissertation consists of six chapters:

In the first introductory chapter, we provided a brief historical context for the investigation of carbon nanotubes and present the elementary basis for to their composition, structure, and properties, with a particular focus on electronic characteristics as they are most relevant to this work. An understanding of carbon nanotube transport properties and their potential applicability in high-frequency devices provides the rational for our research.

In Chapter 2, we explore novel phenomena that arise in one-dimensional conductors and motivate the principal aim of this work: measuring terahertz (THz) electrical transport in a carbon nanotube as means of probing its one-dimensional behavior.

Chapter 3 describes breakthroughs in carbon nanotube synthesis mechanisms, device fabrication specifics, and highlights some of the challenges with regard to sample yield.

The experimental techniques and measurement setup used in this work are discussed in Chapter 4. We also explain how the application of classical approaches, such

as Fourier Transform Spectroscopy with a carbon nanotube as the detector element, can reveal new phenomena.

In Chapter 5, we discuss THz detection mechanisms and report on those observed in carbon nanotubes. We distinguish between the observed mechanisms at radiofrequency and at THz frequencies. A nonlinear response at THz frequency to determine an upper bound on the contact capacitance to a carbon nanotube is employed.

Chapter 6 presents the observed THz spectral response of carbon nanotube devices and derives the propagation velocity of collective mode electronic excitations of a carbon nanotube. We obtain empirical values for the Luttinger parameter describing this one-dimensional system.

Chapter 2

High-Frequency Luttinger Liquid Excitations in Carbon Nanotubes

2.1 High-Frequency Applications

Carbon nanotubes are an astonishing material possessing many remarkable properties making them attractive for numerous high-frequency electronic applications, as discussed in the previous chapter. The drive for faster integrated circuits manufactured at lower cost, consuming less material and possessing greater functionality motivates explorations of the performance and reliability of such novel nanomaterials at high-frequency. Carbon nanotubes may offer a potential solution for many of the issues plaguing the current materials employed in integrated circuits. Nanotubes can form the foundation for high-speed nanometer technologies with large power savings combined with increased performance. Possessing widths on the order of one nanometer, semiconducting nanotubes can function as exceptionally fast transistors. Metallic nanotubes could be advantageous as extremely tiny interconnects, the wires that connect the transistors within a circuit (Burke 2004). They exhibit high current-carrying capacities and with nanometer-scale diameters can sustain such high currents without failing due to

electromigration. The speed of transistor operation can be faster as dimensions are scaled down. An important criterion for high-frequency performance is the RC time constant, the product of the circuit resistance R and circuit capacitance C . Despite the large fundamental impedance of nanotubes due to the resistance quantum, the small capacitances predicted for nanotube transistors would allow them to possess intrinsic RC frequencies above six terahertz (Burke 2004). The frequency dependent response of conventional metallic materials has been well studied; however, the high-frequency behavior of nanotube devices is not yet well understood. Theoretical models have been developed and some experiments have been performed to investigate the carbon nanotube's ac conductivity. However, before delving into the high-frequency properties of carbon nanotubes, we first discuss predictions of their high-frequency behavior which reflect this system's one-dimensional nature.

2.2 Luttinger Liquid Theory

Landau's Fermi liquid theory is successful in explaining the properties of 2D and 3D bulk conductors by treating low-energy elementary excitations of the interacting electron system as free quasiparticles that behave as non-interacting Fermions obeying Fermi statistics and possessing charge e and spin $\frac{1}{2}$. Electron-electron interactions are limited to the Pauli exclusion principle. Repulsive Coulomb interactions are ignored due to their improbability given realistic electron densities in 3D materials. Physically, a quasiparticle can be regarded as a bare electron surrounded by a screening cloud of the other electrons from the Fermi sea. Although Fermi liquid theory describes conduction in bulk 3D

metals, the theoretical situation is altered as dimensions are reduced into systems where electrons are confined to channels that are the size of the electron wavelength. Such channels are effectively 1D for the electrons, and the repulsive Coulomb interactions are unavoidable because of the weak screening by the few other electrons. The Coulomb interactions dominate transport causing the electrons to behave in a highly cooperative way. Fermi liquid theory no longer applies and correlated electron phenomena become significant and must be accounted for. A theoretical treatment of conduction in 1D was first done by Tomonaga (Tomonaga 1950) and by Luttinger (Luttinger 1963) and later refined by others (Tarkiainen 2001). The interacting 1D electron gas forms a strongly correlated state known as a Luttinger liquid, where, in contrast to a Fermi liquid, the low-energy spin and charge excitations are described as bosonic sound-like density waves of charge and spin, respectively known as plasmons and spinons. These are conceptually similar to phonons, which are also boson-like. The addition of a charge carrier to the system is considered an excitation of the entire bosonized Luttinger liquid state. Predicted hallmarks of this Luttinger liquid are a power-law dependence of thermal and electrical conductivity as well as spin-charge separation, where the charge and spin bosonic modes are separable and propagate at different velocities (Deshpande 2010). Due to their small size and low electron density, carbon nanotubes should be nearly ideal realization of such interacting 1D system and offer an excellent laboratory for testing such predictions of the transport behavior of Luttinger liquids.

2.2.1 Power-Law Suppression of Tunneling

The power-law dependence expected for electron transport is a result of the fact that electron movement is constrained to only two directions along the length of the channel in a 1D wire. An electron tunneling into or out of a 1D wire will create a density perturbation forcing the other electrons to shift away in order to accommodate the tunneling electron. All the electrons to the left must shift by one-half the average inter-electron spacing along the wire. Similarly, all the electrons to the right of the tunneling electron must shift away towards the right by an equal amount. Thus, there is an energy cost associated with disturbing the collective line of electrons on both sides of the tunneling electron. If the tunneling electron were instead entering from the end of the wire, a process known as “end tunneling,” and not from more centrally located in the wire, known as “bulk tunneling,” the large number of electrons must all shift away from the end by the entire inter-electron spacing. In terms of electron wavefunctions, the free electron-like quasiparticle is not a proper excitation of the Luttinger liquid, so the creation of an additional electron in the 1D system requires the wavefunctions of all the electrons in the liquid to be modified. This wavefunction transformation reflects an orthogonality catastrophe (Fisher 1996) and the tunneling density of states is thus severely suppressed in the presence of such Coulomb interactions. This is in contrast to a 3D conducting system, where a tunneling electron will cause a less collective disruption of the Fermi sea of electrons by resulting in a quick redistribution of the electrons that are free to move around and rearrange themselves in all directions.

Thus, due to this collective effect in 1D, there is a strong suppression of the tunneling rate for electrons entering a 1D channel around zero-bias, a feature known as a zero-bias anomaly (ZBA), while the tunneling rate into a conventional 3D metal at zero-

bias should neither be suppressed nor enhanced. The zero-bias anomaly can be experimentally observed in the differential conductance, dI/dV , where I is the current and V the voltage, of a tunnel junction attached to a 1D wire. A minimum in the differential conductance around zero-bias, $V_{dc} = 0$, is predicted for a Luttinger liquid. The differential tunneling conductance obeys a power-law in voltage, $dI/dV \propto V^\alpha$, and the zero-bias conductivity follows a power-law in temperature for small finite bias, $G \propto T^\alpha$ (Kane 1992). These power-law dependencies have been predicted and measured for single-walled carbon nanotubes with tunneling both into their end as well as into their bulk (Bockrath 1999, Yao 1999, Postma 2000). The seminal measurements of the Luttinger liquid state in carbon nanotubes were by Bockrath *et al.* (1999) who measured single-walled carbon nanotube ropes contacted by metallic leads in two different geometries. In one case the metal electrodes were deposited on top of the nanotube, effectively ending the nanotube at the contact. (Electrons in the nanotube possess nearly zero probability of traveling within the nanotube while under the electrode, so any current will remain in the electrode until it must tunnel into the nanotube.) This is known as “end” contact because a tunneling electron tunnels into the “end” of the Luttinger liquid. Thus, the charging energy associated with this configuration is determined only by the length of the nanotube between the leads. Electrodes evaporated on top of the nanotube can be invasive and introduce barriers into the nanotube via damage during the lithography processing. The devices discussed later in this thesis are of this “end” type. The alternate configuration is where prefabricated contact electrodes are instead below a nanotube positioned on-top and the electrons are able to tunnel into any location of the nanotube. This is referred to as “bulk” contact and often results in a high contact resistance due to

weak coupling between the electrode and nanotube. Additionally, mechanical bending of the nanotube over the contacts may create successive quantum-dots within the nanotube and also contribute to a large resistance. The detailed nature of these contact barriers remains unclear, but they provide tunnel junctions even at high temperature.

The exponent α quantifies the electron-electron interaction strength. These different values for tunneling into the end of the system or the middle of the system are related to an order parameter g , known as the Luttinger parameter, which quantifies the strength and sign of electron-electron interactions.

$$\alpha_{end} = \frac{g^{-1} - 1}{4}$$

$$\alpha_{bulk} = \frac{g^{-1} + g - 2}{8}$$

$$g = \left[1 + \frac{2E_c}{\delta E} \right]^{-\frac{1}{2}}$$

where E_c is the electrostatic Coulomb charging energy of the system and δE is the mean orbital single-particle energy level spacing (Bockrath 1999). In the case of repulsive interactions $g < 1$, for noninteracting systems $g = 1$, and $g > 1$ for systems with attractive interactions, such as those in superconducting materials. Predictions have established the Luttinger parameter value to be $g \sim 0.28$ for metallic or heavily doped semiconducting nanotubes (Bockrath 1999). Relating α to g gives $\alpha_{end}(\text{theory}) \sim 0.64$ and $\alpha_{bulk}(\text{theory}) \sim 0.23$, in agreement with the experiment on bundles of carbon nanotubes, shown in Figure 2.1, which observes a power-law of the conductivity and temperature for both end and

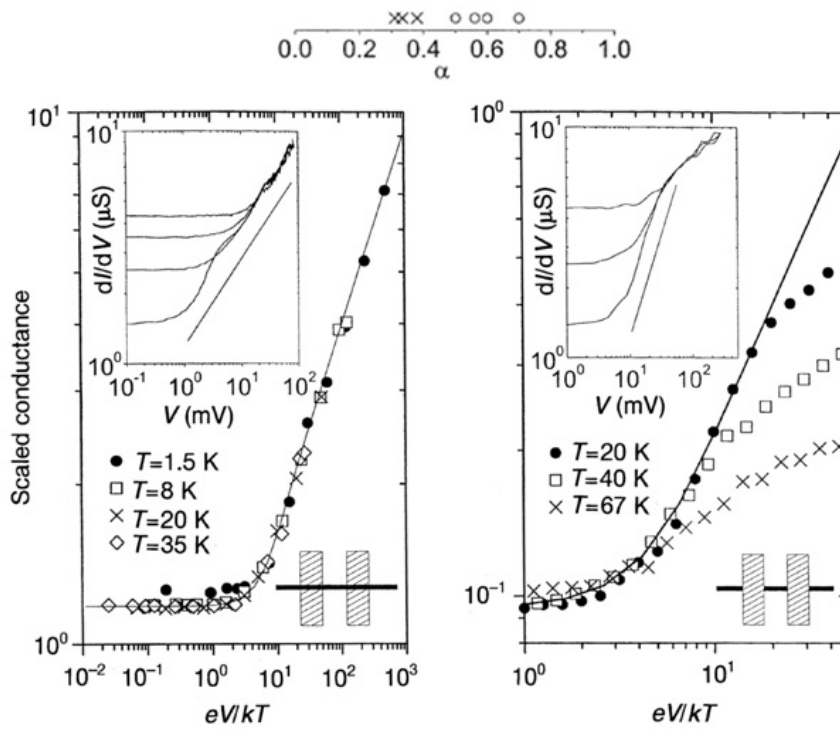


Figure 2.1 – Previous reports observed a power-law dependence of the scaled conductance as a function of applied voltage and temperature for both bulk and end contacts to single-walled carbon nanotube ropes. The top figure shows the variety of power values obtained for the two different contact scenarios, bulk-contacted (crosses) and end-contacted (open circles). The left log-log plot shows tunneling into the bulk with the nanotube ropes on top of the metal contracts (bulk contact), while the right plot shows a nanotube rope under the contacts (end contact). For both scenarios, the data taken at various temperature collapse onto a single curve which is consistent with Luttinger-liquid theory, but can also be explained by other phenomenon (adapted from Bockrath 1999).

bulk contacts with extracted $\alpha_{\text{end}} \sim 0.5-0.7$ and $\alpha_{\text{bulk}} \sim 0.3-0.4$. The authors conclude that these results show agreement with the predictions for tunneling into a Luttinger liquid.

However, applications of the theoretical models can be strongly dependent on the system considered and the assumptions. Theory which includes Umklapp scattering yields an $\alpha = 1-2g$ and, if disorder is accounted for, one finds $\alpha = (1-g)/2$ (Kane 1997). Also, the Luttinger parameter may be affected by the inhomogeneity of the system at the boundaries between a 1D Luttinger Liquid and 3D Fermi Liquid system, such as a nanotube and a metallic contact reservoir, creating a modified effective g parameter (Sandler 1998, Chamon 1997). Other experiments of crossed metallic nanotubes (Yao 1999, Gao 2004) and kinked metallic nanotube observed similar bulk and end tunneling between 1D systems, and photoemission studies on nanotube bundles also attempted to extract the Luttinger parameter g (Ishii 2003), but it is very challenging to measure g without additional effects due to the contacts. Furthermore, the temperature, bias voltage, and gate voltage dependence of a random telegraph signal resulting from an electron between a semiconducting nanotube and a nearby defect were analyzed finding, a value of $g < 0.2$ (Tobias 2007). The various theories and previous experiments which have attempted to predict or measure g of nanotubes or other 1D systems are presented in Table 2.1. This variety in theoretical modeling for the expected power-law suppression of tunneling into a nanotube poses a challenge for definitively understanding the range of experimental results for studies of this type.

These experiments have received varied reactions; some believe these are convincing demonstrations of collective Luttinger liquid behavior, while others consider them to only provide circumstantial evidence that may be explained by other means.

Table 2.1 – Table of Luttinger parameter g values reported for carbon nanotubes and other 1D systems.

Publication	Method	Theory or Experiment	1D Signature	Luttinger Parameter g
Egger (1998)	Low-energy theory for SWCNTs including Coulomb interactions	Theory	Coulomb interaction	0.2-0.4
Kane (1998)	Coulomb interactions and mesoscopic effects in an isolated SWCNT	Theory	Power-law tunneling	0.2
Egger (1999)	Low energy theory including the long-ranged Coulomb interactions, internal screening effects, and single-electron hopping for MWNT/SWCNT ropes	Theory	Power-law tunneling	0.46/0.36 (end bulk) 0.24/0.24 (end bulk)
Bockrath (1999)	Tunneling into CNT bundles	Experiment	Power-law tunneling	0.26-0.33
Yao (1999)	Intramolecular junctions in SWCNT	Experiment	Power-law tunneling	0.22
Auslaender (2000)	<i>Tunneling between 1D quantum wires in GaAs</i>	<i>Experiment</i>	<i>Power-law tunneling</i>	<i>0.66-0.82</i>
Postma (2000)	Tunneling through CNT kink	Experiment	Power-law tunneling	0.26
Bae (2001)	Transport in aligned SWCNT film	Experiment	Power-law tunneling	0.18-0.26
Tarkenton (2001)	MWNT end contact tunneling	Experiment	Power-law tunneling	0.5, $\alpha \approx 0.12-0.32$
Postma (2001)	Sequential tunneling through CNT quantum dot islands	Experiment	Power-law tunneling	0.23
Thorstent (2001)	CNT intramolecular dot tunneling	Theory	Power-law tunneling	0.23
Auslaender (2002)	<i>Tunneling between 1D quantum wires in GaAs</i>	<i>Experiment</i>	<i>Power-law tunneling</i>	<i>0.75</i>
Ishii (2003)	Photoemission spectroscopy on CNT bundles	Experiment	Power-law tunneling	0.18
Shtraiht (2003)	Tunneling into SWCNT networks	Experiment	Power-law tunneling	0.26
Kanf (2004)	Photoemission in SWCNT mats	Experiment	Power-law tunneling	0.18
Lee (2004)	Real Space Imaging of electronic standing waves on SWCNTs	Experiment	Spin-charge separation	0.55
Gao (2004)	Transport through crossed metallic SWCNTs	Experiment	Power-law tunneling	0.16
Hanger (2004)	Transport in SWCNT ropes	Experiment	Power-law tunneling	$\alpha \approx 0.1-0.9$
Lin (2005)	<i>Transport in 1D In_2O_3 nanowires</i>	<i>Experiment</i>	<i>Power-law tunneling</i>	<i>0.43</i>
Auslaender (2005)	<i>1D quantum wires in GaAs</i>	<i>Experiment</i>	<i>Spin-charge separation</i>	<i>0.3, $v_s = 0.8v_F$</i>
Hansson (2005)	Calculation of CNT as antenna elements	Theory	Spin-charge separation	0.13
Hani (2006)	Quantum capacitance in SWCNT	Experiment	Quantum capacitance	0.26-0.34
Dora (2007)	NMR of double-walled CNTs	Experiment	Spin-lattice relaxation rate	0.2
Tobias (2007)	Noise in semiconducting CNTs	Experiment	Power-law tunneling	<0.2
Kim (2007)	Conductance and shot noise in SWCNTs	Experiment	Power-law tunneling	0.22-0.26
Zhong (2008)	Ballistic electron resonances in individual p-n-p cavity semiconducting nanotube	Experiment	Spin-charge separation	1
Jompol (2009)	<i>Electrically gated 1D system from ZDEG</i>	<i>Experiment</i>	<i>Spin-charge separation & power-law tunneling</i>	<i>0.7 0.28</i>
Tanaka (2010)	Tunneling in SWCNT networks	Experiment	Power-law tunneling	0.3 (bulk)
Parkash (2010)	Calculation of Quantum Capacitance of SWCNTs	Theory	Quantum Capacitance	0.14-0.33
Hara (2010)	NMR spin-lattice relaxation in CNT bundles	Experiment	Power-law tunneling	0.34
Barak (2010)	<i>Tunneling in double wire system</i>	<i>Experiment</i>	<i>Charge fractionalization</i>	<i>0.55</i>
Wakabayashi (2011)	Wiedemann-Franz violation of quasi-1D $\text{Li}_0.5\text{Mo}_2\text{O}_7$	Experiment	Power-law tunneling	0.25
Yan (2012)	<i>ZBA in 1D metallic Au/Ag nanowire</i>	<i>Experiment</i>	<i>Power-law tunneling</i>	<i>Exclude LL behavior</i>
Hortensius (2012)	Thermovoltage in suspended CNT	Experiment	Power-law tunneling	0.25 (bulk)
Sedlmayr (2013)	Conductance of interacting quantum wires with scattering	Theory/Experiment	Power-law tunneling	2.4 (unphysical)
Present Work	Tunneling through ZBA	Experiment	Power-law tunneling	$\alpha \approx 0.1-0.8$
Present Work	THz Standing wave resonances	Experiment	Spin-charge separation	1, $\approx 0.7, 0.3$

Other possible descriptions include dynamical Coulomb blockade theory or the possible presence of disorder, which can occur in highly resistive, conventional non-1D conductors and can also impede the spreading of charge due to tunneling electrons. The observed effect may also be due to a ZBA in resistive 3D leads. Dynamical Coulomb blockade, the interaction of tunneling electrons with their electromagnetic environment (Devoret 1990), is a leading alternative interpretation for the power-law behavior observed by Bockrath. This environmental quantum-fluctuation theory treats the electrodes and nanotube as conventional Fermi liquids and includes the Johnson-Nyquist noise due to the coupling of energy between an electron and its environment. These electric circuit fluctuations can induce effective repulsive interactions between electrons. However, the differences in the predicted tunneling power-law suppression of this effective environment effect and that of tunneling into a Luttinger liquid are difficult to differentiate (Sonin 2001, Jezouin 2013). Furthermore, experiments on multi-walled carbon nanotubes (Bachtold 2001, Tarkiainen 2001, Yi 2003) yielded very similar results to the single-walled nanotube experiments, with a power-law observed for an unexpectedly wide range of biases and despite adjusted predictions (Egger 2001) of behavior for multi-walled nanotubes accepted as disordered multichannel wires (Mishchenko 2001). Thus, a host of possible explanations, only one of which is Luttinger liquid behavior, can be used to describe the observed power-law dependence of electron tunneling into carbon nanotube devices.

2.2.2 Power-Law Measurement Results

As a part of this thesis work, the electrical conductance of individual single-walled carbon nanotubes was measured at various temperatures and plotted as in previous experiments. It is predicted that measurements of the conductance of a 1D system taken at different temperatures should collapse onto a single universal curve when scaled by the temperature raised to the α power and plotted versus the bias scaled by the thermal energy, $k_B T$, where k_B is Boltzmann's constant (Bockrath 1999). This was indeed reported and shown in Figure 2.1. We have examined several samples of different lengths, varying resistances (depending on intrinsic behavior as well as bias conditions), as well as contact geometries. All samples studied exhibit a ZBA at low temperature and low bias voltage and are intended to possess Ohmic contact rather than tunneling contacts. There are frequently two classes of samples: those with a moderate ZBA where there is a relatively small increase in resistance around zero-bias, as shown in the inset of Figure 2.2a, or those with a very pronounced ZBA where there is an increase in the resistance by at least an order of magnitude around zero-bias, as shown in the inset of Figure 2.2b. The scaled conductance G/T^α of two devices, one from each of these categories, plotted as a function of $eV/k_B T$, is shown in Figure 2.2a and 2.2b. Despite the sought after Ohmic contacts of our devices, we follow the power-law scaling approach of Bockrath to examine if this ZBA feature is a possible reflection of Luttinger liquid behavior in our individual single-walled carbon nanotube samples. We find α values of 0.2 and 0.5 for the two devices shown, corresponding to g values of ~ 0.6 and ~ 0.3 . This second value is close to the theoretical prediction and corresponds to a device with a more extreme increase in resistance around zero bias. This may make this sample more fitting with the assumed electron tunneling behavior into the nanotube, but may also just be a reflection of poor

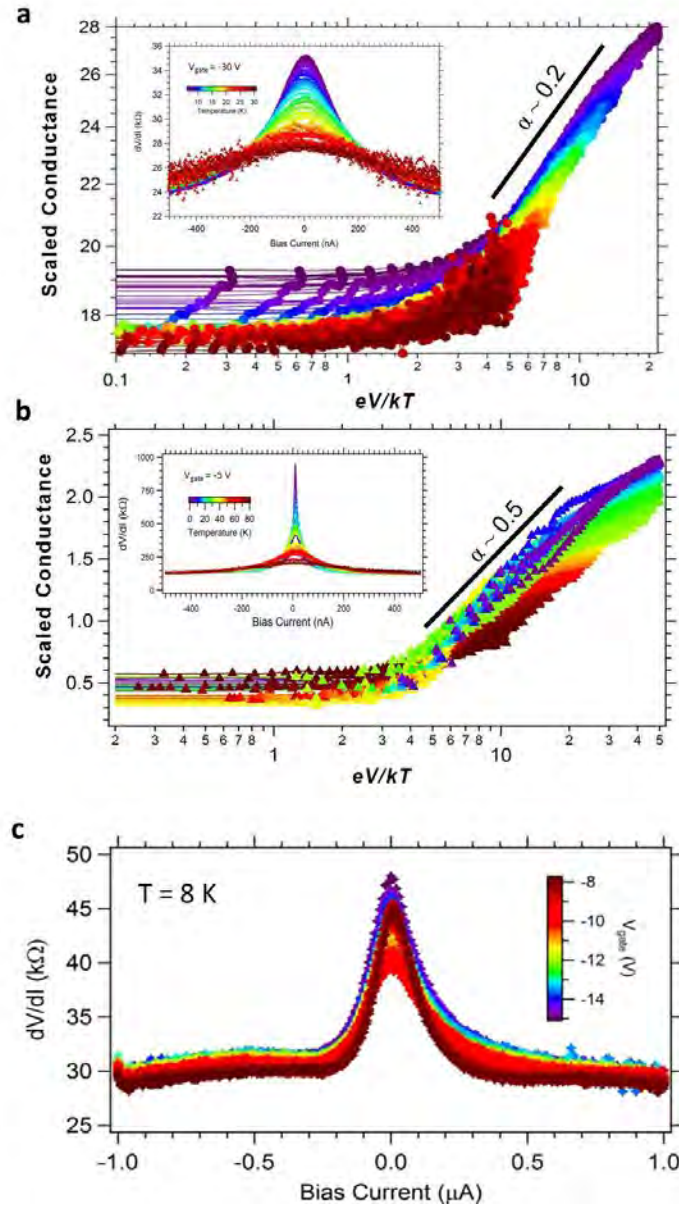


Figure 2.2 – Plots of the scaled conductance as a function of eV/kT for two different individual carbon nanotube end-contacted devices at varying temperature. The inset shows the shape of the zero-bias anomaly (ZBA) that develops as the temperature decreases characterized by an increase in the differential resistance around zero bias. (a) shows a device exhibiting a moderate ZBA with only a small increase in resistance around zero bias while (b) shows a device with a very dramatic ZBA. The scaled conductance can be fit with a power-law dependence on eV/kT with varying values of α for these dramatically different devices studied; for these two devices this corresponds to g values of ~ 0.6 and ~ 0.3 . The lower value is closer to the theoretical prediction and corresponds to a device with likely poorer electrical contact. (c) Differential resistance of an individual carbon nanotube device at low temperature as a function of bias current at various gate voltages showing that the choice of applied gate voltage can alter the shape of the zero-bias anomaly and thus the power-law exponent. This would indicate that the ZBA is a contact effect not simply related to Luttinger liquid behavior. The diversity of shapes for the ZBA and corresponding collection of power-law fits highlights the difficulty in using this method as a means of demonstrating Luttinger liquid behavior in carbon nanotubes.

electrical contact. We find a wide-range of values for α , from 0.1 to 0.8, for the individual single-walled carbon nanotube devices studied ranging in length from 1 to 5 μm yielding a variety of corresponding g values for this system. Furthermore, as shown in Figure 2.2c, the choice of applied gate voltage for single-walled nanotube devices can alter the shape of the ZBA and thus the power-law exponent to describe this behavior. In addition, an asymmetry between positive and negative bias can be seen, indicating the complex nature of the contacts with contributions beyond only electron-electron interactions, which would be expected to be symmetric, as the origin of this behavior. Thus, the collection of varied results ascribed to several possible explanations, reported in the literature and from our work, maintains the puzzle of Luttinger liquid behavior physics in carbon nanotubes an open question and require a direct method of measuring the Luttinger parameter within an individual carbon nanotube.

2.2.3 Plasmon Velocity

Another signature of the correlated behavior of electrons when confined to one dimension is the phenomenon of spin-charge separation. The electron system supports collective excitations of waves of electron charge density and distinct uncharged waves, often referred to as waves of electron spin density, which propagate with two different velocities (Burke 2002). This manifestation of spin-charge separation has been experimentally observed using a technique of momentum-conserved electron tunneling between parallel nanowires (Auslaender 2005), and also in measurements on an electrostatically gated 1D system, which report observation of spin-charge separation and

the predicted power-law suppression of tunneling into the 1D system (Jompol 2009). As we will see, the propagation characteristics of the charge-carrying excitations in 1D systems, termed plasmons, are dependent on the strength of the electron-electron interactions. These waves are predicted to travel at a propagation velocity of charge transport $v_p = v_F/g$, where for carbon nanotubes the Fermi velocity is $v_F = 8 \times 10^5 \text{ m/s}$. The spin transport velocity for the uncharged excitations is expected to simply be the Fermi velocity v_F . Thus, since $g < 1$ for repulsive electron-electron repulsion, the plasmon velocity is predicted to be *faster* than the Fermi velocity. An experiment to measure these different propagation velocities in an individual single-walled carbon nanotube using time-domain measurements only observed propagation at the Fermi velocity (Zhong 2008). Recent work has also endeavored to further the description of 1D quantum fluids by going beyond the low-energy limit of the Luttinger Liquid paradigm (Ngai 2011, Imambekov 2012). In the work described in this thesis, we attempt to advance this understanding of the Luttinger liquid behavior of carbon nanotubes by measuring the faster plasmon charge mode velocity utilizing a model of a nanotube as a high-frequency transmission line.

2.3. Transmission Line Model of a Carbon Nanotube

A transmission line model of a single-walled carbon nanotube was first proposed by Bockrath (Bockrath 1999b) in 1999, and detailed predictions were presented by P.J. Burke in 2002 (Burke 2002). The main consequences of treating a nanotube as a transmission line are the presence of the expected transmission line properties, including

phase velocity v_p and characteristic impedance Z_o . Burke carefully derived the relevant values for a single-walled carbon nanotube transmission line. Others have tried to determine them experimentally through challenging measurements (Ilani 2006, Plombon 2007).

2.3.1 Transmission Line Model

The basis for understanding the high-frequency properties comes from considering a single-walled carbon nanotube with a diameter d separated a distance h from a nearby ground plane. This is a typical transmission line configuration. The presence of the ground plane (conducting substrate) prevents long-range Coulomb interactions for distances greater than the screening length $2h$. A single conduction channel can be modeled with the effective circuit given in Figure 2.3a as an infinite series of distributed parallel inductances and capacitances. Included in this equivalent circuit model, in addition to the typical *electrostatic capacitance*, C_{ES} , for a wire and a ground plane, and the standard *magnetic inductance*, L_M , there is a *quantum capacitance*, C_Q , accounting for the energy needed to add an extra electron to the nanotube, as well as a *kinetic inductance*, L_K , accounting for the kinetic energy stored in the motion of the nanotube charge carriers. This theoretical model of a transmission line is consistent with Luttinger liquid theory, which describes the interacting electrons in a 1D system. We begin by investigating each of the relevant parameters included in this distributed model of a carbon nanotube transmission line.

2.3.2 Electrostatic Capacitance

The electrostatic capacitance C_{ES} per length between the nanotube and the ground plane can be calculated by computing the capacitive energy, the stored electrostatic energy. It is important to note that the effects of electron-electron interactions are included in C_{ES} .

Following the treatment in Burke, the electrostatic capacitance per unit length, C_{ES} , of a long conducting cylinder of diameter d separated from a ground plane by a dielectric of thickness h and dielectric constant ϵ is approximated by

$$C_{ES} \approx \frac{2\pi\epsilon}{\ln\left(\frac{h}{d}\right)}.$$

For silicon dioxide $\epsilon = 3.9$ and for a nanotube of diameter $d = 2$ nm, and a typical dielectric thickness of 100 nm, we estimate the electrostatic capacitance per unit length $C_{ES} \approx 50$ aF/ μm (Burke 2002).

2.3.3 Quantum Capacitance

The quantum capacitance per unit length C_Q results from the finite energy needed to add an extra electron to the 1D system due to the quantized energy levels possessing a limited number of states. Adding an electron to a classical (three-dimensional) electron gas of large volume costs a negligible amount of energy. In contrast, for a quantum electron gas, one can only add an electron to an available quantum state above the Fermi energy as a result of the Pauli exclusion principle. Such an addition has an energy cost associated with it. Equating the quantization of the 1D system's energy levels to the quantum

capacitive energy yields an effective quantum capacitance (Burke 2002). For a 1D system with a linear dispersion relation, such as a nanotube, the single-particle energy level spacing is $\delta E = \frac{dE}{dk} \delta k = \frac{h v_F}{\ell}$, and equating it with the quantum capacitive energy (including spin degeneracy):

$$\delta E = \frac{h v_F}{\ell} = \frac{2e^2}{C_Q}$$

where e is the electron charge, h is Plank's constant, v_F is the Fermi velocity, and ℓ is the length of the 1D system. We can solve for C_Q to obtain a capacitance per unit length of:

$$\frac{C_Q}{\ell} = \frac{2e^2}{h v_F} \approx 100 \frac{\text{aF}}{\mu\text{m}}$$

C_Q is only related to fundamental constants and the Fermi velocity of the nanotube. This value was experimentally confirmed by Ilani *et al.* (Ilani 2006) with measured values of the total capacitance ~ 100 aF/ μm per channel. Comparisons to analytical and numerical models were performed by Liang *et al.*, who found good agreement (Liang 2008). The electrostatic capacitance and quantum capacitance are in series, as shown in Figure 2.3a. In bulk metallic conductors $C_Q \gg C_{ES}$ (the quantum charging energy is small), so the electrostatic capacitance dominates. However, in reduced dimensions, such as a nanotube over a ground plane, due to the low density of states, the quantum capacitance is comparable in magnitude to the electrostatic capacitance. The quantum capacitance can be thought of as accounting for the intrinsic charge storage, whereas the electrostatic capacitance accounts for the electric field (Wong 2011) and both the electrostatic and

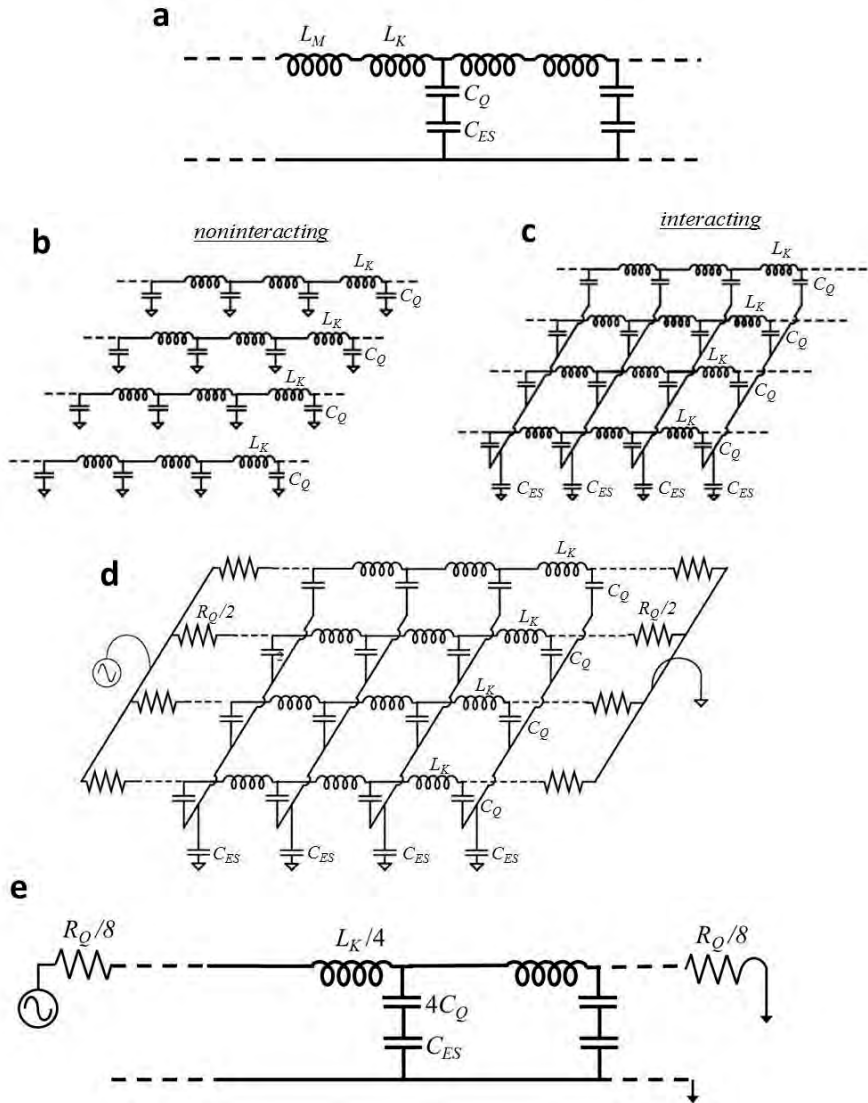


Figure 2.3 – (a) Circuit diagram of a quantum channel as a nanotransmission line with distributed magnetic L_M and kinetic L_K inductances with parallel distributed quantum C_Q and electrostatic C_{ES} capacitances. (b) Circuit model of a single-walled carbon nanotube with noninteracting electrons composed of four quantum channels in parallel. The lack of C_{ES} is equivalent to neglecting the electron-electron interactions. Note that the magnetic inductance is ignored since the kinetic inductance dominates for a carbon nanotube as explained in the text. (c) Circuit model for interacting electrons in a single-walled carbon nanotube where C_{ES} couples the four channels. Considering applying an ac voltage to this line leads to four fundamental excitations: one common mode which carries a net current (plasmon mode) as well as three neutral modes which do convey any net current. This represents separation of spin and charge as is expected in a strongly interacting Luttinger liquid 1D system. Exciting voltage waves on the transmission line is equivalent to directly exciting one dimensional plasmons, the low energy excitations of the Luttinger liquid. (d) Circuit diagram of a single-walled carbon nanotube with dc electrical contacts corresponding to half of the quantum of resistance on each end of the four channels. (e) Effective circuit diagram consisting of a single transmission line for the charge mode of a single-walled carbon nanotube possessing rescaled inductance and capacitances. The wave velocity of this effective circuit is the same as the wave velocity of the common mode for all four channels (adapted from Burke 2002).

quantum capacitances must be considered in the transmission line model for a nanotube (Burke 2002).

2.3.4 Magnetic and Kinetic Inductance

In bulk conductors, the frequent scattering of electrons limits the drift velocity of such charge carriers, but the large number of carriers still produces a large electrical current. The kinetic energy of the charge carriers is very small, so the magnetic field created by the current flow, with its associated magnetic energy, dominates the inductance. From basic electromagnetics, the magnetic inductance L_M is simply calculated by setting the inductive energy equal to that stored in magnetic energy. For a typical nanotube above a conducting plane, the magnetic inductance per unit length, L_M , is estimated to be 1 pH/ μm .

An additional energy is the kinetic energy. For normal conductors, electrons frequently scatter and lose their kinetic energy, making any contribution of this energy negligible. However, in cases where electrons travel without loss, such as in superconductors, or in a system with a limited number of carriers and weak internal scattering, such as the carbon nanotube, the carriers travel with high velocity, and there is significant energy stored in the inertial motion of the charge. The kinetic inductance L_K , as examined by Rutherglen and Burke (Rutherglen 2009), is calculated from the energy increase of the system to generate a finite current composed of a higher population occupying forward-moving states than occupying backward-moving states. The energy difference between the highest occupied forward-moving states and the highest occupied

backward-moving states is given as $\Delta\mu$. The current for a single quantum channel is this energy difference divided by the resistance quantum yielding a total current $I = \Delta\mu(\frac{e^2}{h})$. The energy cost to then generate this total current can also be calculated by multiplying the number of promoted electrons N by the energy added to each electron δE . The 1D energy level spacing is given as earlier with $\delta E = \frac{hv_F}{\ell}$. Accounting for spin degeneracy, the excess number of electrons in forward-moving states due to a $\Delta\mu$ potential is:

$$N = \frac{e\Delta\mu}{2\delta E} = \frac{e\ell\Delta\mu}{2hv_F}$$

and because each electron adds $\delta E=(e\Delta\mu/2)$, the Fermi energy level increase of the right movers, the total energy added by the current is:

$$E = \frac{e^2\Delta\mu^2\ell}{4hv_F}$$

Treating this current energy cost as an inductive energy yields:

$$E = \frac{e^2\Delta\mu^2\ell}{4hv_F} = \frac{1}{2}L_K I^2 = \frac{1}{2}L_K(\Delta\mu^2 \frac{e^4}{h^2})$$

and solving for inductance per unit length L_K , we find:

$$\frac{L_K}{\ell} = \frac{h}{2e^2v_F} \approx 16 \text{ nH}/\mu\text{m}$$

Note that this value of L_K is not for a nanotube, which possesses four quantum channels as described below. For a nanotube, the kinetic inductance per unit length dominates the magnetic inductance per unit length by four orders of magnitude. The magnetic

inductance will be ignored henceforth. The relatively large kinetic inductance per unit length of carbon nanotubes $\approx 4\text{nH}/\mu\text{m}$ has implications for their potential use in any high-frequency electronic circuits.

2.3.5 Four Parallel Channels

Carbon nanotubes possess two orbital conduction channels from the two K points arising from the two unique carbon atom basis of the hexagonal lattice. Each channel allows for electrons to be either spin up or spin down. Thus, the complete model is composed of four (connected) transmission lines in parallel. Figure 2.3b shows the circuit model of a single-walled carbon nanotube with noninteracting electrons composed of four quantum channels in parallel. The lack of C_{ES} is equivalent to neglecting the electron-electron interactions. Note that the magnetic inductance is ignored since the kinetic inductance dominates for a carbon nanotube. Figure 2.3c displays the circuit model for interacting electrons in a single-walled carbon nanotube where C_{ES} couples the four channels.

Considering applying an ac voltage to this line, Burke proves that these can accommodate four fundamental collective mode excitations, one of which conveys charge, known as a plasmon or charge mode, and three which are neutral due to no net transfer of charge, referred to as spinons or neutral modes (Burke 2002). This represents separation of spin and charge as is expected in an interacting Luttinger liquid 1D system. Additionally, the quantum resistance ($R_Q = h/4e^2 = 6.5\text{ k}\Omega$) as described in Chapter 1 for entering and exiting the 1D system from 3D contacts is incorporated for each quantum channel.

Considerations by Maslov and Stone demonstrate that the quantum resistance is not

expected to be modified by the electron-electron interactions present in a Luttinger liquid (Maslov 1995). The circuit diagram of Figure 2.3d shows a single-walled carbon nanotube with dc electrical contacts corresponding to the quantum of resistance split equally on each end of the four channels. This thesis focuses on the plasmon charge mode, and at high-frequency the nanotube picture can then be simplified into the effective circuit diagram of Figure 2.3e consisting of a single transmission line representing the charge mode of a single-walled carbon nanotube possessing rescaled inductance and capacitances. The wave velocity ($v = 1/\sqrt{LC}$) of this effective circuit is the same as the wave velocity of the common charge mode for all four channels. Exciting a high-frequency voltage wave along the nanotube transmission line is equivalent to collectively exciting a 1D plasmon, the low energy excitations of the Luttinger liquid.

2.3.6 Contact Resistance and Capacitance

We expand the model of Figure 2.3e beyond the intrinsic equivalent distributed circuit elements of a nanotube transmission line by including a term to account for damping due to electron scattering within the nanotube, denoted as an internal distributed resistance per unit length, r_{int} . Note that, as mentioned in Chapter 1, r_{int} for best case real nanotubes is found to be $\approx 1 \text{ k}\Omega/\mu\text{m}$ at low temperature. In addition to the quantum of resistance R_Q , an additional contact resistance R_c between the nanotube and electrodes, for the reasons previously outlined in Chapter 1, is included in parallel with a contact coupling capacitance C_c between the 3D metal electrodes and the nanotube. The contact resistance R_c arises from the imperfect transparency of the metal/nanotube interface; R_c is zero for a

perfect contact. Even though the associated contact capacitance C_c is in fact a distributed capacitance between the electrode and the entire length of the nanotube, it is modeled as a parallel lumped element here for simplicity. The complete equivalent circuit model is shown in Figure 2.4.

2.3.7 Intrinsic Impedance

Measurements of the high-frequency properties of such a system are quite challenging and extremely difficult due to the relatively high intrinsic impedance of such nanotube devices ($>6.5 \text{ k}\Omega$), which is incompatible with typical $50 \text{ }\Omega$ microwave test equipment. This serves as a major impediment to device testing at high frequency since most of an incoming signal is reflected due to the large impedance mismatch, greatly limiting device coupling efficiency. This issue can be overcome with appropriate impedance matching, but at the cost of limited bandwidth for measurement. Other groups have analyzed the high-frequency properties of thin-films or bundles of carbon nanotubes, which can have lower resistance than an individual nanotube; however, de-embedding the properties of individual nanotubes from measurements on such samples is extremely tricky.

One experiment was reported by Plombon *et al.* (2007), where they measured the reflection and transmission coefficient S-parameters up to 20 GHz of individual and bundled carbon nanotubes. The small signal level was near the experimental noise floor due to the large intrinsic impedance of nanotubes. Thus, the effects due to the nanotubes were difficult to differentiate from any reference standard, resulting in substantial uncertainties in the extracted equivalent circuit parameters for the nanotube.

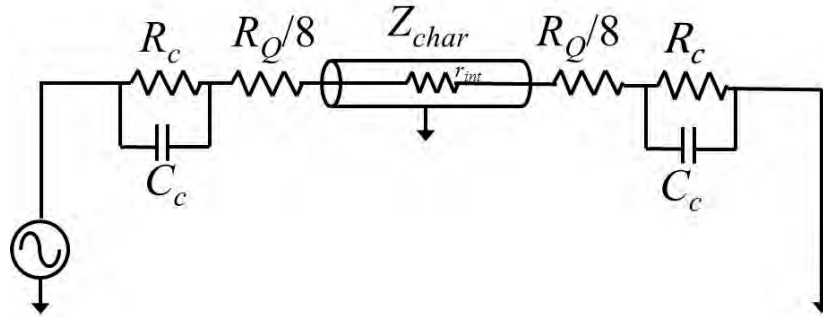


Figure 2.4 - Equivalent circuit model of a single-walled carbon nanotube possessing characteristic impedance Z_{char} and internal distributed resistance per unit length r_{int} as well as quantum R_Q ($=26 \text{ k}\Omega$) and contact R_c resistances with parallel contact capacitance C_c . The internal resistance leads to damping of the 1D plasmon along the length of the nanotube.

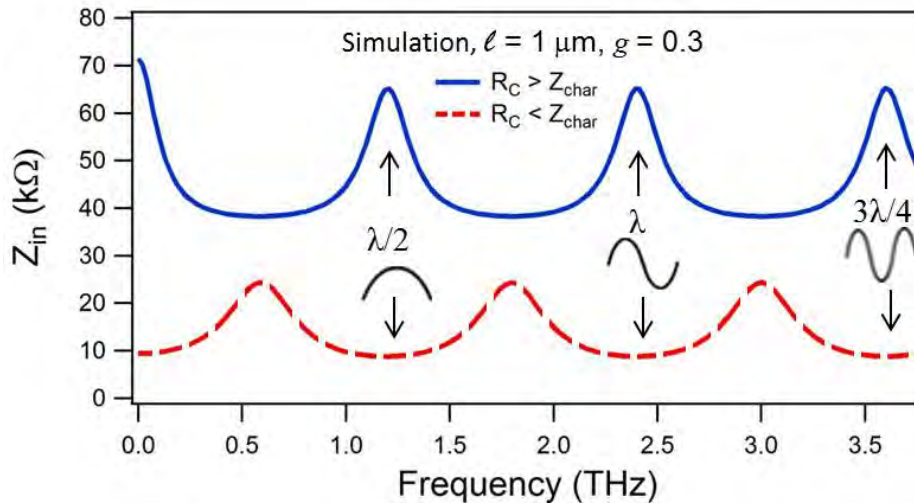


Figure 2.5 – Predicted THz frequency dependent impedance for a carbon nanotube using the effective circuit described above. This plot corresponds to a nanotube $1 \mu\text{m}$ long and with an assumed Luttinger parameter g of 0.3 and $C_c = 0$. This model predicts periodic standing wave resonances will appear in the finite length nanotube when there is an integral multiple of a half wavelength on the nanotube. This frequency location of this resonant behavior allows for the calculation of the wave velocity of 1D plasmon and hence a direct measurement of the Luttinger parameter g . This is similar to the general rf engineering result of quarter wavelength structure transforming an open circuit to short circuit and vice versa. Here, the termination of the nanotube transmission line, namely the ratio of the line characteristic impedance to the contact resistance, determines whether the standing wave resonance will produce an impedance minima or maxima.

2.3.8 Plasmon Velocity and Characteristic Impedance

Treating a nanotube as a transmission line enables a straightforward determination of the wave velocity and characteristic impedance. The development of spin-charge separation, characterized by a modified wave velocity for charge transport when compared to the spin mode, can be readily visualized from this transmission line approach. Examining the simplified transmission line model of Figure 2.3e, if we only include C_Q (excluding C_{ES}), then this situation is essentially describing a 1D system possessing no electron-electron interactions. This would be the case for the neutral modes. Given the equations determined above, calculating the wave velocity of such a transmission line,

$v_{1D,noninteracting} = 1/\sqrt{L_K C_Q} = v_F$, it is clear that the velocity of this mode is equal to the Fermi velocity. If repulsive electron-electron interactions are now accounted for with the inclusion of C_{ES} , the wave velocity for the four parallel channels is found to be *greater* than v_F ,

$$\begin{aligned} v_{1D,interacting} &\approx \sqrt{\frac{1}{\frac{L_K}{4} C_{tot}}} \\ &\approx \sqrt{\frac{4}{L_K C_{ES}} + \frac{1}{L_K C_Q}} > v_F \end{aligned}$$

The ratio of these two velocities is the dimensionless Luttinger parameter g , which quantifies the strength of the electron-electron interaction,

$$g \equiv \frac{v_F}{v_{1D,interacting}} = \sqrt{\frac{C_{tot}}{4C_Q}}.$$

The Luttinger parameter g can be determined via a capacitive relation comprised of C_Q and C_{ES} expressing the reduction of the electron-electron interactions by the screening of the electrostatic Coulomb force. Using the total capacitance per unit length $C_{tot} =$

$\frac{C_Q C_{ES}}{C_Q + C_{ES}}$, g can be equivalently defined as:

$$g = \sqrt{\frac{C_{tot}}{4C_Q}} = \sqrt{\frac{C_{ES}}{4(C_Q + C_{ES})}}.$$

For a very weakly interacting system, $C_{ES} \gg C_Q$, $C_{tot} \rightarrow C_Q$, gives $g = 1$, whereas for a strongly interacting system, $C_{ES} \ll C_Q$, $C_{tot} \rightarrow C_{ES}$, $g \rightarrow 0$.

We can measure the faster charge mode propagation velocity, the plasmon velocity, by exciting a high-frequency signal on a finite-length nanotube. We can thereby characterize the Luttinger parameter g and the strength of the substantial electron-electron interaction in this 1D system.

2.3.9 Standing Wave Resonances

For a finite nanotube of length L , standing wave resonances will occur when the length corresponds to integral multiples of half-wavelengths. This situation occurs when $L = n \frac{\lambda}{2} = n \frac{v_p}{2f} \Rightarrow f_n = n \frac{v_F}{2Lg}$, so the frequency spacing $\Delta f = \frac{v_F}{2Lg}$ is related to g . Thus, by determining the frequencies of the standing wave resonances on the nanotube, one can straightforwardly determine g by using the known nanotube length and Fermi velocity. We measure the propagation velocity in the frequency domain by examining power coupling to the nanotube. This can be understood by examining the properties of standing

waves on a mismatched line. For a finite length nanotube, if a quarter-wavelength corresponds to the length, the input impedance will be large if the terminating resistor is smaller than the characteristic impedance Z_o resulting in less power coupling to the nanotube. This behavior repeats for odd integral multiples of a quarter-wavelength, so treating the nanotube as a transmission line predicts significant frequency dependence of dynamical impedance and we see resonant structure corresponding to quarter-wave transformer. A representation of these resonances is shown in Figure 2.5.

The properties of a transmission line are frequently characterized by two parameters, the characteristic impedance Z_o conveying the conditions for optimal signal propagation, and a propagation constant β which characterizes the attenuation and dispersion of a signal as it travels along the line. The characteristic impedance and propagation constant can vary with frequency. From transmission line theory (Pozar 2005), the input impedance Z_{in} of a lossless transmission line terminated with a load impedance Z_L is given by:

$$Z_{in} = Z_o \frac{Z_L + jZ_o \tan[\beta\ell]}{Z_o + jZ_L \tan[\beta\ell]}$$

where ℓ is the transmission line length. Considering the special length $\ell = \lambda/2$, corresponding to $\beta\ell = (2\pi/\lambda)(\lambda/2) = \pi$, the $Z_{in} = Z_L$. For a length of a quarter-wavelength with $\beta\ell = (2\pi/\lambda)(\lambda/4) = \pi/2$, evaluating this in the limit that $\beta\ell \rightarrow \pi/2$, the $Z_{in} = \frac{Z_o^2}{Z_L}$. This configuration is known as a quarter-wave transformer because it effectively transforms the load impedance depending on the characteristic impedance and allows one to match the transmission line and load at a specific frequency. Single-walled

carbon nanotubes are expected to operate as lossy transmission lines at GHz and lower frequencies and gradually transition to low-loss transmission lines at sub-THz frequencies (Wong 2011). In terms of distributed circuit parameters, the characteristic impedance is $Z_o = \sqrt{\frac{L_K}{C_{tot}}}$ which is a purely real frequency-independent constant.

Applying this to a nanotube gives $Z_o = \frac{1}{g} \sqrt{\frac{L_K}{C_Q}}$, which is dependent on g , the electron-electron interaction parameter. For the four parallel quantum channels in an individual nanotube with an assumed $g = 0.3$, $Z_o \sim 15 \text{ k}\Omega$.

2.3.10 Microwave test of v_p

It would be ideal to analyze these predictions in an easily measurable framework. The microwave regime ($\sim 10 \text{ GHz}$) is a well-established high-frequency range offering many standard measurement systems and approaches. Inspection of the frequency spacing equation shows that to observe resonant frequencies of $\sim 10 \text{ GHz}$ with an assumed $g = 0.3$ the corresponding carbon nanotube devices must be long, measuring $\sim 100 \text{ }\mu\text{m}$. Yu & Burke measured the dynamical conductance up to 10 GHz of single-walled carbon nanotubes with lengths over $100 \text{ }\mu\text{m}$ and did not observe any strong resonant behavior, attributing this to the damping of the plasmons by the large internal resistance $> 100 \text{ k}\Omega$ (Yu 2005). This poses a significant technical challenge since the unavoidable large distributed internal resistance within a long nanotube, as explained in Chapter 1, will damp out the sought after resonances. The scattering length, due to electron-phonon interactions, in a high-quality single-walled carbon nanotube is about $1 \text{ }\mu\text{m}$ at room-

temperature. In the low temperature limit the scattering length is likely due to impurities and can be as large as 10 μm (Purewal 2007). For a nanotube with greater defect densities, the scattering length will be shorter. Such scattering will dissipate the plasmon in a long nanotube and prevent the formation of the standing wave resonances. Thus, short nanotubes on the order of a few microns measured at low temperature are necessary in order to observe predicted standing wave resonances.

2.4 Terahertz Time-Domain Measurement

One experiment performed by Zhong *et al.* (2008) sought to measure the plasmon velocity of a short nanotube. They used THz time-domain reflectometry as shown in Figure 2.6a. This is a technique that probes material properties via short pulses of THz radiation. The experiment involved measuring the propagation velocity by creating short pulses launched into a nanotube, with pulse length less than a picosecond. This experiment utilized an individual semiconducting carbon nanotube channel with source and drain contacts fabricated on top of an oxidized silicon wafer. A local top gate was patterned on top of the channel, with the doped silicon wafer serving as a global back gate to dope the nanotube *p-type* while the local top-gate doped a short middle portion of channel *n-type*, as shown in Figure 2.6b. Pulsed-laser excitations of the silicon allowed picosecond current pulses to be injected into the nanotube channel, where the delay between the first and a second pulse could be controlled. As expected, precise delay times would produce destructive interference when the arrival of the second current pulse into the *p-n* junction coincided with the arrival of the reflected first current pulse. This

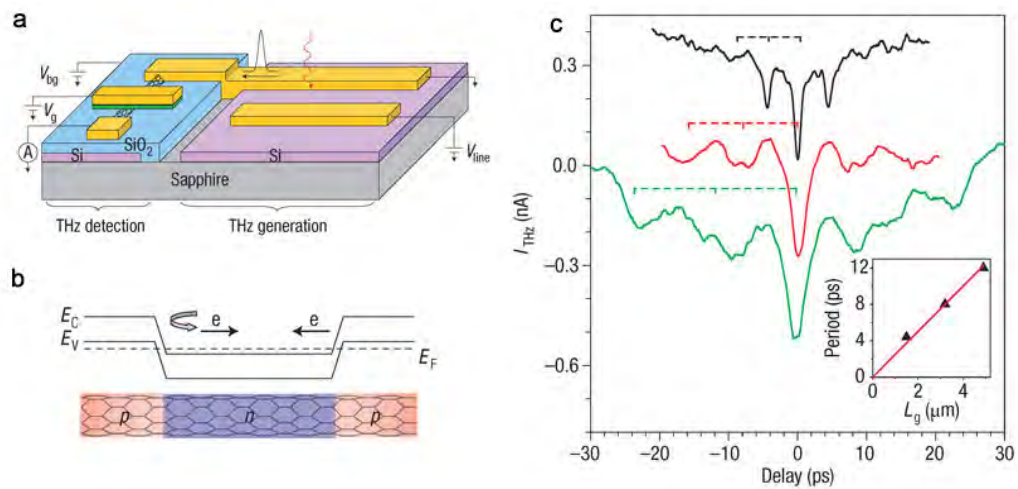


Figure 4.6 – (a) Schematic of time-domain terahertz measurement setup showing an integrated time-domain THz source and single-walled carbon nanotube field-effect transistor. This technique probes the round-trip transit electron ballistic propagation along the nanotube with a picosecond-scale period. (b) Schematic of the electron resonance cavity formed by two p-n junctions created by differential gating along the carbon nanotube. (c) Ballistic electron resonance measured for three devices possessing different gate/cavity lengths. Observe a prominent resonance corresponding to an electron velocity that is constant and equal to the Fermi velocity and not the plasmon velocity. The high-frequency electron response for this system is dominated by single-particle excitations rather than the predicted collective plasmon modes (adapted from Zhong 2008).

combined pulse results in a decrease in the current passing through the channel for pulse-difference times corresponding to time resonances along the channel length as in Figure 2.6c. Unexpectedly, for each of three different channel lengths measured, the delay times produced resonances in the current signal corresponding to the Fermi velocity of 8×10^5 m/s. The predicted resonances resembling charge transport at the faster plasmon velocity were not observed.

In assessing this experiment as an effective means for determining the plasmon propagation velocity, there are several points to consider. The THz generation in this experiment was in the time-domain as a result of a fast laser pulse exciting the doped silicon region between two separated electrodes maintaining a large voltage bias (30–50 V). The laser pulse produces electron/hole separation in the silicon and allows a fast current to flow between the biased electrode gap, yielding a unipolar voltage pulse to traverse down the line with a pulsewidth of ~ 1 ps, equivalent to a broadband THz signal. The 75 MHz repetition rate Ti:sapphire laser used corresponds to a pulse time separation of ~ 10 ns. The pulse width to separation ratio of 1ps/10ns gives a $\overline{10^4}$ duty cycle, so that the DC current is 10^{-4} of the peak current. The stated 4 nA average current then implies peak currents of ~ 40 μ A, which would rapidly saturate the nanotube electron system and heat the electron system, elevating its temperature well above the substrate temperature. If the rectification effect described is due to saturation, the relationship should be sublinear with voltage, not superlinear as claimed. One would also expect the observed THz current peak size to then decrease for longer length samples due to increased scattering, but this is not observed for the two longer samples. For the longest length nanotube investigated, 5 μ m, the two round trips reported corresponds to a full 20 μ m

total travel length. If the electron pulse significantly raises the electron system temperature, the mean-free-path would decrease, as demonstrated by Purewal *et al.* (2007), and the excitations would expect to be attenuated as they traverse the nanotube and one would not expect to observe the stated resonance behavior. Such considerable scattering would also possibly promote mode-mixing, where the faster plasmon mode within the nanotube can intermingle with the three slower neutral modes, possibly only measuring the slowest mode at the Fermi velocity as reported. (More detailed discussions of mode-mixing and paradigms beyond the Luttinger liquid description will be presented in Chapter 6.)

Ngai and Kim have theoretically considered this experiment for directly measuring the velocity by measuring traversal time for an injected electron bunch (Ngai 2011, EA Kim private communication). They conclude that an electron injected will excite all four modes available in a carbon nanotube, so the excitation may be limited by slowest of the four collective modes. They, similar to Burke, present an alternative means to measure the charge velocity by connecting the frequency scale with the finite length of the nanotube via an electric field. Of the four modes within a carbon nanotube, only the plasmon charge mode propagates with a speed not equal to the Fermi velocity. Moreover, this is the only mode that would couple to an applied electric field. Analogous to Burke's transmission line model, Ngai and Kim consider the bosonized form of the low energy effective Hamiltonian of the freely moving right/left charge modes within a finite length metallic carbon nanotube treated as a Luttinger liquid. They find that, as a result of wave interference between the left and right propagating modes, the amplitude of the ac conductance shows pronounced maxima at half-wavelengths on the nanotube. They

additionally consider regimes of weak-backscattering (Ohmic contacts) and strong-backscattering (non-Ohmic contacts). They conclude that, in the weak-backscattering regime, detection of the charge mode velocity through observations of ac conductance peaks should indeed be experimentally possible with a typical micron long metallic carbon nanotube. Our experiment does just this; namely, exciting plasmon mode standing wave resonances in a short high-quality single-walled carbon nanotube using an electric field testing in the frequency domain.

2.5 Summary

Single-walled carbon nanotubes present promising environments for investigating the one-dimensional collective conduction of interacting quantum wires. The varied results coming out of very diverse experiments on the high-frequency properties of individual carbon nanotubes sustains the puzzle of 1D Luttinger liquid behavior physics in carbon nanotubes. Further experimental investigations needed to be realized. By considering the transmission line model of a carbon nanotube, we have presented a direct method for measuring the plasmon propagation velocity and Luttinger parameter for a finite-length single nanotube. We employ observation of THz standing wave resonances. This will provide a signature of the electron-electron interaction within this system. We have discussed the potential issues that prevented such successful measurements in the past and have developed approaches of overcoming or avoiding them in the present work. These solutions require special fabrication and measurement techniques as will be described in the next chapters.

Chapter 3

Device Fabrication

3.1 Fabrication Overview

Over the past half-century, the microelectronics industry has constantly refined the capabilities for the design, fabrication and analysis of continually shrinking electronic devices. An ever-expanding collection of microfabrication and measurement techniques was developed for the assembly and investigation of the properties of microcircuits. The resolution and characterization required by progressively scaling these devices down to the nanometer scale required the related invention of new tools, such as the scanning electron microscope (SEM), utilizing a beam of electrons to produce images; the atomic force microscope (AFM), measuring a local force between a sample and tip; and electron-beam lithography for the creation of microscopic electronic devices.

The present chapter details the central aspects and challenges of carbon nanotube device fabrication which take advantage of this expertise. The growth of carbon nanotubes atop a silicon substrate is the result of a chemical processes. The imaging of carbon nanotubes demands the use of extremely high-resolution instruments due to their extremely small diameters. As explained in Chapter 1, in order to investigate the

electronic nature of individual carbon nanotubes we employ a field-effect transistor geometry, where the nanotube is contacted on each end by a metal electrode, commonly known as the *source* and *drain* contacts, and a third electrode capacitively coupled to the nanotube, referred to as the *gate* electrode. Figure 1.4 showed a schematic of the different device configurations employing a *back-gate* (or *bottom-gate*), where the gate electrode is globally (or locally) underneath the nanotube, separated by a dielectric material, or placed as a *side-gate*, where the gate is on the same plane as the nanotube. For our proposed terahertz (THz) measurements, the source and drain electrodes also form an antenna geometry for coupling of free-space signals to the nanotube located at its center. As nanotubes can occur in both single-walled or multi-walled forms and can possess a variety of electronic properties, each device must be screened to determine if it is a contender for the subsequent fabrication step. A given nanotube experiences a long journey from initial growth to ultimately being chosen for possible THz analysis.

3.2 Carbon Nanotube Device Fabrication

We begin with an overview outlining the simplest series of principal steps involved in the fabrication procedure of an antenna-coupled carbon nanotube device for THz measurements, and then we will proceed to explore the key stages in more specific detail. [Steps listed in square brackets are optional depending on the final device desired.]

1. Begin with a high-resistivity silicon wafer substrate
2. [Lithographically pattern and deposit metal to form bottom-gate]
3. Grow thermal oxide of desired thickness, if oxide is not already present

4. Define alignment marks using lithographic process and etch into oxide and silicon
5. Lithography pattern fiducial marking array of HSQ e-beam resist
6. Grow carbon nanotubes from selected catalyst using chemical vapor deposition (CVD) process at high-temperature in furnace
7. [Lithograph fiducial marks followed by metal evaporation (Ta) if not done prior to growth]
8. Use SEM to image chip to determine nanotube location relative to fiducial marks
9. Use AFM to measure heights of isolated individual nanotubes
10. Lithographically pattern *source/drain/gate* electrodes in antenna/gate geometry to contact desired nanotubes, followed by metal evaporation (Pd) and lift-off in warm acetone
11. Image nanotube devices using SEM and AFM
12. Remove unwanted nanotubes by oxygen plasma etching in lithographically defined areas
13. Electrically probe nanotube devices at room temperature and ambient conditions
14. Select metallic single-walled nanotubes to mount and wire-bond in chip carrier for dc testing at low temperature ($T = 4$ K)
15. Select low-resistance nanotube devices for integration with alignment wafer piece and silicon lens backing
16. Wire-bond quasi-optical nanotube/lens device system to antenna carrier and mount in optical access cryostat in interferometer setup

Countless variations exist for nearly all of the processing steps listed and a wide variety of tools are frequently available to choose from for accomplishing a particular

objective. As will be explained, the specific choice for each stage of the fabrication process is motivated by the ultimate device desired and its specific requirements.

3.3 Silicon Substrate

Often for nanotube electronics research, a degenerately-doped silicon substrate with a silicon dioxide layer is utilized in order to easily obtain the field-effect geometry for typical nanotube devices. The substrate can then be contacted electrically, even at cryogenic temperatures, and operated as an efficient back-gate with the silicon dioxide layer acting as the insulating layer between the gate and the device. Such silicon wafers are readily available commercially and can be purchased with an oxide of specified thickness. However, the oxide quality can vary greatly, where a poor thermal oxide easily breaks down at high applied gate voltages or during the wire-bonding process. This produces ohmic conduction across the dielectric between the device and doped substrate, a behavior known as gate leakage, and the gate will no longer perform as designed to alter the electrical properties of the device. In addition to acting as the dielectric for possible gating, the presence of a silicon dioxide layer provides excellent contrast for SEM imaging of carbon nanotubes.

A more serious issue with the use of doped substrates in this work is that the free charge carriers of the donors in the doped silicon (resistivity $\sim 1 \text{ m}\Omega\cdot\text{cm}$ at room temperature) result in significant absorptive losses of THz radiation; thus, they are incompatible with our quasi-optical THz coupling scheme described below, where THz radiation is to be transmitted through the substrate. Lightly-doped silicon ($\sim 1 \text{ }\Omega\cdot\text{cm}$) was

investigated and shown to allow for sufficient THz transmission as well as gating, but also demonstrates substrate heating. High resistivity silicon ($>1 \text{ k}\Omega\cdot\text{cm}$) acts as a lossless medium for THz, with a lack of dopants preventing absorptive losses. In addition, the large direct band gap of silicon prevents THz photons from being absorbed across the bandgap. However, the use of this high-resistivity silicon prevents back-gating using the substrate and requires alternate approaches. We can use a side-gate geometry, where the gate is nearby in the same plane as the device, or instead deposit a bottom-gate of a thin section of metal on only a limited portion of the wafer to be located underneath (or a top-gate above) the device, separated by a deposited dielectric. We use the Yale University cleanroom Oxford Plasmalab80 for plasma enhanced chemical vapor deposition of a silicon dioxide film as the dielectric on regular high-resistivity silicon substrates or those possessing the thin bottom-gate metal electrode.

3.4 Alignment Marks

Global alignment marks are used as locators for the orientation of a silicon wafer section and for automatic alignment of lithography steps. These must possess sufficient topographic contrast for the electron-beam writer to reliably recognize them for subsequent lithography steps using its automatic alignment algorithm. Etching shapes deep enough into the silicon dioxide and silicon wafer or depositing metals with large atomic number are commonly used for this purpose. We etch approximately $1.5 \text{ }\mu\text{m}$ deep into the silicon substrate using a combination of SF_6/CF_4 and CHF_3 gases in the Yale Cleanroom Oxford Plasmalab80 to reactively ion etch through a lithographically exposed

e-beam mask resist. Previously, when using a FEI Sirion XL40 converted electron beam writer with J.C. Naby Nano Pattern Generation System, we would manually align to deposited metal tantalum global alignment marks, but this was not nearly as accurate. These initial metal alignment marks were often in the shape of a cross measuring $10\ \mu\text{m} \times 10\ \mu\text{m}$. For our later work, the etched markers in the shape of a $4\ \mu\text{m} \times 4\ \mu\text{m}$ square, surrounded by $60\ \mu\text{m}$ long and $1\ \mu\text{m}$ wide bars acting as optical markers, are located at the periphery of the wafer and in the four corners defining each $3\ \text{cm} \times 3\ \text{cm}$ chip subsection. In addition, for device labeling and general organization, we would simultaneously etch wafer subsection names, detailing the wafer name and subsection grid location, during the same lithographic and etching process. Furthermore, the trenches used for studies focusing on suspended nanotubes, where the nanotube extends over a trench with no oxide or silicon directly below, can also be lithographically defined and etched during these same steps.

A key difference between the use of metal versus etched alignment marks depends on the stage at which either can be accomplished relative to carbon nanotube synthesis. Any processing or alignment marks must be able to survive the high-temperatures necessary for nanotube growth, as explained below, and also not interfere with the growth conditions. Etching into the silicon will not have any detrimental effects, so that is done prior to growth. However, the presence of many metals, including tantalum, during the growth conditions can yield undesirable nanotubes or amorphous carbon structures. Thus, the tantalum deposition would instead be performed following nanotube growth.

3.5 Carbon Nanotube Synthesis

An extensive amount of research has focused on the various synthesis approaches and the broad range of conditions which can produce carbon nanotubes. The first large quantities of nanotubes were formed in the 1990s using the arc discharge or laser ablation methods (Wong 2011). These techniques do not result in the clean and isolated single-walled nanotubes preferred for electrical study or applications, but rather produce nanotubes that are multi-walled or grouped together as bundles, in addition to generating many unwanted amorphous carbon byproducts and other contaminants. To remove the undesirable carbon material, cleaning and purification processes involving harsh acidic solutions can be used, but these often also destroy the sought after carbon nanotubes. The limited surviving nanotubes can then be dispersed in a liquid solution, sonicated in order to slightly break apart the bundles of tubes, and then spun onto a silicon chip for subsequent processing. However, this vital sonication step also frequently leads to a limit in nanotube size where the bundles initially measuring hundreds of microns in length are reduced to smaller bundles or individual nanotubes that are often well under ten microns in length and may be far from pristine. Such length scales are sufficient for some electrical studies, but not ideal. Thus, searches for new synthesis techniques resulting in fewer contaminants, less amorphous carbon formations and yielding nanotubes much longer in length were sought. By the late 1990s, chemical vapor deposition emerged as the preferred synthesis method for carbon nanotubes (Kong 1998).

Chemical vapor deposition (CVD) has existed for decades as a technique to create thin films in the semiconductor industry. Hongjie Dai's research group at Stanford University pioneered and advanced the use of CVD for the production of mostly defect-free and isolated on-chip single-walled carbon nanotubes (Kong 1998). This process involves the thermal decomposition of a hydrocarbon vapor in the presence of a metallic catalyst particles, often nanoparticles or nanoclusters, on a flat sample silicon/silicon dioxide surface, often with a uniform thickness of around 300 to 500 microns of silicon and 200 to 300 nanometers of silicon dioxide, at high temperatures. The catalyst particles decompose the carbon-containing gas and nanotubes then grow. A vast collection of nanotube growth recipes has been developed in the literature, specifying the variations of the catalyst material, exact specifications of gas flow and temperature, and other additional ingredients. These parameters will even gradually change over time within the same growth setup due to unknown or unavoidable causes. CVD has become a simple, economic and versatile technique for synthesizing high yields of pure carbon nanotubes for experimentalists. Using trial and error, with an educated basis and much fine-tuning, one can determine optimal parameters to develop a successful nanotube growth recipe. However, a recipe that yields success in one research lab does not ensure a separate lab will be able to reproduce those same results. In the course of this thesis work the actual nanotube growth was performed in the facilities of Prof. Philip Kim at Columbia University, and then subsequent processing was done at Yale University. Several different nanotube batches were grown in furnaces, with various catalyst materials, gases and distinct growth recipes, yielding a wide range of nanotube growth results.

3.5.1 Carbon Nanotube Synthesis Parameters

The exact nature of the carbon nanotube growth mechanism from catalyst particles has long been debated. Several proposals have been made for the microscopic process and reported experiments often contradict one another. However, it is fairly well agreed that when the hydrocarbon vapor interacts with the liquefied metal catalyst nanoparticle, due to the high temperature, the gas decomposes into carbon and hydrogen atoms, where the carbon atoms are dissolved into the nanoparticle and hydrogen forms a gas that flows away (Kumar 2010), as shown in Figure 3.1. Once the metal saturates at its carbon-solubility limit, the carbon begins to precipitate out and form an energetically favorable crystalline cylindrical network. For cases where the catalyst-substrate interaction is weak, the carbon precipitates out at the bottom of the metal and pushes the nanoparticle up off of the substrate as the nanotube forms and grows in length. This process, where the catalyst particle floats off the substrate, is known as the “tip-growth” model. If, however, the catalyst is well anchored on the substrate surface, the carbon precipitates out at the top of the nanoparticle, first forming a rounded carbon cap and then continuing growth of the cylindrical nanotube. This is referred to as the “base-growth” model. Imaging of nanotubes grown using different metal catalysts under similar growth conditions have exhibited evidence of both growth models in regard to final position of catalyst particles. Both processes continue as long as there is metal exposed for fresh hydrocarbon decomposition, but once the catalyst is fully covered with excess carbon, the catalytic activity stops and nanotube growth ceases. In contrast to the arc discharge and laser ablation synthesis methods with fairly narrow diameter ranges, CVD growth results in a wide range of single-walled nanotube diameters ranging from ~0.7 to up to 3 nm. The

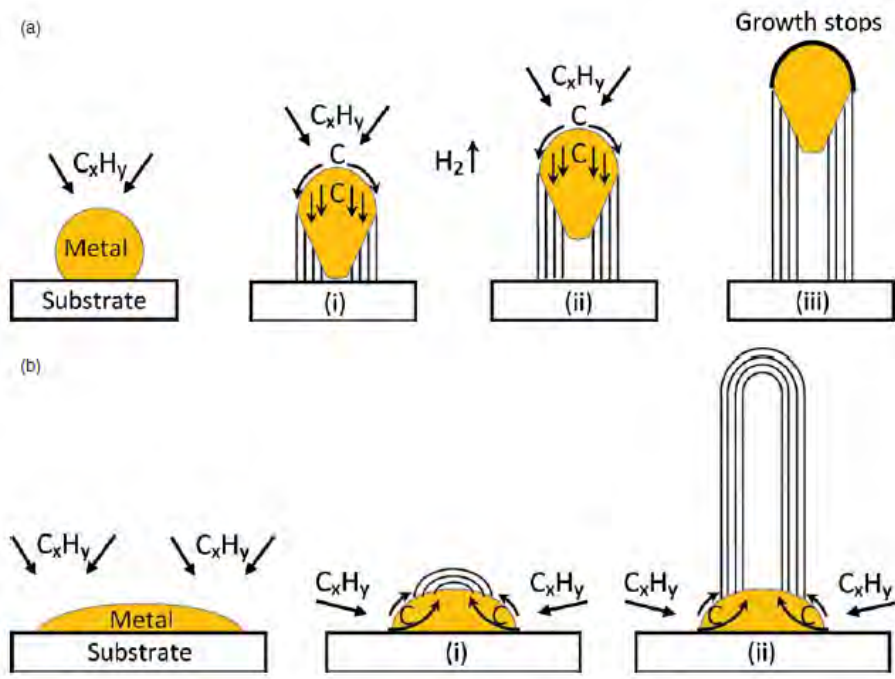


Figure 3.1 – Illustration of the carbon nanotube growth mechanism via chemical vapor deposition for (a) tip-growth and (b) base-growth. Hydrocarbon vapor interacts with liquefied metal catalyst nanoparticle at high temperature. Carbon atoms dissolve into the nanoparticle and hydrogen gas flows away. Carbon precipitates out the catalyst once the metal saturates, forming a multi-walled carbon nanotube (Kumar 2010).

size of the catalyst particle is thought to dictate the nanotube diameter and govern the formation of single-walled or multi-walled nanotubes. Smaller nanoparticles measuring a few nanometers in diameter favor single-walled nanotube growth, while larger nanoparticles promote multi-walled nanotube growth. The choice of catalyst metal and substrate material, as well as catalyst preparation will greatly determine its size based on factors including growth temperature, oxidation time, catalyst dispersal method, as well as any templating or support structure for the catalyst. The catalyst nanoparticles are formed from an individual metal or combination of several metals, possessing a high melting point along with good carbon diffusion rates and solubility, which includes iron, nickel, molybdenum, and cobalt. They can be suspended in a solution or implanted in a template structure. There are different methods for depositing the catalyst particles onto the substrate surface. The catalyst-substrate interaction can lead to different size catalyst particles during growth due to diffusion and migration of the catalyst particles on the surface at the high temperatures. These different properties can result in larger catalyst particles as the nanoparticles aggregate on the surface.

Furthermore, the other synthesis parameters, such as hydrocarbon feedstock, deposition and growth times, growth chamber pressure, gas-flow rates, ratio of gases, and reactor geometry also play key roles in determining success of nanotube growth. Small changes can dramatically alter the outcome, frequently in a negative way. Some adjustments, however, are advantageous. For example, adding hydrogen flow in the chamber along with the carbon feedstock can convert some gas byproducts, such as carbon monoxide, into water which will prevent the accumulation of amorphous carbon on the nanotubes (Hata 2004).

Initially, the Dai group produced robust nanotube growth with low defect density and extremely long lengths, over 100 microns, on silicon and silicon dioxide substrate using methane as the carbon source (Kong 1998). Later the Liu research group used carbon monoxide as their carbon source and a “fast heating” process where the catalyst on a silicon substrate is inside the quartz gas flow tube, but external to the oven, until the desired growth temperature is achieved (Huang 2004). Then, once the oven is at desired temperature, the quartz tube and substrate with the catalyst are quickly moved into the hot zone center of the oven. This procedure prevents the catalyst nanoparticles from aggregating due to thermal migration over an extended period of time under extreme heat. Also, this creates turbulence of the relatively hotter gas flow above the cooler substrate, keeping the catalyst particle floating during a tip-growth and preventing growth termination from nanotubes colliding with neighboring nanotubes. In this way, nanotubes with lengths over a centimeter have been achieved, with an extreme aspect ratio of about ten million to one. The stability of a laminar gas flow is crucial to the growth of such ultra-long nanotubes which are aligned in the direction of the smooth gas flow and can yield numerous nearly parallel ultra-long nanotubes. Such nanotubes are advantageous for electrical measurements and applications since they can be spread out enough on the chip to easily pattern electrical devices out of a single or several nanotubes for further study. We initially achieved this with a tube-within-tube growth reactor geometry as developed by our collaborators at Columbia (Hong 2005). More recently, ethanol vapor has become a popular carbon source (Maruyama 2002, Huang 2004) allowing for a slightly lower growth temperature around 850 °C producing less amorphous carbon and not posing any of the potential health dangers associated with using carbon monoxide.

Several other carbon sources have proven effective for growing nanotube forests for interesting new applications, such as weaving large quantities of nanotubes into yarn (Nakayama 2008).

We grow nanotubes in a one-inch quartz tube at Columbia University using the growth facilities of the Kim and Hone groups by operating a furnace with central hot zone of about 18 inches on a rail system for fast heating and methane or ethanol as the preferred carbon feedstock. The one-inch diameter quartz tube limits the size of our silicon chips; prior to this, when using a tube within tube geometry to obtain laminar gas flow, the inner tube diameter limited chip widths to be below 1 centimeter. The specific equipment and recipes used varied over several years and we next briefly describe the primary growth recipes used for the devices studied in this thesis.

3.5.2 Methane Growth

For our work the nanotubes were initially grown from a catalyst of iron-trichloride (FeCl_3) nanoparticles, approximately two nanometers in diameter, suspended in hexane. A sharpened toothpick was dipped into this solution and quickly swiped along an edge on the top surface of the silicon substrate. In this way, the catalyst spreads out in a narrow line on the top of the chip as the hexane evaporates shortly thereafter. Other groups sometimes use lithography to predefine catalyst islands as small squares at known positions on the chip. To improve laminar flow inside the growth tube, we initially place a smaller diameter quartz tube inside the normal one inch quartz tube and place chips inside (Hong 2005). This narrower tube with samples inside is carefully loaded into the

quartz tube at the center of the furnace and heated to 950°C in an argon flow rate of 500 sccm to purge the system of oxygen. Once the desired temperature is reached, the flow rate of argon is reduced to 200 sccm and a hydrogen flow at 60 sccm is begun for approximately 30 minutes. Then, the argon is stopped and a methane flow at 100 sccm is initiated for 2 hours. The small coflow of hydrogen allows unwanted byproducts to form water and be removed during growth, preventing the accumulation of amorphous carbon and averting the catalyst particles from poisoning too quickly and ending growth. The nanotube growth occurs during the methane flow and results in ultralong nanotubes. Following this growth time, the quartz tube is flushed with an argon flow at 500 sccm at the growth temperature for 10 minutes. Afterwards, the heating element is turned off and the sample is allowed to cool to room temperature in a sustained argon flow before removal from the furnace.

This methane growth process has been shown to produce many long nanotubes as shown in Figure 3.2. However, subsequent Rayleigh scattering studies reveal that the majority of the nanotubes grown are actually multi-walled nanotubes or small bundles of single-walled nanotubes and are also coated with large amounts of amorphous carbon (Caldwell 2011). Rayleigh scattering is a noninvasive technique that shines bright white light generated by fast laser pulses on a nanotube and analyze the resulting spectrum. This provides fast mapping of key nanotube parameters, including number of walls as well as the chiral indices and electronic type (Sfeir 2004). Thus, alternative and superior growth methods for producing a higher proportion of clean single-walled nanotubes have been pursued.

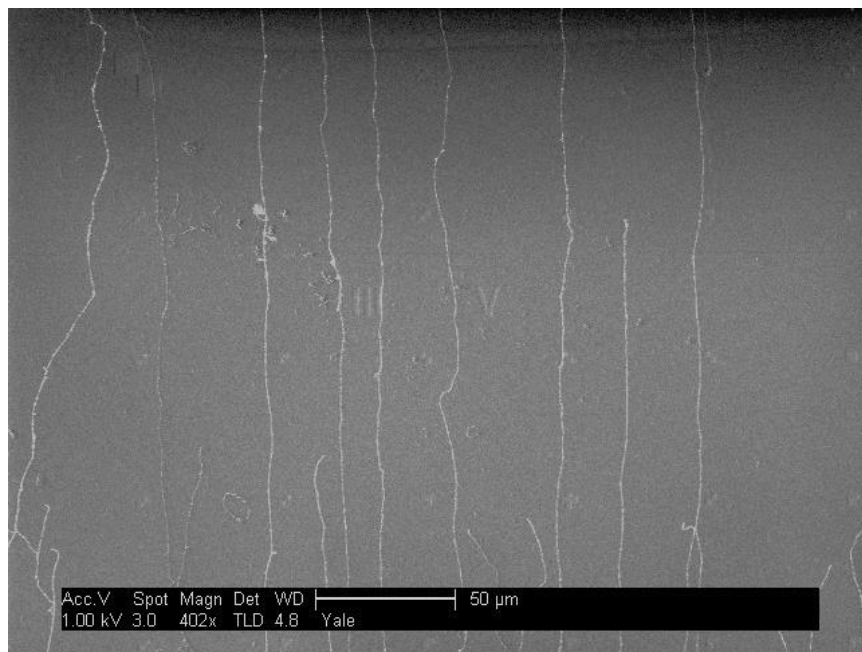
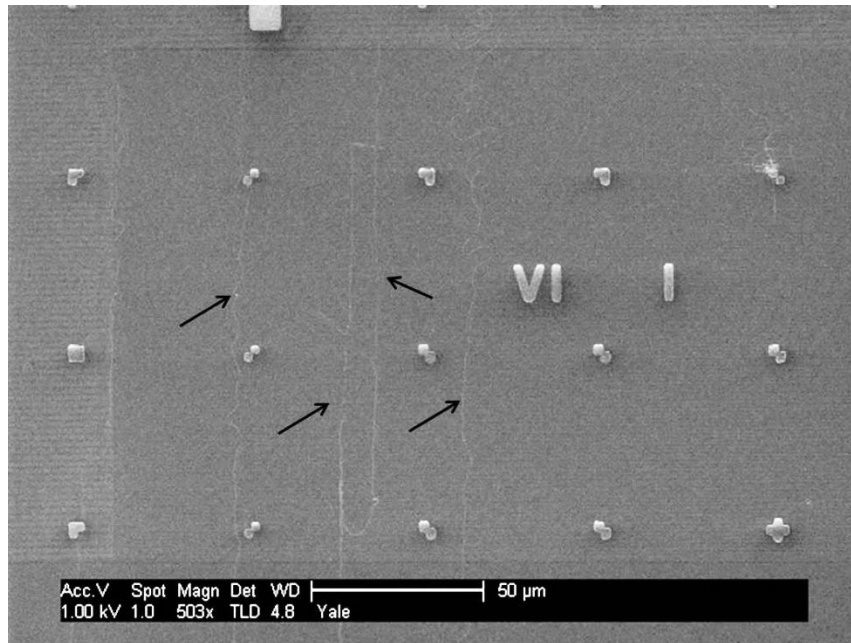


Figure 3.2 – SEM micrographs of carbon nanotubes produced by methane growth with FeCl_3 catalyst particles and Ta fiducial markers. The use of methane and FeCl_3 can produce ultralong carbon nanotubes, but a large percentage are multi-walled. The conditions for the top micrograph, low accelerating voltage and small spot size, allow for easy recognition of the fiducial markers, but make the surface potential difference or electron-beam-induced current representing long, parallel carbon nanotubes more difficult to identify (indicated by arrows). The lower micrograph, at the same voltage but larger spot size, shows many bright lines signifying numerous long, parallel carbon nanotubes, but the fiducial markers are much harder to distinguish under these conditions.

3.5.3 Ethanol Growth

As mentioned earlier, ethanol vapor has emerged as a popular carbon source producing long, individual single-walled nanotubes not bundled and mainly free of amorphous carbon deposition. The catalysts and recipe procedure used as a part of the ethanol growth synthesis also were developed and optimized by Chenguang Lu and others at Columbia University to yield clean single-walled nanotubes (Huang 2004). The catalysts used are cobalt-molybdenum salts or an iron-molybdenum nanocluster, known as a Muller catalyst (Muller 2000), within a silica or alumina template support structure. The advantages of these hybrid nanoclusters is that they are designed to be easily dispersed in ethanol and do not clump to one another when dispersed on a silicon chip; the template structure is a porous material with a high surface area to increase growth yield, can withstand high temperatures and presents nanometer sized channels in which the nanoclusters form, limiting their size (Zoican 2010). This catalyst evolution had the objective of reducing the catalyst dimensions, and thus nanotube diameter and proportion of single-walled and multi-walled nanotubes. These characteristics do indeed lead to the growth of predominantly clean several hundred micron long single-walled nanotubes, though this is not quite as long as previous methods, with a narrower distribution of diameters. An additional step introduced to prevent the introduction of amorphous carbon is a quartz tube cleaning step in between growths where any remaining carbon in the tube from a previous growth is burned out in a pure oxygen flow at $\sim 1000^{\circ}\text{C}$ to remove any residual organic material from the tube. Similar to the previous method, a toothpick is used to disperse sonicated catalyst particles onto the silicon chip and placed in the furnace quartz tube. The temperature is ramped to 400°C in air for 30 minutes to burn

away any remaining organic material. After cooling to 200°C, the system is purged with argon to remove oxygen from the growth chamber. A flow of ethanol and hydrogen is introduced so that growth can proceed using the fast heating method. The temperature is set to 1000°C with the oven positioned away from the sample so the chip is out of the oven hot zone; once the 1000°C setpoint is reached, the oven is moved so that the sample is at the oven center and the temperature is now set to 900°C. The thermocouple temperature reading will dip to ~800°C before increasing again. The ethanol flow is stopped 10 minutes after the minimum temperature reading. The heating is stopped and the oven is then allowed to cool with the sample in a pure hydrogen environment to prevent accumulation of amorphous carbon. SEM images of carbon nanotubes produced with ethanol growth are shown in Figure 3.3.

3.5.4 Chirality Selection

For the use of nanotubes in reproducible real-world electronic applications, the growth of nanotubes possessing identical chiralities is necessary. With nanotubes functioning as interconnects in electronic circuits, each nanotube must be known to be metallic.

Similarly, for the use of semiconducting nanotubes as transistors, identical chiralities are necessary to ensure a common threshold voltage with sharp on/off ratios. Extensive research has been focused on finding synthesis techniques able to grow specific types of chiralities of clean nanotubes with different inherent properties, in specific locations isolated from one another, for the easy production of electrical devices. So far, this has not been fully achieved, but many groups have sought ways to separate and sort

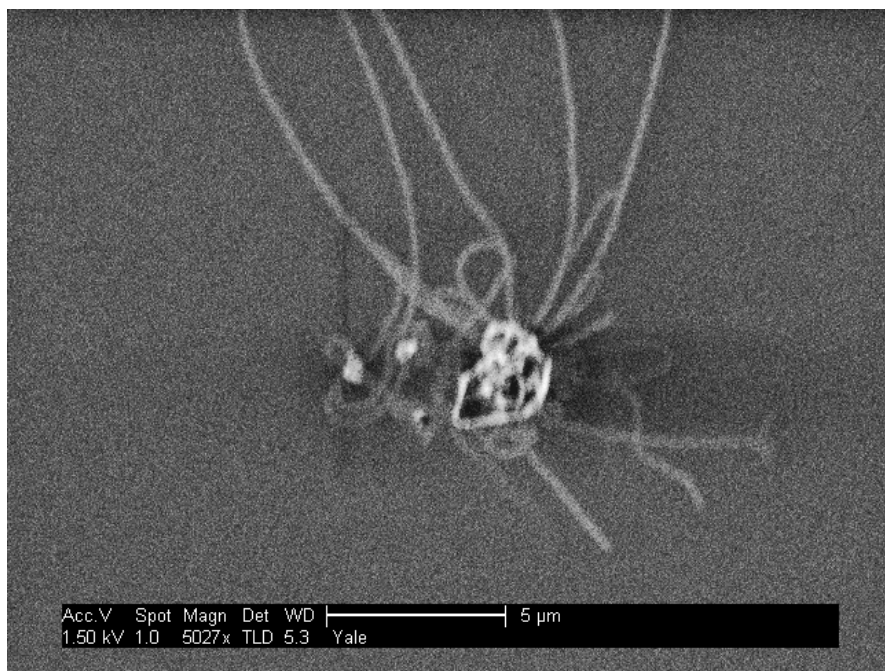
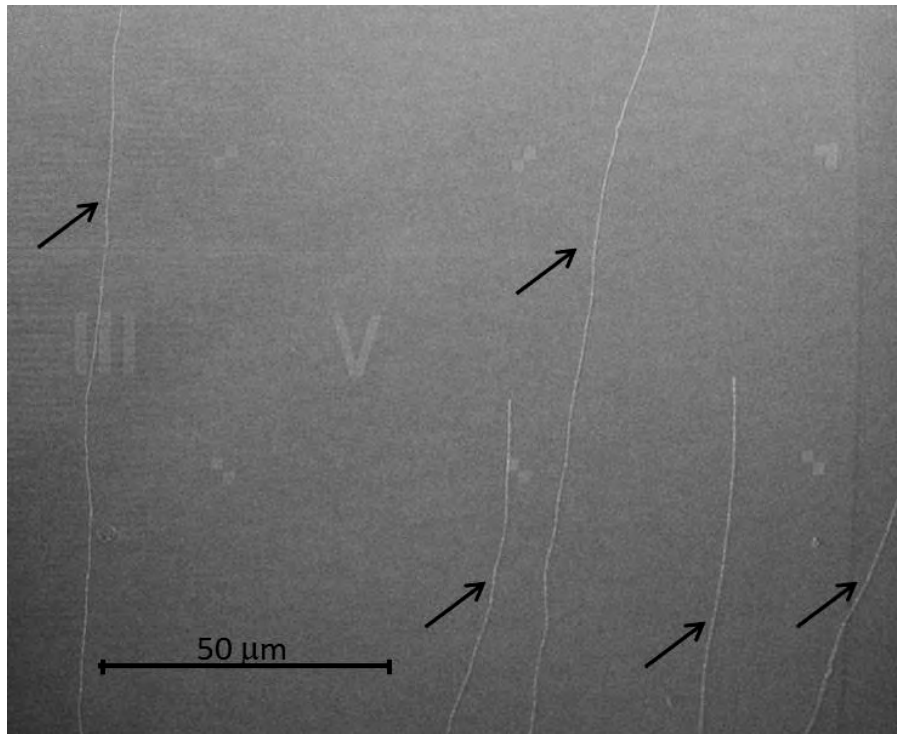


Figure 3.3 – SEM micrographs of carbon nanotubes produced by chemical vapor deposition growth from template Muller catalysts using ethanol as the carbon source and the fast heating method. These catalysts and growth conditions promote a higher proportion of ultralong single-walled carbon nanotubes. The bottom micrograph shows the numerous nanotubes growing out of catalyst clump.

nanotubes after growth by chirality (Vijayaraghavan 2012). There was no chirality selectivity involved in the growth and fabrication of devices discussed in this work; it is only after electrical contacts are deposited that transport measurements allow for the differentiation between metallic and semiconducting nanotubes. Much remains to be understood regarding the chemical growth process of carbon nanotubes and there is still considerable progress yet to be made before their inclusion in practical electronic device applications.

3.6 SEM Imaging

Scanning probe microscopy, such as atomic force microscopy (AFM) and scanning tunneling microscopy, are valuable methods initially used for determining the diameter and location of nanotubes as well as characterizing their electrical and mechanical properties. An AFM used in electrostatic force microscopy (EFM) mode, where a voltage is applied to the cantilever tip and electrostatic force gradients are measured, can produce a phase shift of the cantilever oscillation in the presence of the nanotube due to a strong charge interaction between tip and tube, which can be more readily detected than by using only AFM height imaging. However, such AFM techniques offer limited scan areas and are frequently time-consuming, making them impractical for the analysis of wide regions or large structures. Field Emission Scanning Electron Microscopy (SEM) is a well-established technique with widespread application in many areas of research and development and has more recently proven to be a very powerful tool in studying nanotubes on insulating substrates. Nanotubes with diameters typically in the range of 1-

4 nm have been shown to exhibit remarkable SEM contrast on Si/SiO₂ substrates (Brintlinger 2002), providing an easy and efficient process for identifying the location and measuring the length of nanotubes. This approach also provides quick feedback for growth processing and evaluating nanotube growth density. Both metallic and semiconducting nanotubes can be detected in this manner, but not easily distinguished.

Due to their small diameter and low material volume, the direct electron beam interaction with a nanotube is negligibly small, causing the SEM image contrast of a nanotube sample to be very sensitive to the specific imaging conditions as well as nanotube and substrate properties. These imaging parameters can include the accelerating voltage (primary beam energy), scanning speed (dwell time), detector choice, and magnification. The length of a nanotube, its electrical characteristics, and its connection to an electron source, including other nanotubes or to a metallic electrode, affect the electron diffusion within the nanotube and the SEM image contrast. It has been widely reported and confirmed in this work that SEM imaging at low primary beam energies (<2 keV) and low magnification allows for easy detection of bright contrast images showing individual single-walled carbon nanotubes on insulating surfaces, this despite the fact that the nanotube diameters are much smaller than the SEM resolution. Typically, SEM images are acquired through the detection of secondary electrons generated from a sample by a primary electron beam. The image is sensitive to the sample surface potential which is also known as voltage contrast. This technique is insensitive to surface roughness, defects, or many forms of contamination. Since the secondary-electrons generated by scattering from a small-diameter carbon nanotube are insufficient for imaging, a variety of novel mechanisms for this phenomenon have been proposed for the

rapid SEM imaging of carbon nanotubes on insulating substrates, with the common conception that it is due to charging characteristics between the nanotube and insulating substrate.

Brintlinger *at al.* first suggested that this was due to a voltage contrast mechanism from the differential charging of the conducting nanotube relative to the insulating background substrate, typically SiO₂ (Brintlinger 2002). The electron beam irradiation creates a local surface potential difference in the conducting nanotube relative to the insulating oxide, resulting in the observed image contrast. The much greater apparent diameter of 50-100 nm observed using SEM by the detected secondary electrons, when compared to 1-2 nm true physical diameter confirmed by AFM height profile measurements, is a result of the long-range electric field around the nanotube. As the electron beam scans, the thick insulating oxide becomes charged by electrons from the beam which cannot move. However, the conducting nanotube is less charged since the electrons are able to flow along its length. Thus a potential difference between the oxide surface and the nanotube will result. For the case where the potential difference between the nanotube and detector is greater than that of the substrate and detector, the nanotube appears brighter with respect to the substrate. The positively charged substrate appears dark, the nanotube and the surrounding region is bright compared to the rest of the surface, broadening the apparent diameter of the nanotube to a much larger size on the order of tens of nanometers. Changes in the scanning parameters, such as decreased scan speed, increased magnification or increased beam current, as well as different geometries or electrical conductivity of the nanotube, can allow for the nanotube to more readily reach a potential equilibrium with the substrate which will degrade image contrast. For

higher accelerating voltages, the electron beam penetrates further into the oxide, yielding fewer secondary electrons near the surface and thus decreasing the sensitivity to the surface potential difference. Image contrast is thus best for low accelerating voltages of 1-2 keV and drops dramatically at >3 keV. This is due to the fact that the surface potential is on the order of several volts. The insulator surface is positively charged when electron beam energy is <3 keV, but negatively charged when >3 keV as well as the deeper penetration of the electron beam. The positive surface potential will only exist in regions irradiated by the electron beam. It is important to note that the contrast difference is a relative observation and that the nanotube and oxide must be in close contact to generate a sufficient potential distribution. Also, as is well known, previously irradiated areas appear as dark rectangles in subsequent SEM images due to this surface potential contrast, burned on carbon or other contamination. If a nanotube is electrically connected to a metal pad or an area beyond the scanned region, the metal electrode or non-irradiated area can act as an electron supply reservoir, thereby allowing the conductive nanotube to become more negatively charged and thus appear brighter and thicker than an isolated nanotube. Even long unconnected nanotubes can exhibit such enhanced voltage contrast since, depending on primary electron beam energy and scan direction, the nanotube may be charged by the beam on one end and then appear charged for the remainder of the image.

Homma *et al.* proposed an alternate mechanism for low primary-electron voltage imaging using an SEM of a nanotube on an insulating substrate surface (Homma 2004). By using the in-column type secondary-electron detector, which detects low-energy electrons, the insulator surface surrounding the nanotube is imaged rather than the

nanotube itself. This method results in bright, highly selective imaging of individual nanotubes. The primary electron beam irradiates the oxide, producing electron-hole pairs, which increases the electrical conductivity in the irradiated area and also causes significant secondary-electron emission from the insulating oxide surface, so electrons near the oxide surface are depleted. A current is induced if electrons are supplied to the oxide, by the nanotube acting as a conducting wire, allowing it to return to its original secondary-electron value. The image contrast reflects this electron-beam-induced current (EBIC) around the nanotube where an oxide surface contacting a nanotube appears brighter by emitting more secondary electrons than the average surface. Thus, the nanotube appears wider than its actual diameter, resulting as the sum of the electron scattering range and the electron diffusion length in the oxide. The in-column detector is optimized for low-energy secondary electron detection providing the best image of the bright lines which are not the direct image of a nanotube, but are rather images of the oxide surface current near the nanotube.

These theories for nanotube imaging become further complicated due to the fact that successful SEM imaging of nanotubes that are not in contact with a substrate is also possible. Homma *et al.* later extended this picture by examining suspended nanotubes, which do not possess the same conducting path to the substrate as nanotubes in direct contact with the oxide surface (Homma 2005). Low primary electron-beam voltages <2 keV are found to still yield the best image contrast. This is possibly explained by the primary beam electrons directly interacting with the nanotubes singular surface layer (the beam interacts with the nanotube tubular structure top and bottom sections) generating high-energy secondary electrons which inelastically lose their energy through multiple

collisions inside the nanotube surface before low energy secondary electrons escape to the detector. Distinct contrast models to explain this have been proposed by Finnie *et al.* which describe the charged suspended nanotube deflecting the emitted secondary electrons or, alternatively, the charge suspended nanotube produces a locally varying secondary electron yield (Finnie 2008). Additionally, the supports propping up the nanotube allow charges to flow along the length of the nanotube and give rise to electrostatic interactions between the nanotube and substrate. The nanotube is then at a lower potential than the substrate and a dielectric substrate will be polarized by the electron beam, allowing any positive charges in the substrate to be drawn towards the surface and thus the nanotube. This provides a contrast imaging mechanism due to different charge distribution, and a dark contrast due to excess positive charge.

In addition, the SEM image contrast can be related to the electrical properties of the carbon nanotube. Metallic and semiconducting single-walled carbon nanotubes on a silicon dioxide substrate may have noticeably different contrasts under SEM due to their conductivity difference. Thus, they can be distinguished and effectively identified where some nanotubes are bright while others seem dark. Ji *et al.* examined contrast comparison due to the electron beam inducing a surface potential in the insulating silicon dioxide. They found that the conductivity difference between metallic and semiconducting nanotubes can be identified and concluded that bright ones are metallic and dark ones are semiconducting (Li 2012). Notwithstanding the various explanations for and capabilities of imaging carbon nanotubes with SEM, this technique is an immeasurably valuable tool for locating and fabricating nanotube devices for electrical measurements.

3.6.1 SEM Contamination

Despite the many advantages of imaging carbon nanotubes with SEM, especially when compared to AFM, there are still some drawbacks. One universal problem is that there is a carbon contamination which accumulates on the image surface as the electron beam scans. Moreover, exposure to the electron beam is known to cause significant irradiation damage to the carbon nanotube electronic behavior, characterized by a decrease in conductance (Suzuki 2004). We and other groups find it optimal to image the nanotubes at both low magnification and low electron beam dose to reduce this damage. One possible origin of this damage is that the high-energy incident electrons from the primary beam can ballistically eject carbon atoms from the nanotube, known as knock-on damage. However, this knock-on damage should occur above a threshold in the operating range of high-energy transmission electron microscopes (TEM) which operate with beams >100 keV when one considers the very strong bonding of the carbon atoms in the seamless graphene sheet cylinder that forms the carbon nanotube. Instead, SEMs typically operate from 1-30 keV and must cause damage via other mechanisms. One mechanism is that contaminants, such as adsorbed oxygen, are able to adhere via van der Waals attraction to the nanotube due to the SEM beam irradiation (Suzuki 2004). Another possibility is that the electron beam produces trapped charges when penetrating into the oxide in proximity to the nanotube. This local charge distribution of the adsorbed contaminants or the trapped charges in the oxide affects the nanotube electronic properties by producing an electric field which induces a band gap in the local nanotube density of states. This contamination is unavoidable and presents itself with any

technique utilizing an electron beam, including electron beam lithography which is almost universally used to define contacts to nanotubes. Thus, due to the processing of nanotube devices with these trapped charges and adsorbents, the nanotubes often exhibit less than ideal performance.

The SEM imaging for this work primarily used an FEI Sirion XL40 SEM with a thermal field emission source possessing both standard secondary electron (SE) as well as a through-lens detectors (TLD). The TLD detector, located in the column of the SEM, senses backscattered electrons and is extremely sensitive to sample surface potential. The TLD detector is thus a good choice for imaging of carbon nanotube devices at low accelerating voltages. In addition to the primary beam voltage, the selected beam size determines the spatial resolution, greatly affecting the image contrast and quality for detecting carbon nanotubes. However, unlike more typical imaging where smaller spot sizes yield greater resolution, larger spot sizes were found to give better contrast for carbon nanotubes, supporting the theory that carbon nanotube imaging is due to the nanotube and substrate relationship and not the nanotube alone. Figure 3.4 shows several SEM micrographs of the same catalyst region under different operating voltages and using different detectors, demonstrating the benefits of lower beam voltage, larger spot size, and the enhancement from use of the TLD detector.

3.7 Fiducial Mark Array

Individual carbon nanotubes grown from a catalyst stripe using CVD are randomly positioned and oriented on the silicon substrate. In order to fabricate carbon nanotube

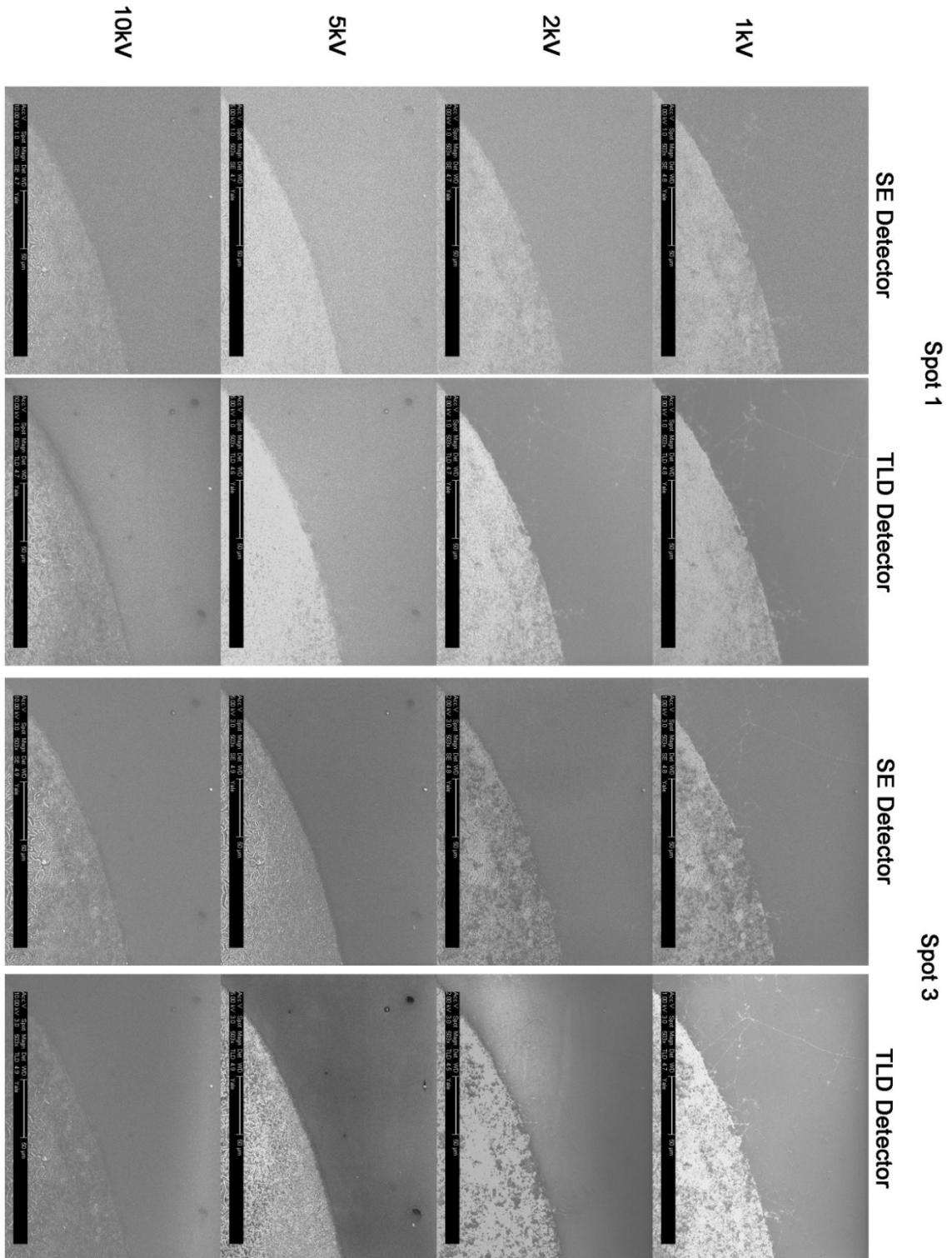


Figure 3.4- SEM micrographs of the same catalyst region under different operating voltages and using different detectors. This demonstrates the benefits of lower beam voltage, larger spot size, and the enhancement from use of the TLD detector.

electronic devices, one must precisely locate these nanotubes and then be able to electrically contact the nanotubes. Imaging nanotubes using SEM, as described above, is not sufficient to then be able to immediately make contact. The fiducial marks can be etched into the substrate, formed by a metal with a lift-off process, or composed of other materials whose properties change when exposed to the electron beam. It would be ideal to be able to create the fiducial marks prior to nanotube growth, but these markers would need to survive the high furnace temperatures associated with carbon nanotube CVD growth. Etching into the substrate would be suitable, but would not be compatible with the eventual antennae metallic contact geometry to the nanotubes if used for densely located fiducial marks. Following global alignment marks etched into the silicon substrate prior to growth, fiducial markers are patterned onto the substrate relative to the global alignment marks in order to aid in local nanotube locating and alignment. These give a general sense of chip orientation and can be easily imaged by SEM. These fiducial markers are a local array of easily recognizable shapes and roman numerals formed using electron-beam lithography. These markers utilize four different elementary shapes whose centers are easily discernible and allow for the design of customized electrode patterns for each nanotube, as shown in Figure 3.5. The specific arrangement of the different 2 micron wide elementary shapes with 50 micron center-to-center separation identifies a unique specific location within the entire array. Initially, following the nanotube growth, we used metallic shapes formed using electron-beam lithography and lift-off made out of thick tantalum, due to its large atomic number, for both the global alignment marks and fiducial marks. Eventually, we moved to a process where the global alignment marks were etched into the silicon substrate and used a negative tone electron-beam resist

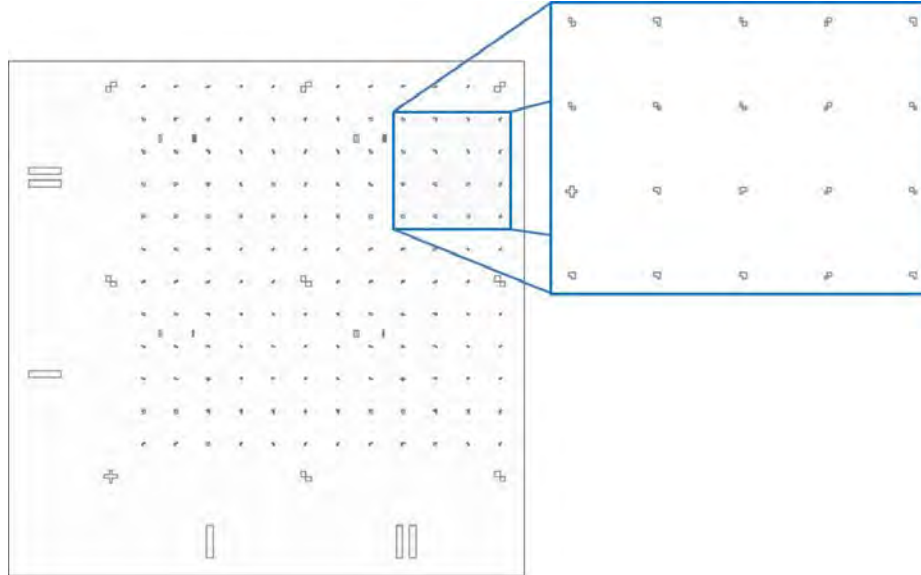


Figure 3.5 – Fiducial marker array pattern based on four different elementary shapes which can be etched into the substrate, formed by a large atomic number metal (Ta) via a lift-off process, or composed of other materials (HSQ) whose properties change when exposed to an electron beam. The unique addressing of these shapes allow for the locating of carbon nanotubes and the design of customized electrode patterns around them.

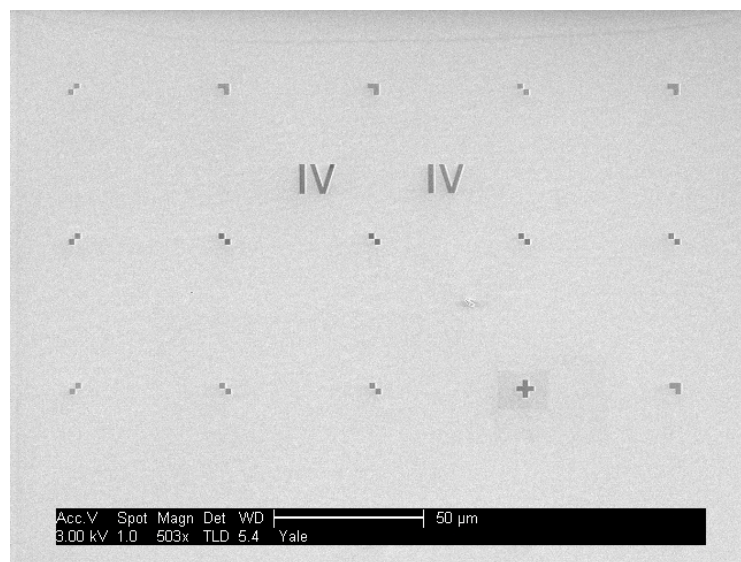


Figure 3.6 – Fiducial marker array composed of the negative tone resist HSQ which transforms into SiO_2 when exposed to an electron-beam. Since transformed HSQ can survive the elevated nanotube growth temperature, this allows for more pristine nanotubes that are not contaminated and damaged by an extra lithography/processing step to produce a fiducial array subsequent to growth. The contrast of the converted HSQ is poor at lower imaging voltages, but also makes for an easier overall process by eliminating the additional electron beam lithography step following the nanotube growth otherwise necessary.

hydrogen silsesquioxane (HSQ), with chemical formula $\text{H}_8\text{Si}_8\text{O}_{12}$, for the fiducial marker grid, shown in Figure 3.6. HSQ, when exposed to an electron beam, transforms into SiO_2 which is able to survive the nanotube growth conditions. The SEM imaging contrast of the converted HSQ is relatively poor at the low imaging voltages (<2 kV) that produce better nanotube imaging. However, the use of HSQ makes for a more favorable process by eliminating the additional electron beam lithography step following the nanotube growth that is otherwise necessary. This allows for more pristine nanotubes, which are not contaminated and damaged by the electron beam during extra lithography steps, as explained above. Once the location of an individual nanotube is known, its diameter can be determined using AFM from the measured height above the substrate, as seen in Figure 3.7. Nanotubes with diameters < 2 nm are likely single-walled and are selected for further study (Purewal 2007). An alternative means of determining the single-walled nature of a nanotube device is measuring its current saturation at large bias. Optical-phonon electron scattering processes stipulate a current saturation of ≈ 25 μA for single-walled nanotube devices (Leonard 2008). However, this method requires electrical contact to first be made to the nanotube, which involves lengthy extra lithography and metal deposition steps in addition to the possibility of producing damage to the nanotube by excessive resistive heating.

3.8 Lithography

Once the specific location address within the fiducial mark array of individual single-walled nanotubes on a chip is established using SEM and AFM, a variety of lithography

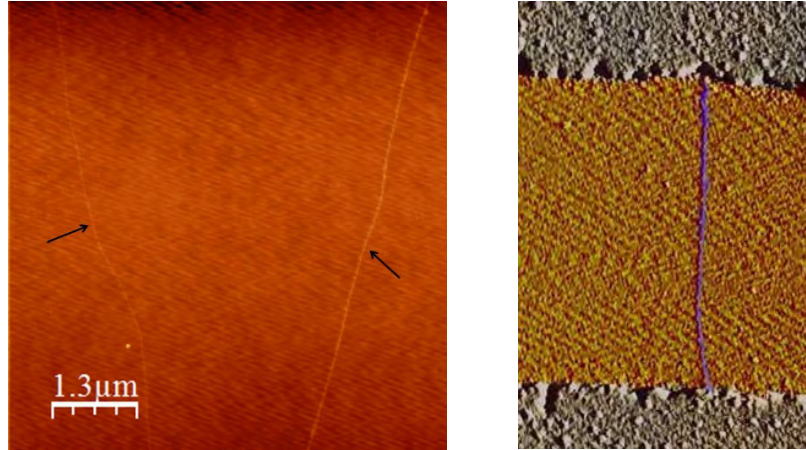


Figure 3.7 – Using atomic force microscopy, once the location of an individual carbon nanotube is determined within the fiducial marker array, its height can be measured. The AFM image on the left shows two carbon nanotubes with different heights in a single scan (denoted by arrows), where the left nanotube has a diameter~1.5 nm, signifying a single-walled carbon nanotube, and the right nanotube appears thicker with a diameter~4 nm, indicating a multi-walled carbon nanotube. The false color AFM image on the right shows a 1 μm long single-walled carbon nanotube section with height~1.5nm in between source and drain contacts.

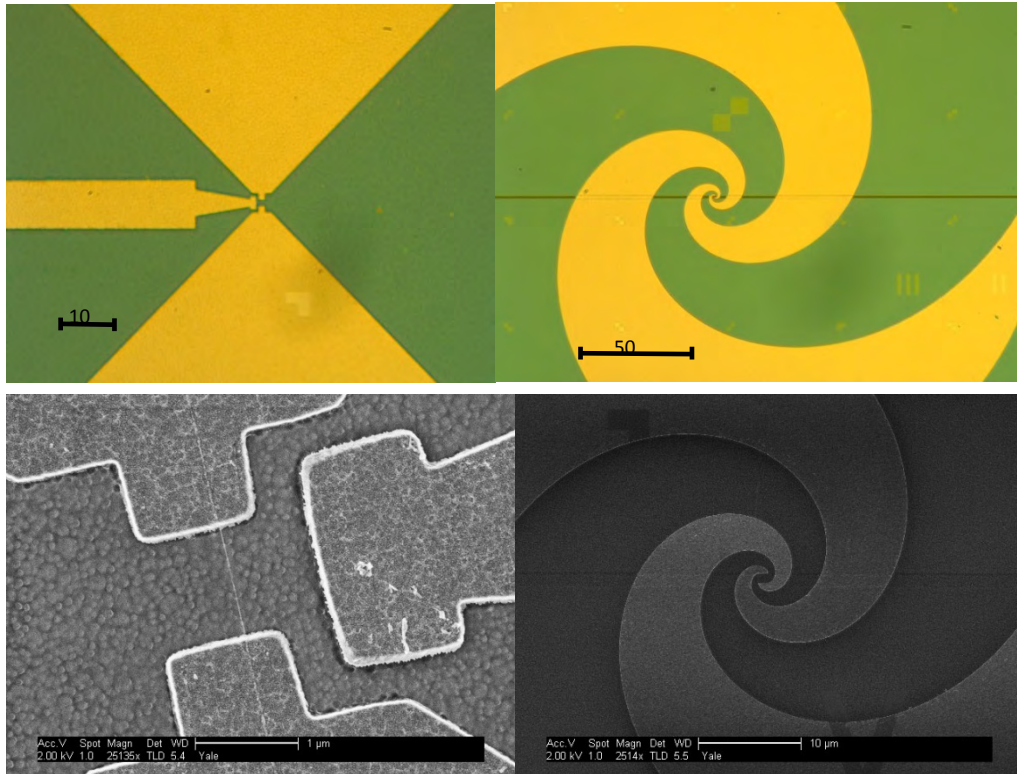


Figure 3.8 – Optical and SEM micrographs of the bowtie (left) and log-spiral (right) broadband antennas with an individual single-walled carbon nanotube at the center and a nearby side-gate or bottom-gate electrode.

tools are available for the fabrication of carbon nanotube electronic devices. Due to the random orientation and location of the individual nanotubes, we select an electron beam process. This provides the greatest customized patterning for each new sample, with an individualized contact pattern custom tailored to the targeted nanotube. Photolithography was initially used for some steps associated with the process and fabrication of the superconducting microbridge devices used for antenna bandwidth standardization, as will be explained in the next chapters. This process was also eventually migrated to an electron beam process once new faster and easier e-beam capabilities were available at Yale. We used a lift-off process of the source and drain contact pattern in the shape of an antenna using bilayer electron beam resist. Initially the electron beam patterning was performed using a converted 30kV FEI XL40 SEM system, but this required substantial manual operation and the patterning accuracy was not ideal, especially when aiming to make contact to a specific nanotube at a given location. This system also only accepted small chip samples so the device throughput was very low. We ultimately moved to the use of a Vistec EBP5000+ electron-beam lithography system employing a 100 kV primary beam obtained as a part of the Yale Institute of Nanoscience and Quantum Engineering. This system can accommodate much larger sample substrate sizes, up to six-inches, and is fully automated using a laser-guided substrate stage with 15nm accuracy. The addition of this tool greatly increased sample throughput. After electron beam patterning in the Vistec system we develop in a ratio of chilled 1:3 IPA to water solution. Additionally, not all typical lithography steps are compatible with nanotube device fabrication; for example, we do not include an oxygen plasma etching after resist development to remove residual resist since the oxygen plasma also readily etches the exposed carbon nanotubes.

3.9 Metal Contacts

Metal contacts are formed using electron beam metal deposition and lift-off in warm acetone following lithography exposure and development. The carbon nanotube source and drain contacts are defined in the lithography step to be the desired shape. The shape of these contacts acts as a planar antenna with far-away bonding pads, as will be explained in Chapter 4. These contacts allow for both dc contact to the nanotube as well as a means for coupling incident terahertz radiation to the nanotube. We use ~100 nm palladium film as the contact metal material since this has been shown to reliably achieve low-resistance electrical Ohmic contact to carbon nanotube devices due to good work function matching (Mann 2003), as will be discussed further. This was performed using the Kurt Lesker EJ1800 Thin Film Deposition System (PETE) or Denton Infinity 22 E-Beam Thermal Evaporation System available in the Yale Cleanroom. Some groups use a titanium adhesion layer since palladium, as a soft material, does not adhere well to the silicon dioxide substrate; however, such an additional layer between the nanotube and contact metal often produce devices with inferior electrical properties characterized by high resistance. The presence of any energy barriers between the metal contacts and the nanotube will present significant effects on this nanoscale system. Sonication is not used to assist the metal lift-off process due to this poor adhesion as well as the tendency of sonication to move and break up carbon nanotubes. Reports in the literature claim that annealing carbon nanotube devices in a furnace at high temperature improve the quality of the metal-nanotube contact interface (Lu 2008) and leads to a reduction of the device resistance. We attempted this annealing process in argon or vacuum on several samples,

but for an unresolved reason found poorer results characterized by devices with increased resistance.

3.10 Planar Antenna

The deposited palladium film serves as a planar antenna. These sorts of antennas have attractive features including low profile, light weight, and ease of integration which has made them popular in modern wireless communication devices. Extensive characterization of these antennas in work for terahertz niobium microbridge bolometric detectors proves their ability to efficiently couple terahertz radiation to a load placed across its feed gap (Reese 2007, Santavicca 2007/2008). When the terahertz radiation strikes the antenna, it produces terahertz currents which propagate along the metal edges until they reach the carbon nanotube. The planar antennas used in this work primarily fall into the category of self-complimentary, where the structure is defined by a single angle (Wiesbeck 2009). This formation produces antennas whose performance is partially independent of source frequency, possessing a real radiation impedance $\sim 100 \Omega$. Two common shapes in this set are bowtie (Compton 1987) and log-spiral (Dyson 1959) broadband antennas, as shown in the optical micrographs of Figure 3.8. A major challenge of this work is the significant impedance mismatch between this low-impedance antenna and the nanotube impedance, $>10 \text{ k}\Omega$ at low frequencies. This impedance mismatch prevents effective power transfer from the incident terahertz beam, resulting in suboptimal performance (Compton 1987). For this work, we can vary the gap space at the center of the antenna design to produce carbon nanotube antenna-coupled

devices possessing various lengths. Typically for this work we focused on nanotube sections measuring 1-5 μm . However, a challenge that results is that misalignment can lead to nanotube sections bridging the gap that are longer than desired. We initially focused on the bowtie design since it allowed for the easy incorporation of a side-gate electrode. The side-gate was shown using simulations with CST Design Studio and EM Software & System's FEKO software to not affect the antenna terahertz radiation pattern. We ultimately progressed to using log-spiral antenna design since this increased the operational frequency range and improved overall performance. However, these are not easily compatible with a side-gate electrode and we had to instead shift to embedding a narrow gate-electrode below the center of this structure, a bottom-gate. These alternative gating approaches are used because the high-resistivity silicon does not allow the substrate to be used as a back-gate. Also, these log-spiral antennas contact a long single nanotube at many locations, unlike a bowtie shape. Extra lithography steps combined with plasma etching are employed to remove unwanted nanotube sections that bridged antenna segments and make them electrically disconnected, as shown in Figure 3.9.

3.11 Suspended Nanotubes

An approach to study the properties of carbon nanotubes and remove some of the effects of the oxide substrate is to examine suspended nanotube devices. Suspended nanotube devices can be obtained a variety of ways. The few suspended devices studied in this work were grown over trenches etched into the SiO_2 prior to nanotube CVD growth. This can avoid some of the effects due to trapped charges in the oxide which degrade nanotube

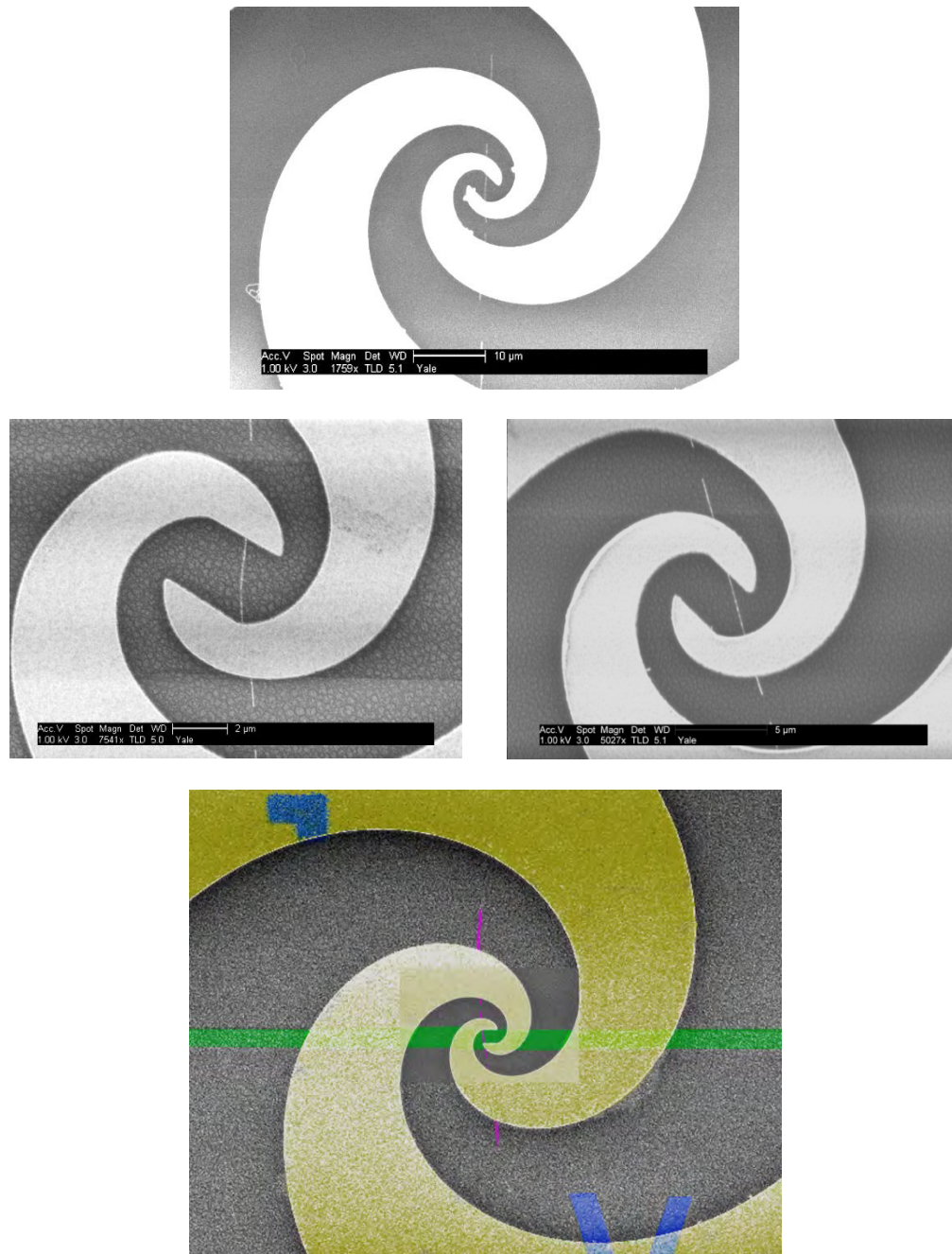


Figure 3.9 – Log-spiral antennas contact a long individual single-walled carbon nanotube at many locations, unlike a bowtie shape. These SEM micrographs show the result of extra lithography steps combined with plasma etching to remove unwanted nanotube sections that bridged antenna segments and make these segments electrically disconnected. The bottom false color micrograph shows the relevant sections of the final antenna-coupled device: fiducial markers (blue), bottom-gate (green), log-spiral antenna (yellow), and etched individual single-walled carbon nanotube (pink).

performance. A potential advantage of this approach for this research comes from suspending the nanotube over a trench which can lead to a lower thermal conductance and thus produce greater nanotube heating. The responsivity, as will be discussed in Chapter 5, is inversely proportional to the thermal conductance for bolometric devices and thus a lower thermal conductance from a suspended nanotube can lead to a greater responsivity. Unfortunately, the many attempts for suspended nanotubes at the center of an antenna structure created in this work in the manner described, as shown in Figure 3.10, were unsuccessful and only resulted in inadequate high-resistance devices.

3.12 dc Characterization

Once all the fabrication steps are completed, initial electrical testing is performed on each nanotube device at room temperature in ambient conditions using a probe station. First, a direct-current low-bias regime measurement is taken at zero gate voltage to determine the natural two-terminal nanotube device resistance, usually biased in the 10 mV range. Large bias voltages or current can damage carbon nanotube devices. The nanotube device acts as a field-effect transistor where a constant bias voltage is maintained across the nanotube by the source and drain antenna contacts, and the voltage applied to the side-gate or bottom-gate electrode is swept, as shown in Figure 1.4. The applied gate electrode voltage produces an electric field that can modulate the electrostatic potential in the nanotube channel which moves the energy band up for negative gate voltage resulting in positive charge in the nanotube channel, and moves the energy band down for a positive gate voltage resulting in negative charge in nanotube channel. Semiconducting nanotubes

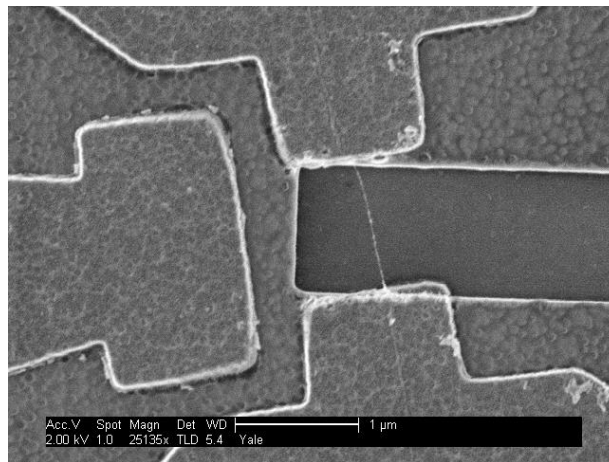
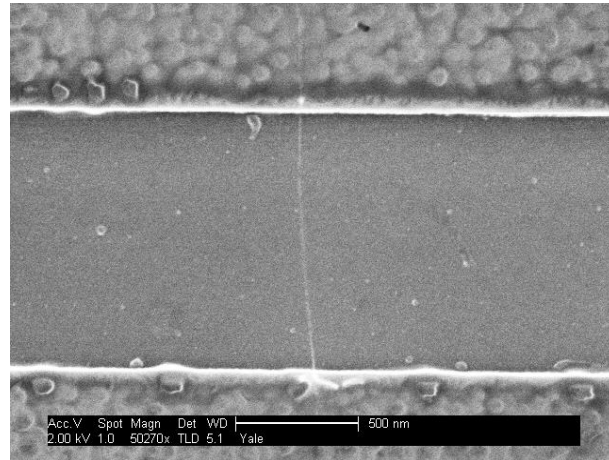


Figure 3.10 – Suspended carbon nanotube devices were grown over trenches etched into the SiO₂ prior to nanotube growth avoiding the effects due to trapped charges in the oxide which degrade nanotube electrical performance.

are easily discerned by seeing a change from a conducting ‘on’ state, low resistance, to a very high resistance ‘off’ state as a function of gate voltage. The gate voltage limits are maintained to avoid breakdown of the silicon dioxide or avoid gate leakage. Nanotube devices are often p-type due to oxygen doping when measurements are taken in air (Derycke 2001). Sections with low-resistance nanotube devices are then scribed into smaller individual 5 x 5 mm chips for direct-current and radio-frequency testing in a dipstick at low temperature and ultimately for THz testing in an IR-Labs optical-access cryogenic dewar.

3.13 Electrostatic Discharge Damage and Device Yield

Small electronic devices face the inherent challenge of sensitivity to electrostatic discharge (ESD). Due to their extremely small size, once metallic carbon nanotubes are contacted, they are extremely electrosensitive and can be significantly damaged by the sudden release of built up charge or the application of abrupt large voltages. This can lead to a dramatic increase in the device resistance or, more typically, can completely destroy a device. Special care must be taken, especially in regard to proper electrical grounding, when dealing with these sensitive devices, especially during the device wirebonding, general handling, and throughout all electrical measurement stages. Countless devices fabricated in the course of this research were damaged despite concerted efforts to keep them as protected as possible. Dramatic SEM images showing a device following metal deposition and then after later device failure from a large side-gate voltage are shown in Figure 3.11.

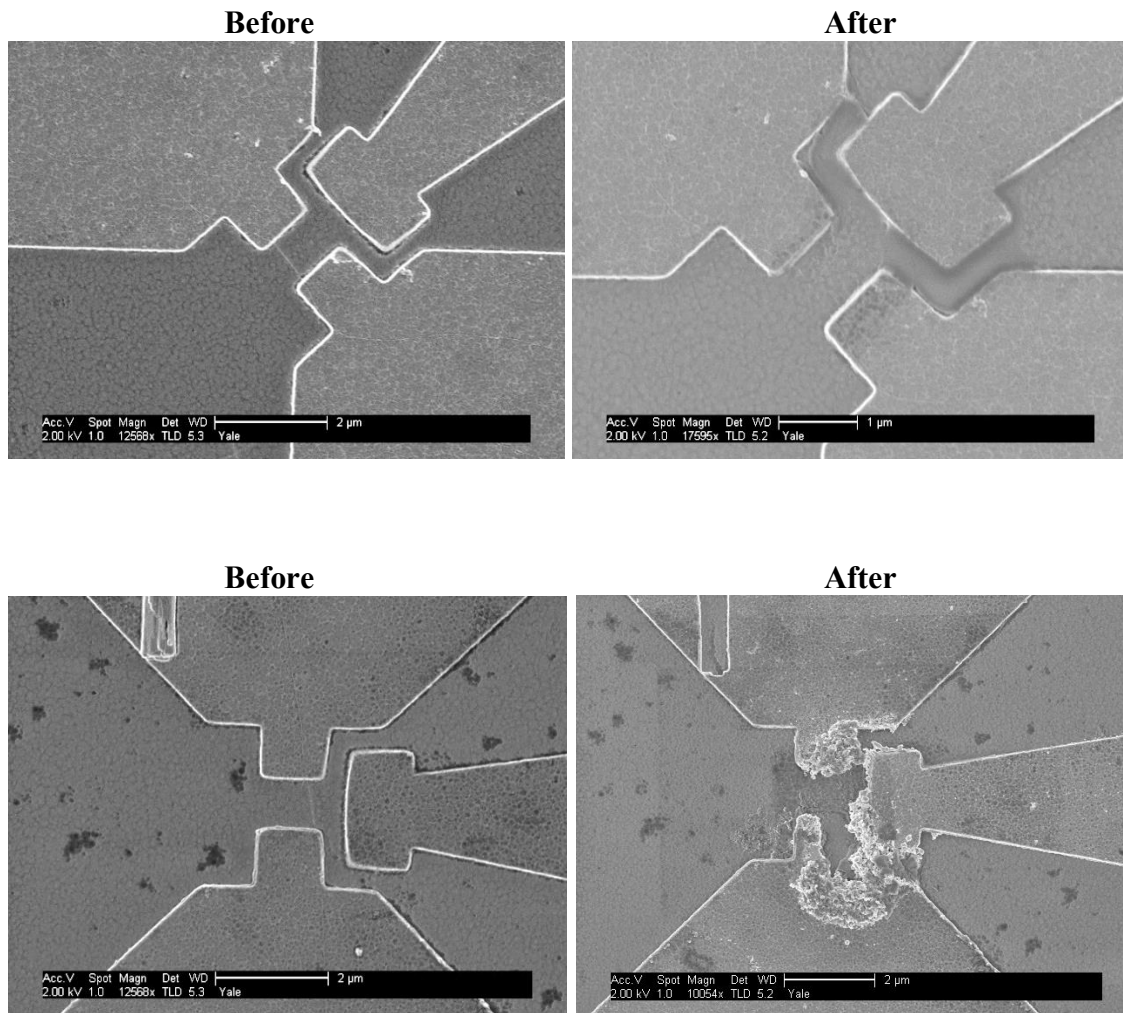


Figure 3.11 – Contacted metallic carbon nanotubes are extremely electrosensitive and can be significantly damaged by the sudden release of built up charge or the application of an abrupt large voltage/current. The top images show a pair of SEM micrographs displaying a device before any electrical measurements (left) and after the application of a voltage ~10 V causing breakdown of the SiO₂ from the gate electrode where the nanotube is no longer visible (right). The bottom image pair shows a device before electrical measurements (left) and after an ESD event that completely destroyed the active region of the device (right).

The device yield in this research was extremely meager when considering the large number of carbon nanotubes grown on a given chip to the number of usable fabricated devices of a high-quality individual single-walled metallic carbon nanotube at the isolated center of a planar antenna with side-gate. After the initial growth, only isolated nanotubes are selected for further study; of these, only single-walled nanotubes are chosen; the processing involved with making electrical contact to these few nanotubes can result in slight nanotube motion on the substrate, resulting in numerous misaligned nanotube devices; of the few aligned nanotube devices, electrical measurements then reveal which of these are metallic as compared to semiconducting; of these metallic nanotube devices, only a handful are shown to be high-quality, characterized by relatively low resistance ($<100\text{ k}\Omega$); for devices in the log-spiral geometry, the oxygen plasma step often would lead to the decreased performance of the center nanotube section or to its complete removal; generally, of these rare devices, many would cease to function due to ESD events or measurement issues, such as gate leakage. Thus, the ultimate device yield as a part of this specific research project was very low and one of the major challenges that had to be faced. Fortunately, with a lot of effort and patience successful devices were indeed possible and allowed for measurements, as will be described in the next chapters.

3.14 Summary

The development of nanoscale systems for operation at high-frequency and low temperature can be very complex. There are many steps involved in the fabrication of carbon nanotube devices: substrate preparation before carbon nanotube growth, the intricate growth conditions necessary for optimal nanotube self-assembly, the process for

addressing the location of individual single-walled carbon nanotubes, and ultimately creating electrical contact for further high-frequency study. The progress that the microelectronics industry has experienced in developing new tools and techniques over the past few decades has allowed for the realization of these very sensitive nanofabricated antenna-coupled single-walled carbon nanotube electronic devices for the THz measurement setup described in the next chapter.

Chapter 4

THz Measurement Setup

4.1 THz Regime

Technology operating in the terahertz (THz) frequency range, the region of the electromagnetic spectrum typically defined from 0.1 to 10 THz (0.4–40 meV), offers advantages in a large range of areas including medical imaging, advanced sensors, security screening, electronics, and wireless communications (Siegel 2002, Ferguson 2002). For example, clothing is transparent at such frequencies and explosives possess spectral signatures easily detectable at terahertz, allowing for the straightforward and effective detection of concealed weapons or dangers without the hazards of conventional means. In addition to the social impact possibilities offered by THz technology, this frequency range presents a versatile scientific tool for the study of fundamental physical phenomenon. It is at THz frequencies that small molecules rotate, excited electrons orbit, gaseous and solid-state plasmas oscillate, biological proteins vibrate, and superconductor energy gaps resonate. Moreover, the speed of operation for solid-state devices is ever increasing and there are many desired applications of systems possessing frequency bandwidths in the THz range. This unique regime finds itself at the fascinating

intersection of electronics and photonics as well as at the transition of the classical depiction to quantum description of electromagnetic waves.

Operating in this radiation range, however, remains a challenge with a deficiency of available technologies for generation and detection. The energy of room temperature corresponds to 6 THz (25 meV) and presents substantial background (thermal) sources of incoherent light. Further difficulties arise due to power limitations, frequency stability and tunability, beam pattern resolution, and atmospheric attenuation by water vapor. Existing between the sophisticated optical tools accessible at infrared wavelengths and the mature microwave capabilities that exist at lower frequencies, as shown in Figure 4.1, this underdeveloped regime is oftentimes referred to as the “THz gap” in the electromagnetic spectrum. Current electronic devices operating in the THz range are expensive, bulky and often require special operating conditions, such as extreme cryogenic cooling, to function.

To solve some of these issues, carbon nanotubes have been considered for a wide range of THz optoelectronic devices owing to their unique electronic properties, such as low heat capacity (Hone 2000) and ultra-fast thermal time constants (Lauret 2003). THz photon-assisted single-electron tunneling detectors based on carbon nanotube quantum dots have recently been proposed as highly sensitive terahertz spectrometers (Rinzan 2012). Other features of carbon nanotubes have led them to be proposed for a variety of terahertz applications (Portnoi 2008, Hartmann 2013), but those are beyond the scope of this thesis.

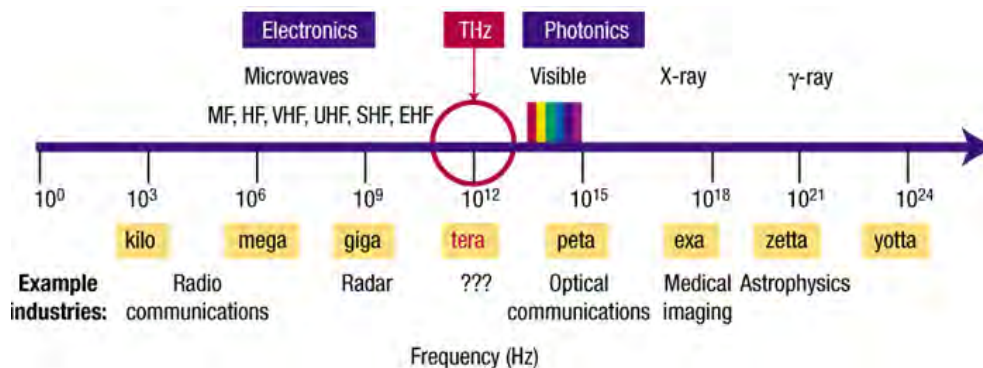


Figure 4.1 – The electromagnetic spectrum highlighting the underdeveloped THz “gap” regime existing between the sophisticated optical tools accessible at infrared wavelengths and the mature microwave capabilities that exist at lower frequencies (Ferguson 2002).

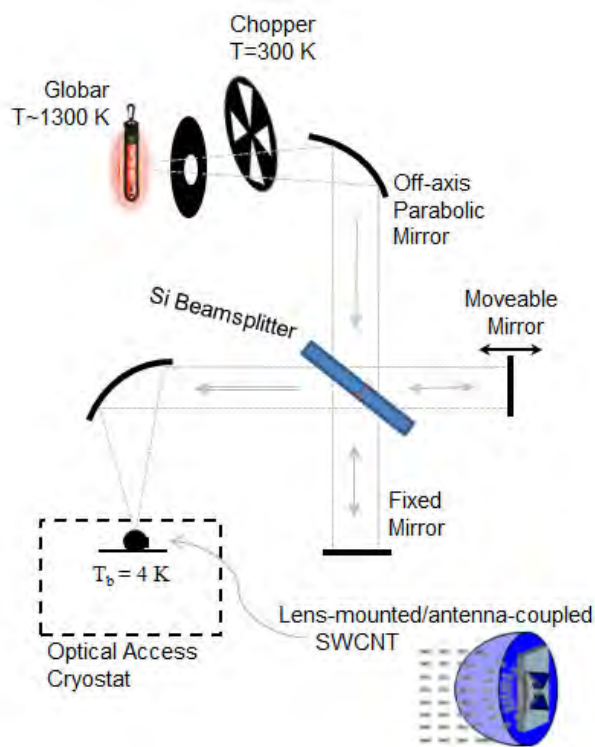


Figure 4.2 – The Fourier Transform Infrared Spectrometer (FTIR) is primarily composed of moveable mirror that can translate back and forth, a mirror fixed in position, and a beamsplitter. The beamsplitter divides the collimated radiation from a hot blackbody globar into two beams which then recombine after reflection from the two mirrors. The recombined beams constructively or destructively interfere depending on the relative displacement between the fixed and moveable mirror beam path lengths. The combined beam is then focused on a lens-mounted antenna-coupled carbon nanotube device in an optical access cryostat for detection.

By using THz radiation we can examine the high-frequency electronic properties of carbon nanotubes, as explained in Chapter 2, as a means of studying and verifying a physical one-dimensional conduction model as well as laying the framework for the development of carbon nanotube devices operating at such high-frequencies. The details of this chapter draw on previous work on terahertz detection using superconducting Nb microbridges (Reese 2007, Santavicca 2007) to develop an experimental technique for probing the one-dimensional behavior of carbon nanotubes using analysis of their THz spectral response.

4.2 Carbon Nanotubes at THz

Theoretical treatments of the possible interaction of high-frequency radiation with carbon nanotubes to extract the propagation velocity have been performed (Ponomarenko 1996, Cuniberti 1998, Sablikov 2000) and P. Burke made important specific predictions (Burke 2002). However, there is very limited experimental work on carbon nanotubes in the THz range. Previous work on individual single-walled carbon nanotubes in the time-domain THz range (Zhong 2008) was discussed in Chapter 2 and reported no conclusion of collective one-dimensional behavior. More recent work at UMass focused on the development of sensitive direct THz detectors based on carbon nanotubes. This work reported on THz detection and generation utilizing bundles of carbon nanotubes (Carrion 2009) using similar techniques to those described in this chapter. Other work has shown the generation of THz radiation from Joule heated single-walled carbon nanotube bundles (Kibis 2007, Muthee 2011). It has been predicted that plasmon resonances in the carbon

nanotubes could be revealed in the THz emission radiation spectrum, but no evidence of this was observed. Muthee reported no discernable change of the THz spectrum as a function of the single-walled carbon nanotube bundle length. The use of heterogeneous bundles of nanotubes instead of a single individual nanotube may complicate and possibly conceal the observation of this behavior. In addition to intrinsic device complications, there are many natural challenges to coupling THz radiation to carbon nanotubes and limited methods for characterizing the experimental results. Besides the lack of available standard THz technology, the inherent high-impedance of nanotube devices makes coupling radiation from free space or low-impedance transmission lines extremely difficult. Novel approaches are necessary to probe the electrical transport of these systems at THz frequencies.

4.3 THz Measurement Setup

In order to efficiently deliver THz radiation to an individual single-walled carbon nanotube, we utilize a quasi-optical coupling technique employing a lens and planar antenna scheme. The broadband THz generation and spectral response measurement is achieved using a Fourier Transform Spectrometer and an optical-access cryostat.

4.3.1 Spectrometer

Our experimental setup for obtaining a THz spectral response uses a Fourier transform infrared spectrometer (FTIR). This is an optical instrument composed of a Michelson

interferometer that measures the spectrum from a radiating source by modulating radiation via interference (Smith 2013). The Fourier transform of the signal then reveals the frequency spectrum. The basic interferometer components are a moveable mirror that can precisely translate back and forth, a mirror fixed in position, a beamsplitter, a source, and a detector. As seen in Figure 4.2, the ideal beamsplitter divides the incoming radiation from a blackbody source into two beams, transmitting half of the radiation to the fixed mirror and reflecting the other half to the moveable mirror. The beams are each then reflected back to the beamsplitter, a 6mm thick, 100mm diameter high-resistivity silicon wafer, where the resulting beams are recombined and passed to the detector. The signal impinging on the detector, which in our case is the nanotube device itself, is a function of optical path difference (OPD), the difference in distance the beams travel through the two arms of the interferometer. The translating moveable mirror produces a frequency-dependent relative phase difference between the two beams. This causes the partial waves to interfere constructively if the OPD is an exact multiple of a wavelength λ , i.e. $2x=n\lambda$, where n is an integer, yielding maximum detector signal/power. Similarly, minimum detection occurs when destructive interference occurs if $2x$ is an odd multiple of $\lambda/2$. A unique point of symmetry and natural reference point exists when the two mirrors are equal distance from the beamsplitter. Here, the OPD is zero and the radiation of all wavelengths/frequencies constructively interfere, leading to a very bright central extremum of the interference pattern. As the OPD grows, a sequence of constructive and destructive interactions between the two portions of beam form a complicated interference pattern called an *interferogram*, which has limited intuitive resemblance to the measured spectrum. A single frequency monochromatic source would produce an

interferogram that is a single sinusoid; a broadband polychromatic source produces a signal dominated by a centerburst, a big spike in the center, and decaying with increasing OPD, as shown in Figure 4.3 for a Nb superconducting bolometer. The OPD interval, Δx , determines the highest frequency accessible by the FTIR, commonly referred to as Nyquist frequency, where $f_{max} = \frac{c}{4 \times \Delta x}$. The translatable mirror employed is controlled by a computer-controlled Ealing EncoderDriver precision linear actuator system with a 10mm range and 0.02 μm linear resolution. We use a typical step size of 20 μm corresponding to a maximum frequency of 3.75 THz. The final spectrum contains information at all frequencies from zero up to the Nyquist frequency at equidistant intervals. However, the scientifically useful information is restricted by the “optical passband” to which the detectors, filters, etc. operate and contribute. The optical passband for our system is from ~ 100 GHz, due to blackbody source aperture iris size of 6 mm, to ~ 4 THz, from infrared/visible filters. The interferogram acquires a broadband spectra collecting all wavelengths simultaneously. This possesses all the Fourier component information and can be translated into a spectrum by performing a Fourier Transform using the *Fast Fourier Transform algorithm* technique developed by Cooley and Tukey (Cooley 1965). The inset (a) of Figure 4.3 shows the spectral response resulting from the Fourier Transform of an interferogram for a Nb superconducting microbridge bolometers for both bowtie and log-spiral antenna structures. An FTIR is capable of high resolution because the resolution limit is the inverse of achievable OPD. The maximum spectral resolution for a FTIR is given by the maximum distance the mirror can travel x_{max} : $\frac{c}{2 \times x_{max}}$.

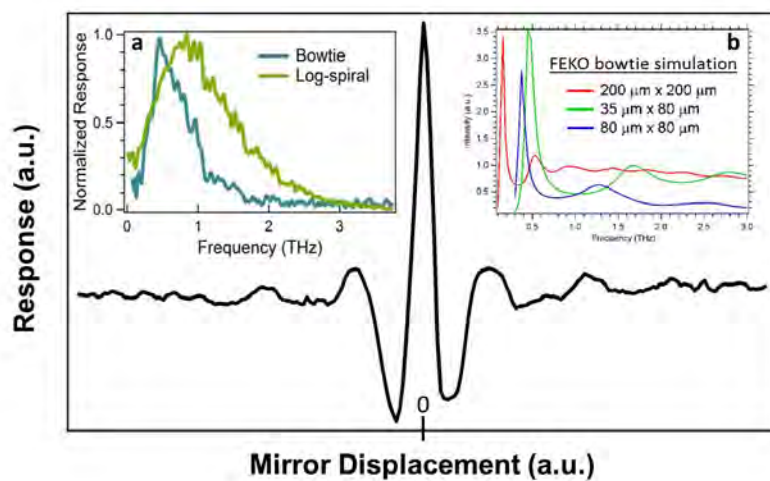


Figure 4.3 – The interferogram, device response as a function of mirror displacement, produced by a broadband source with a Nb superconducting bolometric detector. The signal is dominated by a centerburst, a big spike in the center, corresponding to constructive interference at all frequencies with zero path difference between the spectrometer mirrors. The signal decays and becomes more complicated with increasing path difference. Fourier transforming the interferogram gives the spectral response as shown in inset (a) for two antenna geometries. Inset (b) displays the results of FEKO simulations of the bowtie antenna response for different geometries (courtesy of C. McKitterick). The $200\ \mu\text{m} \times 200\ \mu\text{m}$ bowtie is selected due to its relatively flat response and shows a second-order resonance around 0.5 THz.

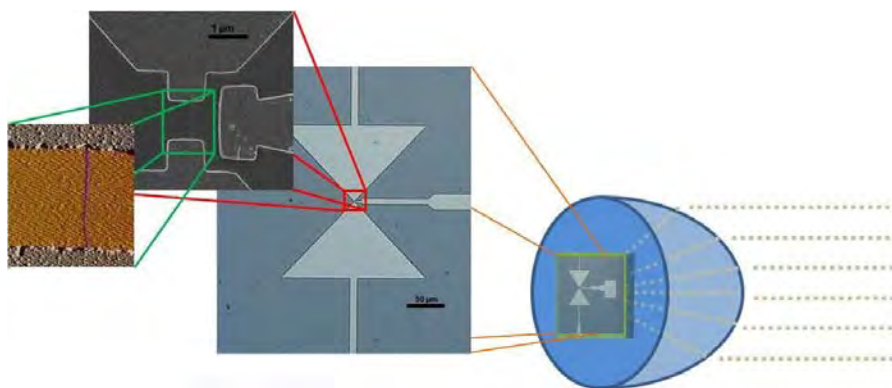


Figure 4.4 – Illustration of the quasi-optical coupling scheme for effectively coupling radiation from free-space to the antenna-coupled nanotube using a hyperhemispherical lens made of high-resistivity silicon.

There are many inherent challenges in the use of FTIR spectroscopy, including background effects, beam alignment, efficiency losses, as well as sampling errors. This approach is not purely reflective of the sample's spectral response but also of the materials composing the FTIR system, including the beam splitter, filters, windows, antenna, and environment. The transmission through each of these will be evident in the ultimate spectral results and must be accounted for. Any FTIR systems will suffer from imperfect overlap of the two light beams upon recombination. Often, the efficiency losses worsen with increasing OPD leading to a gradual loss in information in the interferogram, resulting in apodization, reducing the spectral resolution and features. Noise on the baseline of the interferogram can result from bright point sources due to limited pointing stability, a measure of how much the beam position drifts from the ideal target over time. This stability can be affected by a number of factors both internal and external to the source itself, including physical motion, heat buildup, air currents, and any other variations. A double-sided interferogram records data on either side of the centerburst and can identify asymmetries in the interferogram. Such asymmetries can be derived from various sources, including random noise in the source, such as varying flux levels due to source brightness variations; dispersive elements within the interferometer system leading to varied optical path lengths at different frequencies (the refractive index of dielectric media depends on frequency); maximum signal may not occur precisely at zero path displacement leading to mis-sampling (none of the discrete sampling positions coincides exactly with the proper position of zero path displacement); phase delays of the optics or read-out electronics. Another issue is that the Fourier Transform on discrete measurements only approximates the continuous Fourier Transform. Adding zeros to the

end of the interferogram before Fast Fourier Transform is performed can increase the number of points per frequency in spectrum. Thus, this zero-padding of the interferogram has the effect of interpolating the spectrum, reducing error and increasing resolution (Herres 1985).

In addition to the basic spectrometer components, a variety of parabolic focusing elements are used in our FTIR system. These 90-degree off-axis parabolic mirrors are used for collimating and focusing light external to the basic interferometer. These parabolic mirrors are broadband, reflecting nearly all the incoming radiation up to high frequency and do not exhibit any dispersion. Another key feature is that they do not display any chromatic aberration, so the focal spot stays the same for any frequency/wavelength. We align the mirrors by locating the signal from the globar using a near-IR viewer. The chosen parabolic shape is ideally suited for collimating the light from small sources. Light from a point source at the focus of the parabola will be transformed after reflection into an ideally parallel beam. Conversely, this also tightly focuses collimated beams of radiation, where a parallel beam is focused into tiny focal spot which is approximately plane wave. This remains true for any part of the ideal parabola, so any subsection can be used tolerating significantly less meticulous alignment. We use a parabolic mirror to collimate the light from our blackbody globar point source. Another parabolic mirror carefully aims the THz beam at a 25 μm thick Mylar (polyethylene terephthalate) sheet window and expanded Teflon (polytetrafluoroethylene) sheet, used as infrared and visible filter, attenuating strongly above 4 THz, behind which the antenna-coupled nanotube device was mounted in a He cryostat IR Labs liquid ^4He optical-access cryostat and electrically connected using SMA

connectors allowing for rf measurements. The THz power that ultimately reaches the antenna-nanotube device is reduced due to numerous optical losses which must be accounted for when calculating intrinsic responsivity. The entire FTIR system and cryostat are contained in a dry nitrogen box with a relative humidity $\leq 5\%$, measured with a commercial hygrometer, since water vapor absorbs radiation in the THz frequency range. This setup allows for the dc, rf and THz characteristic measurements of carbon-nanotube devices as a function of temperature with the temperature sensor mounted on the sample metal block.

4.3.2 Quasi-Optical Coupling

A simple means of effectively coupling radiation from free-space to a detection element is through the use of a quasi-optical coupling scheme, originally introduced by Rutledge and Muha (1982). In this setup, as shown in Figure 4.4, a hyperhemispherical lens focuses the free-space signal onto a broadband planar microantenna integrated on-chip. The antenna collects the THz radiation, converting the electromagnetic wave into a high-frequency electrical signal delivered to the sensing device, e.g. a carbon nanotube or superconducting microbridge. The antenna also serves as the dc source and drain electrodes for measurement of the dc output signal. The dielectric lens is made of high-resistivity silicon with a 6 mm diameter hemisphere and an extension length such that the radiation will strike the antenna at the focal point of the lens. The radiation directivity can be strongly dependent on this extension length (Filipovic 1993). The lens and antenna are carefully aligned with one another using the aid of an alignment piece under an optical

microscope. The alignment piece is a high-resistivity silicon chip with patterned markings on both sides, one side with orthogonal lines pointing towards the chip center and the other side with a concentric circle equal in diameter to that of the lens centered on the chip. The lens is aligned with the alignment circle by hand under optical microscope magnification and carefully glued in place using ultraviolet curing glue. Afterwards, the desired antenna device is similarly glued in place on the counter-side of the alignment piece. This method matches the dielectric constants between the lens and substrate, so that no substrate modes will develop. This configuration includes additional advantages in that dielectric lenses can produce high-quality focused Gaussian beams that can be efficiently coupled, and it also leverages the preferential coupling of radiation energy from the high dielectric medium and thus to the antenna through the substrate. Thus, most of the incoming THz power is radiated towards the device. The lens diameter is sufficiently large so that curved surface is in the far field of the antenna. The incoming THz radiation becomes a planar wave at the focal plane of the lens as the beam is narrowed and is efficiently coupled to the antenna and converted into THz currents. The THz currents propagate along the antenna metal edge and enter the carbon nanotube device as the load in the middle of the antenna gap. Misalignment of the lens can result in a skewed interferogram and power loss. This can cause a cutoff of higher frequencies since the focal spot in this range possessing finer wavelength provides less alignment tolerance for the signal satisfactorily reaching the antenna. The antenna-coupled device and lens combination is mounted on copper sample holder for two-wire contact plus a gate connection and are then wirebonded to make dc contact to the nanotube device and for placement in an optical-access cryostat.

4.3.3 Planar Antennas

Planar antennas are lithographically patterned nearly-two-dimensional structures on a dielectric substrate to couple incident radiation from a spatially distant source that radiates electromagnetic waves in its direction to a detector with sub-micron dimensions. The antenna dimension is typically a large fraction of the incident radiation wavelength. The planar antenna configuration limits the radiation coupling to only a single mode. The Nyquist thermal noise formula gives the single mode model of a planar antenna with an equivalent circuit as a voltage source connected to an antenna impedance and a load impedance. In this model, for the case of perfect impedance matching and low-frequency Rayleigh-Jeans limit ($k_B T \ll hf$), the power delivered to the antenna is given by $P = k_B B T$, where k_B is the Boltzmann's constant, B is the coupled antenna bandwidth, and T is the temperature (Santavicca 2009).

There are two classes of planar antennas: resonant and non-resonant (or travelling wave) antennas. Dipole antennas are typically resonant antennas with relatively narrow bandwidth, where a half-wavelength dipole can be made to resonate with a purely real input impedance. The resonance condition for a half-wave dipole is the antenna's physical length corresponding to half a wavelength. Bowtie and spiral antennas are examples of non-resonant antennas and they possess wide bandwidth. For this thesis work, large bandwidth antennas are preferable for observing the periodic standing wave resonances on a carbon nanotube over a large frequency range. The planar antennas used primarily fall into the category of self-complementary where the structure is defined by a

single angle (Wiesbeck 2009). For ideal conditions, such as perfect conductors and dielectrics with exact dimensions, the invariance under change of scale allows the antenna performance to be partially independent of source frequency. This provides a low real radiation impedance $Z_{ant} \approx Z_o/\sqrt{2(1 + \epsilon)}$ for self-complementary antennas, where Z_o is the impedance of free space and ϵ is the dielectric constant of the substrate material. The initial THz antenna used in this work consists of a 90° self-complementary bowtie structure realized by e-beam evaporation of Pd. A bowtie antenna is a bitriangular sheet of metal, defined by a bow angle, with a feed at its vertex and would be frequency independent if its sides extended to infinity. However, practical bowtie antennas must have a finite gap between feed points and finite size, leading to limited bandwidth. Similarly, a spiral is a geometrical configuration described by angles, and thus frequency independent, that are circularly polarized with the winding sense of the spirals. Calculated radiation efficiencies for dipole, bowtie, and spiral IR antennas are 20%, 37% and 25% respectively (Gonzalez 2005). Substrate effects, such as unwanted modes in a thick substrate, can vary as a function of frequency and also affect antenna efficiency. In order to couple a THz signal to an individual nanotube, we utilize a bowtie antenna with overall dimensions measuring 200 μm by 200 μm or log spiral antennas measuring 300 μm by 300 μm . The low antenna impedance of $\sim 100 \Omega$ is significantly mismatched to the nanotube impedance $> 10 \text{ k}\Omega$. This prevents effective power transfer, resulting in very small signal and suboptimal noise performance. However, a $\sim 10 \text{ k}\Omega$ antenna would be well-matched to a nanotube, but would be very poorly matched to free space if it could be constructed. The antenna geometries described were selected for their simplicity, robustness to variation in geometrical parameters, and the ease of including a side-gate.

The antenna fabrication details were discussed in Chapter 3 and, as mentioned there, numerical simulations show that the side-gate does not significantly affect the antenna properties.

4.3.4 THz radiation source

All matter with a temperature above absolute zero emits thermal blackbody radiation, and THz radiation is emitted from anything with a temperature above a few Kelvin. The cosmic microwave background radiation extends weakly to the THz range. Broadband sources exist for a variety of frequency ranges of the electromagnetic spectrum. Mercury arc lamps are typically used for near-infrared radiation, tungsten-based filaments for the mid-infrared, and silicon-carbide globars for far-infrared. Thus, as our broadband thermal source we utilize a Surfaceigniter Corp. model 1034K silicon-carbide globar. The temperature of the globar and its corresponding THz output varies with the bias voltage. The globar output temperature was determined as a function of the applied voltage/current to the globar by measuring the brightness of the radiation produced by the globar (Connelly 2009), as shown in Figure 4.5. This approach uses a calibrated consumer digital camera to take a picture of the globar and then decomposes the image into various wavelengths using the camera's color filter array. The temperature of the globar is then established from the image brightness. We choose a typical operating voltage of 20 V for globar function, corresponding to a temperature of ~ 1300 K. At ~ 1 THz, the emission is essentially frequency independent, since $k_B T \gg hf$.

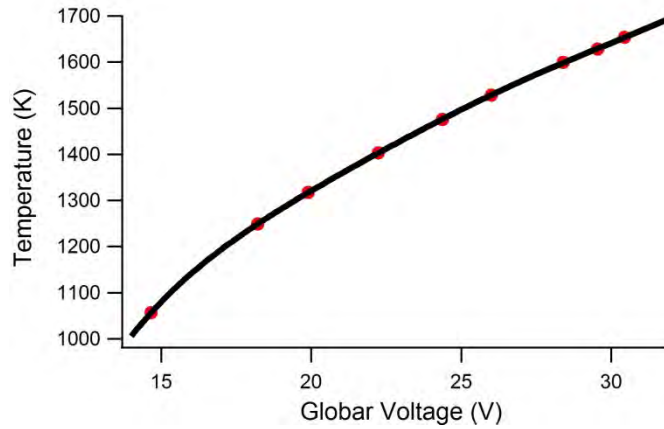


Figure 4.5 - Global output temperature as a function of the applied voltage obtained by measuring the brightness of the global output radiation with a calibrated digital camera.

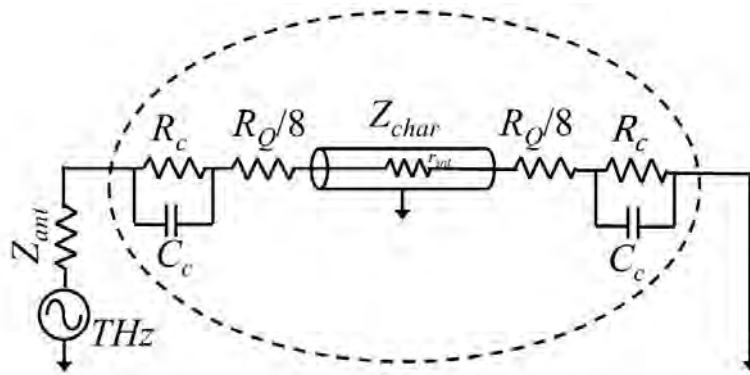


Figure 4.6 – Equivalent circuit model of a single-walled carbon nanotube (from Figure 2.4 in dotted ellipse) with a planar antenna acting as a THz voltage source with an antenna impedance Z_{ant} . The nanotube is shown to include a contact resistance R_c , contact capacitance C_c , resistance quantum R_Q ($=26 \text{ k}\Omega$), characteristic impedance Z_{char} , and internal resistance per unit length r_{int} .

The THz source seen by the antenna-coupled device is modulated between the hot global ($T \sim 1300$ K) and the “cold” room temperature ($T \sim 300$ K) by an optical chopping wheel rotating at a rate of ~ 300 Hz. The power varies by $T_{hot} \sim 1300$ K to $T_{cold} \sim 300$ K. This chopper was positioned initially in front of the cryostat window and later moved in front of the global. The low-frequency antenna-coupled nanotube output, the difference in voltage across the device with a tunable dc bias current applied to the device, is read out with a lock-in amplifier at the chopping wheel reference frequency. The chopper serves as a modulation signal, thus only measuring the voltage difference that is in phase with the THz power modulation. The effective temperature of the signal reaching the chopper is taken as $T \approx 650$ K due to the beamsplitter, which only couples half of the global power to the device. The chopper is at room temperature, but we take its effective temperature to be $T \approx 250$ K to account for partial reflection off the surface of the chopper from the colder cryostat environment when the chopper is position in front of the cryostat. This results in a temperature difference $\Delta T \approx 400$ K, assuming perfect optical and THz coupling.

The THz electrical coupling is understood with the equivalent circuit of the planar antenna and THz source combination of Figure 4.6, where the antenna, with a low source impedance $Z_{ant} \approx 60 \Omega$, presents a THz voltage signal to the nanotube transmission line model presented in Chapter 2. The rms THz voltage difference at the single-mode antenna terminals due to the blackbody source chopping is

$$\Delta \langle V_{THz}^2 \rangle = \eta (4 k_B B \Delta T Z_{ant}) \quad (4.1)$$

where k_B is Boltzmann's constant, B is the antenna bandwidth, ΔT is the source temperature difference, and η is the power coupling efficiency of the optical system. The rms THz voltage is typically on the order of 300 μV and does not include the significant impedance mismatch between the antenna and carbon nanotube, which will only transmit at best $\sim 1\%$ of this THz voltage.

4.4 Superconducting Bolometer as Normalization

Previous work by our lab has utilized superconducting hot electron bolometers for terahertz sensing applications. Using such devices integrated into the FTIR system provided measurements of the bandwidths of the different antenna geometries (Reese 2007, Santavicca 2007). Using an impedance-matched antenna-coupled broadband Nb absorber/bolometer, we determine the optical coupling efficiency and the antenna bandwidth. Excluding the interferometer, we found an optical coupling efficiency of $\eta \approx 15\%$ (Santavicca 2007). In this measurement, the blackbody source filled the entire field of view of the device lens. This value of $\eta \approx 15\%$ is taken as an upper bound for the coupling efficiency with the interferometer, as any misalignment of the interferometer or mismatch between the interferometer beam pattern and the antenna beam pattern will result in a decreased η . Equation 4.1 is in the low-frequency blackbody limit for coupling to a single-mode detector, which is appropriate for our carbon nanotube device at the THz frequency, f , since $f < k_B T / h \approx 5$ THz for $T = 250$ K. The frequency response of the antenna and the optical system was measured with an Nb bolometer at the bowtie antenna feed instead of a nanotube. The device voltage response at the chopping

frequency is measured as a function of mirror displacement to produce an interferogram, which is then Fourier transformed to determine the spectral response. We find that the frequency response of the bowtie antenna plus optical system peaks at 0.5 THz with a bandwidth B of 0.6 THz, as shown in Figure 4.3. The expected maximum power delivered to our device (without taking into account impedance matching) for a bowtie antenna from Equation 4.1 is ≈ 1 nW. Numerical simulations with FEKO simulation software show that the response peak corresponds to the second-order antenna resonance as shown in inset (b) of Figure 4.3; the first-order resonance is below the low-frequency cut-off of our optical system. These Nb devices serve as a normalization for the background spectral response of the measurement system, including the FTIR and antenna-coupling. By focusing on the dc voltage response to the *total* THz power in the antenna bandwidth we can identify the dominant mechanism responsible for the THz-frequency single-walled carbon nanotube device response.

4.5 Summary

The THz regime offers an exciting and new area for exploration and remarkable applications; however, there are many inherent challenges to its development and exploitation. Using a Fourier Transform Infrared Spectrometer system and optical-coupling scheme, we are able to deliver a broadband THz signal to a lens-mounted finite-length, antenna-coupled, single-walled carbon nanotube, detect the device response to this incident power, and form an interferogram. From this we determine the nanotube's spectral response and seek out indications of the fundamental 1D collective plasmon

standing wave resonances that are predicted for this system. The measurements described in the next chapter are challenging due to the lack of readily available commercial THz equipment, the small THz signals accessible by this measurement setup, and the intrinsic large impedance mismatch between free space and nanoscale systems.

Chapter 5

Carbon Nanotube THz Detection Mechanisms

5.1 Introduction

Carbon nanotubes have been proposed for a wide range of electronic device applications because of their unique properties. Several groups have investigated the high-frequency electrical properties of nanotubes in order to assess their potential for use in terahertz (THz) frequency devices (Burke 2002, Fu 2008, Carion 2009, Hartmann 2014). For application as high-frequency detectors, open issues remain regarding the detection mechanisms and the possible limiting effects of the device capacitance. We study the high frequency response of individual carbon nanotubes due to both a bolometric effect and the electrical nonlinearity of the contact resistance at low temperature. For nonlinear detection, we conclude that the contact capacitance will not strongly limit the THz performance.

5.2 Detection Mechanisms

There are two common high-frequency (radiofrequency and THz) detection mechanisms: bolometric detection and nonlinear detection. A bolometric detector can sensitively detect incident electromagnetic radiation through a heating response by generating a dc voltage,

or other change of a measurable parameter, in proportion to the amount of incident radiation power. Carbon nanotubes, with extremely small heat capacity (Hone 2004) and weak electron-phonon coupling (Park 2004, Santavicca 2010), could offer advantages for bolometric detection. Graphene, with similar advantageous properties, would make an excellent THz bolometric detector (McKitterick 2012). A nonlinear, or diode-like, detector generates a dc output signal due to the nonlinearity in the current-voltage (I - V) characteristic of the device. Differences in the device resistance for the positive and negative cycles of an incident ac signal produce power conversion as determined, to leading order, by the magnitude of the second-derivative of the I - V curve. An antenna allows for the transformation of incident radiation into an ac electrical signal, and these two mechanisms allow for the measurement of an associated dc output.

5.2.1 Bolometric Detection

A bolometric device is a type of thermal detector which collects incident radiation power P_{abs} in an absorber and measures the resulting change in temperature ΔT via a thermometer. ΔT is given by $P_{abs} = G_{th}\Delta T$, where G_{th} is the thermal conductance between the active element of the detector and its environment. If instead an energy E_{abs} is absorbed, then $E_{abs} = \mathcal{C}\Delta T$, where \mathcal{C} is the heat capacity of the active element. The absorber and thermometer need not be distinct elements. If the device exhibits a temperature-dependent electrical resistance $R(T) = R_o + (dR/dT)\Delta T$, this heating results in a change in resistance ΔR . This can be measured by means of a dc current bias, I_{dc} , and measurement of the change in the dc voltage across the bolometric device, $V_{bolo} =$

$I_{dc}\Delta R = I_{dc} \left(\frac{dR}{dT} \right) \Delta T$. Bolometric detection can be independent of the radiation wavelength and only depends on the total deposited energy or power. The more absorbed radiation the greater the heating effect and the more dramatic the change in resistance. A device whose resistance significantly varies as a function of the temperature, where a small temperature change induces a large resistance change, yields a detector with greater sensitivity. Superconductors possess very sensitive temperature-dependent resistances when biased at their superconducting transition and are often used for this purpose as transition edge sensors (Richards 1994). Frequently, for devices known as hot-electron-bolometers, the electron-phonon interaction is weak enough that the lattice temperature remains approximately unchanged from the bath temperature, and only the electron system temperature changes due to electronic heating. In this situation, the relevant thermal conductance is that of heat escaping from the electron system.

An important figure-of-merit for a bolometer is the voltage responsivity S_V , reflecting the change in voltage across the thermometer per watt of power collected in the absorber, $S_V = \Delta V / P_{abs}$. Thus, the measured voltage for bolometric detection can be determined by:

$$V_{bolo} = S_V P_{abs} = \left(\frac{I_{dc}}{G_{th}} \frac{dR}{dT} \right) P_{abs} \quad (5.1)$$

This result assumes that the Joule heating from the bias current is negligible; otherwise we must take into account the effect of electrothermal feedback (Richards 1994), which

modifies the above equation $V_{bolo} = S_V P_{abs} = \frac{\left(\frac{I_{dc}}{G_{th}} \frac{dR}{dT} \right) P_{abs}}{1 + \left(\frac{I_{dc}^2}{G_{th}} \frac{dR}{dT} \right) \left(\frac{R - R_L}{R + R_L} \right)}$, where R_L is the load

resistance. For a bolometric detection scheme, by measuring the dc device characteristics,

such as the temperature-dependent resistance and the thermal conductance, for a given dc bias and incident power, we can determine the expected dc output voltage. A typical single-walled metallic carbon nanotube possesses a moderate temperature-dependent resistance and small thermal conductance, making it a good candidate for detecting THz radiation using a bolometric detection scheme.

5.2.2 Nonlinear Detection

Nonlinear devices used as direct detectors are based on electrical rectification, where an ac signal is converted to a dc signal. Rectification will occur in any device with a nonlinear current-voltage relation. For a Schottky diode, the nonlinearity is due to the Schottky barrier at the interface between a metal and a semiconductor. Following the approach of Cowley & Orenson (Cowley 1966), using the Taylor expansion of $V(I)$ to second order, the time-averaged dc voltage output for a nonlinear detector is given by:

$$\begin{aligned}
 V(I_{dc} + \delta i) &= V_{dc} + \left. \frac{dV}{dI} \right|_{I_{dc}} \delta i + \frac{1}{2} \left. \frac{d^2V}{dI^2} \right|_{I_{dc}} \delta i^2 + \dots \\
 \langle \delta V \rangle &= \langle V(I_{dc} + \delta i) - V_{dc} \rangle \\
 &= \left\langle \left. \frac{dV}{dI} \right|_{I_{dc}} \delta i \right\rangle + \left\langle \left. \frac{1}{2} \frac{d^2V}{dI^2} \right|_{I_{dc}} \delta i^2 \right\rangle \\
 \Delta V_{dc} &= \frac{1}{2} \left. \frac{d^2V}{dI^2} \right|_{I_{dc}} \Delta \langle I_{THz}^2 \rangle
 \end{aligned} \tag{5.2}$$

Thus, the dc nonlinear voltage output can simply be determined from the second derivative of the I - V curve and the high-frequency current through the device. As previously discussed, carbon nanotubes exhibit a nonlinear behavior known as a zero-bias

anomaly at low temperature and low bias, and this can be used for nonlinear THz detection.

5.3 Temperature Dependent Behavior

The electrical behavior of the nanotube device is characterized by the change in resistance as function of temperature. Semiconducting nanotubes increase in resistance with decreasing temperature. Quasi-metallic nanotubes decrease in resistance with decreasing temperature, but often show an upturn at low bias and low temperature. The dc resistance $R_{dc} = V_{dc}/I_{dc}$ as function of temperature for a 5 μm long metallic nanotube device measured at moderate bias current ($I_{dc} = 300$ nA) is shown in Figure 5.1. The approximately linear temperature dependence of the dc resistance observed above 50 K is consistent with electron-acoustic phonon inelastic scattering (Park 2004, Jishi 1993).

5.3.1 Thermal Conductance

To determine the expected bolometric response of an individual single-walled carbon nanotube due to THz radiation, we first need to determine the thermal conductivity G_{th} for cooling of the nanotube electron system (Galeazzi 2003). To find this we employ a technique using the device electrical resistance as a thermometer of the electron system (Gershenson 1990). The Joule-heating of a nanotube due to an electrical bias current is used to directly assign the electron temperature. This is accomplished by simply relating the dc characteristics of the equilibrium nanotube resistance as a function of temperature

with the equilibrium nanotube resistance as a function of current. The power P dissipated internal to the nanotube from Joule-heating is given by the dc current and resistance as I^2R . Johnson noise thermometry, a measure of the thermal fluctuations of the system, enables us to probe the temperature T of the nanotube electron system. Using $G_{th}=dP/dT$, we determine the thermal conductance for an individual nanotube as both a function of temperature and of length (Santavicca 2010).

To study the inelastic processes for the nanotube electron system to lose energy to its environment and determine G_{th} , we examine an individual single-walled carbon nanotube device, denoted as NT-1, contacted at various electrode separations of length segments measuring 2, 5, 20 and 50 μm . We apply a global back-gate of -30V using a doped silicon substrate with an oxide layer beneath the nanotube and plot the dc resistance as function of temperature, as in Figure 5.1. We also plot the measured dc resistance as a function of I_{dc} at bath temperatures of 4.2 K and 77 K. The increase in R_{dc} with increasing I_{dc} is due to Joule heating of the electron system in the nanotube. For $T_b < 20$ K a local maximum in R_{dc} is seen at zero bias current. This zero-bias anomaly (ZBA), which will be discussed in more detail later but, as explained in Chapter 2, is attributed to a contact effect, a reduced density of states for tunneling into a Luttinger liquid or dynamical Coulomb blockade. We can use the $R_{dc}(T_b)$ and $R_{dc}(I_{dc})$ data to then assign an average temperature of the electron system as a function of dc bias current $T_e(I_{dc})$.

Johnson noise thermometry offers an alternate means for directly determining the average electron temperature as a function of I_{dc} for a Joule-heated nanotube. For a resistor with uniform electron temperature T_e , the Johnson noise power coupled into a matched load in the low frequency limit ($hf \ll k_B T_e$), is $P_J = k_B T_e B$, where B is the

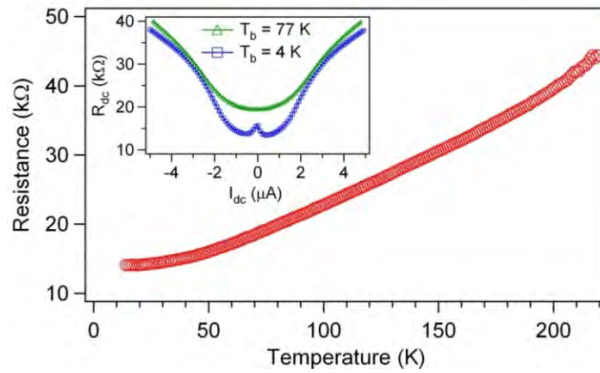


Figure 5.1 – dc resistance of a 5 μm long single-walled metallic carbon nanotube as a function of bath temperature measured with a dc bias current of 300 nA. (inset) dc resistance as a function of dc bias current at bath temperatures of 4.2 and 77 K. The increase in resistance at increasing bias current is due to Joule heating and the small resistance increase around zero bias is referred to as the ZBA (Santavica 2010).

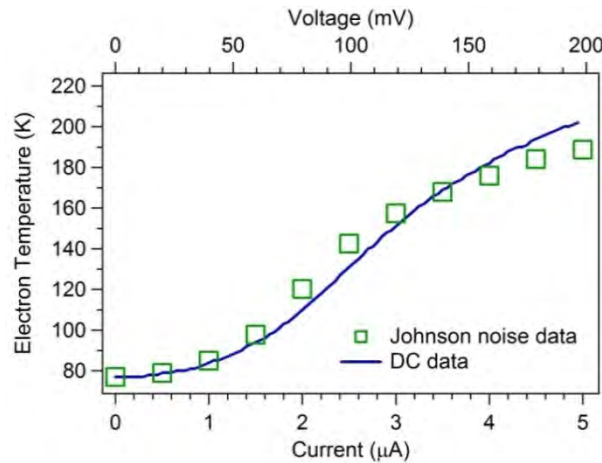


Figure 5.2 – Average electron temperature of a carbon nanotube section as a function of bias current at $T_b = 77\text{ K}$ determined from Johnson noise thermometry and from the dc data in Figure 5.1. The corresponding bias voltage is shown on the top axis. This confirms that the increase in resistance with increasing dc bias is indeed due to self-heating (Santavica 2010).

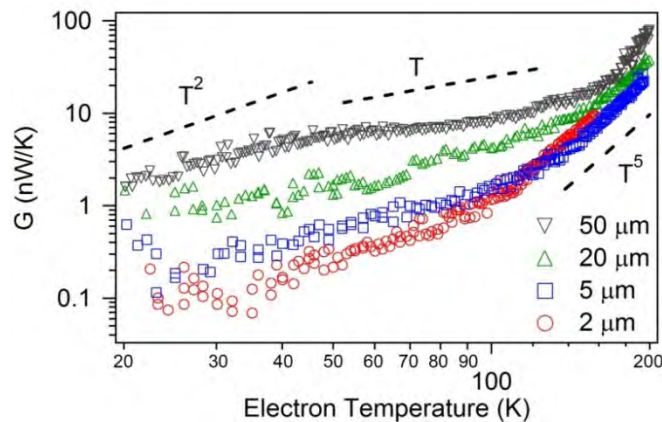


Figure 5.3 – Thermal conductance as a function of average electron temperature for various carbon nanotube length segments at a bath temperature of 4.2 K. The dashed lines illustrate different power dependencies with temperature (Santavica 2010).

measurement bandwidth. We employ a differential measurement technique with a bias current that switches from zero current to finite current at low frequency. We measure at temperatures < 200 K, where lower temperature allows for greater thermal impedance between the electron and phonon systems, so that input power is coupled directly to the electrons. The device noise is measured with a 50Ω microwave amplifier and a bandpass filter. We account for the coupling mismatch between the nanotube and amplifier at each bias current value. The amplifier output is coupled to a diode to measure power, where the diode response is read out on a lock-in amplifier synchronized to the on-off bias current frequency. We assume the total internal resistance $R_{int} = r_{int} \ell$ of Figure 4.6 is heated by the bias current and R_c is temperature independent, where any power dissipated in contact resistance remains in the relatively massive contact thermal reservoirs. Shown in figure 5.2, we compare the temperature increase of the $5 \mu\text{m}$ nanotube sample at 77K (to avoid the ZBA feature) relating the thermal equilibrium $R_{dc}(T_b)$ data to the nonequilibrium $R_{dc}(I_{dc})$ data with the temperature determined by the Johnson noise measurement. We find reasonable agreement between the temperatures determined using these two different approaches. Johnson noise thermometry confirms that the increase in R_{dc} with increasing dc bias is indeed due to self-heating. Thus, away from the ZBA, the dc resistance is a measure of average electron temperature in both the equilibrium ($I_{dc} \sim 0$) and nonequilibrium (large I_{dc}) cases.

We use this knowledge of the electron system temperature to determine thermal conductance for cooling of the electron system. The total Joule power dissipated internal to the nanotube is $P_{NT} = I_{dc}^2 R_{int}$ and the thermal conductance can be found from $G_{th} = dP_{NT}/dT_e$. In Figure 5.3, we show G_{th} as a function of T_e for all four nanotube lengths

for $T_e > 20$ K, to avoid the ZBA. We find three different temperature regions. For $T_e < 120$ K and sufficiently short nanotubes, $\ell < 5 \mu\text{m}$, the dominant cooling path is out-diffusion of electrons into contacts; for longer nanotubes, the dominant cooling is instead into the substrate via emission of acoustic phonons. The thermal conductance between electron system and phonon system in the nanotube G_{e-ph} is predicted to scale at T^2 for low contact resistance. The nanotube-substrate phonon interface conductance G_{int} is predicted to scale linearly with T (Prasher 2005). For the longest length below 50 K, we find G_{ν} scales with T^2 and above 50 K, G_{ν} is proportional to T . Above 120 K, G_{th} increases rapidly with increasing temperature, approximately as T_e^5 . This is attributed to the emission of surface polar phonons directly into the SiO_2 substrate (Santavicca 2009, 2010). Thus, the thermal conductance G_{th} has experimentally been established for a single nanotube of different lengths as a function of temperature. We find that for a micron length individual metallic carbon nanotube, the low temperature thermal conductance is less than 1 nW/K, which is consistent with the order of magnitude estimates for the room temperature thermal conductance reported (Pop 2007).

Returning to Equation 5.1, we can now compute the expected bolometric response for a typical nanotube device at low bath temperature. The bolometric voltage detected is given by $\left(\frac{I_{dc}}{G_{th}} \frac{dR}{dT}\right) P_{abs}$. The dc bias current would be chosen to give a reasonable dR/dT while reducing G_{th} and minimizing R_{dc} so as to maximize the power transfer into the nanotube from the antenna. Examining Figure 5.1 shows that $I_{dc} = 1.5 \mu\text{A}$ is sufficient, with a corresponding $R_{dc} \approx 20 \text{ k}\Omega$, $dR/dT \approx 200 \Omega/\text{K}$, and from Figure 5.3 $G_{th} \approx 1 \text{ nW/K}$. The calculated maximum power delivered to our device from a bowtie antenna in our FTIR setup, as discussed in Chapter 4.4, is $\approx 1 \text{ nW}$; accounting for the impedance

mismatch of the nanotube presented in Figure 5.1 with the antenna gives the absorbed power in the nanotube as $P_{abs} \approx 12$ pW. Combining these gives the reasonable detectable bolometric output voltage as ~ 3 μ V. Thus, we would expect to be able to achieve sufficient electron heating due to weak THz radiation to allow bolometric detection in an individual single-walled carbon nanotube due to the very small thermal conductance.

5.4 Zero-Bias Anomaly

In the I - V characteristic of a typical carbon nanotube device we find a pronounced nonlinearity near zero bias, illustrated as a peak in the resistance (dip in the conductance) as shown earlier in Figure 2.2. This is known as a zero-bias anomaly (ZBA) and is common to quasi-metallic carbon nanotubes as well as point contacts and thin-film tunnel junctions. The ZBA only appears at low temperature and increases with decreasing temperature. As briefly described in Chapter 2, this feature is not yet well-understood and several possible interpretations have been put forward, including Luttinger Liquid effects, Coulomb blockade, or the presence of energy barriers at the metal-nanotube interface (Hunger 2004). At low temperature and low bias, few electrons are able to transmit through these energy barriers and the resistance increases, while at higher bias or temperature, the electrons possess enough energy to overcome any energy barrier present and the current increases so that the resistance decreases. This resistance change will tend to mostly modify the contact resistance beyond the quantum resistance, and be a measure of how well the nanotube is contacted by the metal electrodes. In the ZBA, these non-Ohmic ‘bad contacts’ strongly dominate the I - V characteristic and transport properties of the entire device, but not the internal inherent nanotube resistance.

The nonlinear transport behavior arising from the presence of a ZBA allows for nonlinear detection. As explained in section 5.2.2, the second current derivative of voltage can be used to predict the nonlinear mode detection. For a device exhibiting a strong ZBA, characterized by a large contact nonlinearity and considerable d^2V/dI^2 , one can expect significant THz detection at low bias and low temperatures. The explanation of the nanotube detection in this nonlinear mode due to the ZBA at THz is complex and claiming a complete understanding of this anomaly and the detection process would be inaccurate. We, however, present a feasible explanation based on the well-documented contact effects of the ZBA. We note that this is in contrast to bolometric detection, which is due to heating of the nanotube itself, namely the internal resistance and not that of contacts. For large contact resistances, the heating of electrons inside the nanotube may be very small and thus greatly reduce bolometric detection.

5.5 rf Detection

An intermediate step before proceeding towards THz measurements is to measure the response of an individual single-walled carbon nanotube due to an rf signal ~ 10 -100 MHz that is modulated on and off. This power modulation results in a measurable change in dc output voltage due to the detection mechanisms discussed and provides a good demonstration of the THz power that could be coupled. The measured voltage at the modulation frequency allows one to experimentally determine the device rf responsivity via the electrically controlled amount of power P_{rf} delivered to the device. For this rf measurement, we use both a dc bias and rf signal fed to the nanotube device through a

bias tee. Initially, we utilized a heterodyne measurement scheme with two rf inputs at ≈ 90 MHz and ≈ 100 MHz and the output at the difference frequency (≈ 10 MHz) was measured on a spectrum analyzer. Later measurements used an rf signal from a function generator modulated from zero to maximum amplitude at 400 Hz. The device was connected to a lock-in amplifier whose reference signal is synced with the 400 Hz modulating frequency of the rf pulse. Thus, any voltage measured is in direct response to the incoming rf signal. The ‘detected’ lock-in voltage was recorded for several rf frequencies and powers, as well as device temperatures and bias voltages. The ratio of the detected voltage ΔV to the rf power gives the voltage responsivity:

$$S_V = \frac{\Delta V}{P_{rf}} = \frac{V_{ON} - V_{OFF}}{P_{rf}} \quad (5.3)$$

Indeed we find two different response mechanisms when looking at the voltage response as a function of bias current (Santavicca 2009, 2011). The red curves of Figure 5.4 represents our measured data on the detection of rf (≈ 100 MHz) electromagnetic radiation by the same individual single-walled carbon nanotube sample discussed above, NT-1. The contacts for this sample were not designed for high-frequency rf or microwave measurements, limiting the accessible frequencies for investigation. We show that the intrinsic voltage responsivity from these rf heterodyne mixing measurements reveals both bolometric and nonlinear detection in two different regimes. At higher bias current, bolometric detection based on the dR/dT from the temperature dependent dc resistance and the G_{th} as described earlier fits the data very well, as shown in Figure 5.4. For $|I_{dc}| \geq 0.4 \mu\text{A}$, the rf detection at bath temperature $T_b \approx 4.2$ K is due to photon heating of the temperature-dependent resistance. At lower bias current, $|I_{dc}| < 0.4 \mu\text{A}$, a nonlinear

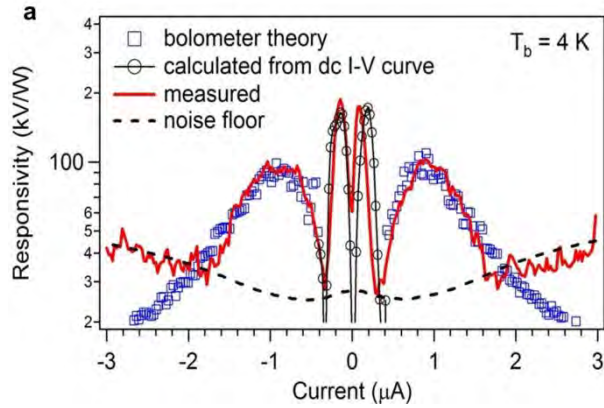
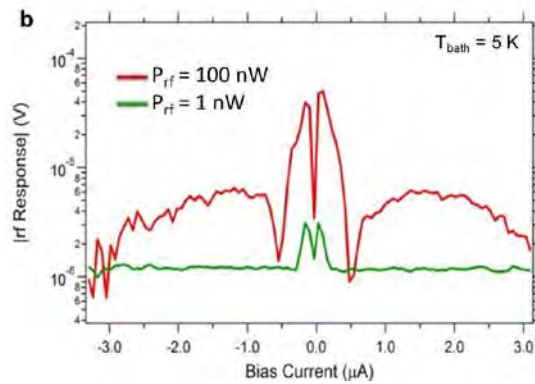


Figure 5.4 – (a) Intrinsic voltage responsivity from rf heterodyne mixing measurement at a bath temperature of 4.2 K for NT-1, a 5 μm single-walled carbon nanotube section with rf input power of 10 nW. The measured data is fit with the calculated bolometric responsivity as a function of bias current for $|I_{\text{dc}}| \geq 0.4 \mu\text{A}$ and with the calculated nonlinear responsivity from the dc I - V curve for $|I_{\text{dc}}| < 0.4 \mu\text{A}$. The experimental noise floor is also shown (Santavica 2011).



(b) rf voltage response for rf input powers of 100 nW and 1 nW for a device possessing larger contact resistance. At the lower input power, the bolometric detection at higher bias current is no longer observed.

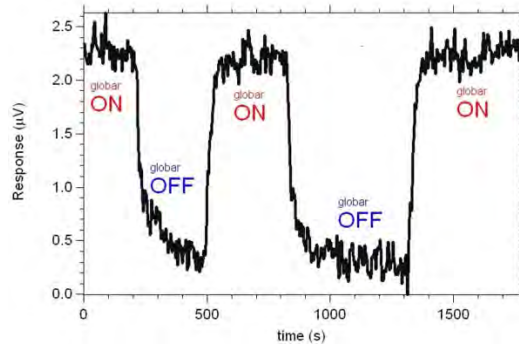


Figure 5.5 – THz response measured by lock-in amplifier at the chopping wheel reference frequency as a function of time for the hot globar blackbody source on/hot and off/cooling.

response corresponding to a non-ohmic ZBA contact characteristic of the dc I - V curve. The heating effect is negligible at these small currents. At $T_b = 77$ K, only bolometric detection is observed. The relative contribution of these two mechanisms depends on bias current, temperature and frequency. These rf experiments used a single-walled carbon nanotube with extremely small contact resistance, $R_c \approx 1$ k Ω . However, one thing to note with these rf measurements is that we can arbitrarily increase the power, which is not the case with our THz source. For the measurement at $T_b \approx 4.2$ K, the rf power was ≈ 10 nW, while at $T_b \approx 77$ K, it was ≈ 100 nW. Several other samples studied possessing larger contact resistances showed similar behavior for large input power, as shown in Figure 5.4b. For these samples at reduced input rf power ~ 1 nW, a better representation of the likely THz power that would be received by the nanotube, the device response is greatly reduced; only the nonlinear detection is often above the noise, and the bolometric response is too small to be observed. This may be due to these devices where the voltage drop across internal part of nanotube, R_{int} , is very small compared to contact resistance, R_c . Thus, it may be hard to experimentally detect bolometric response at THz with the limited coupled power available for samples with large contact resistance. However, the C_c in parallel to R_c may allow for THz current to shunt R_c and produce bolometric detection.

5.6 THz Detection

The principle behind the experimental setup for THz detection is similar to that for rf measurements. Initially, devices receive broadband THz power and the difference in

voltage between the THz signal was modulated by moving the wheel from transmitting hot ($T \approx 650$ K) to cold ($T \approx 250$ K). Figure 5.5 shows the signal modulation in phase with the chopping wheel for the two situations of the blackbody source on/hot and off/cold. The experimental setup is more complex than at rf due to difficulties and limitations when dealing with THz signals. Coupling the THz radiation to the nanotube device required techniques as described in the previous chapter.

The differential resistance dV/dI for samples denoted as NT-2 and NT-3 is presented in Figure 5.6 as a function of the dc current and bath temperature T_b . The left side of Figure 3.8 shows an SEM image of a sample similar to NT-2. Samples NT-1 and NT-2 displayed a significant gate dependence; data shown for these samples were taken with the device in its high conducting state with a gate voltage of -30 V and -6 V, respectively. The conductance of sample NT-3 displayed only a weak dependence on side-gate voltage, which may result in part from shielding of the gate by the electrodes. All data for sample NT-3 were taken with a side-gate voltage of either 0 or -1 V. At low temperature, all devices show a ZBA peak in dV/dI at zero bias current due to the imperfect transparency of the contacts. At higher currents dV/dI is approximately independent of current for samples NT-2 and NT-3. Sample NT-3 has the largest resistance and the most pronounced ZBA feature, whereas sample NT-2 has more moderate values. As discussed above, sample NT-1, on the doped Si substrate, showed a small ZBA peak, ≈ 2 k Ω at $T_b = 4.2$ K. Only sample NT-1 has small contact resistance, less than the quantum resistance R_Q , but this sample was not suitable for THz detection, as the doped substrate strongly absorbs THz. Sample NT-1, with length $\ell = 5$ μm , had total internal dc resistance of $R_{int} = 5$ k Ω at $T_b = 4.2$ K; we expect that the other two

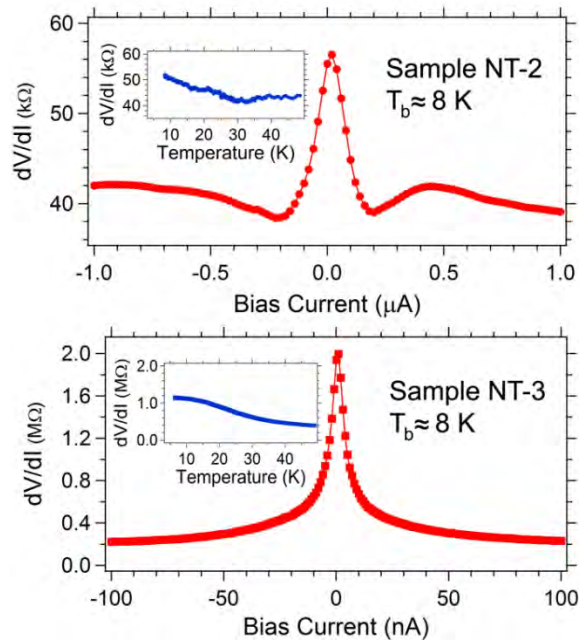


Figure 5.6 – Differential resistance as a function of dc bias current at $T_b \approx 8$ K for samples NT-2 and NT-3. The increase in dV/dI around zero bias current is referred to as a zero-bias anomaly (ZBA). (insets) Differential resistance as a function of bath temperature for respective samples measured with (top) 10 nA ac and 50 nA dc bias current and (bottom) 1 nA ac and 3 nA dc bias current.

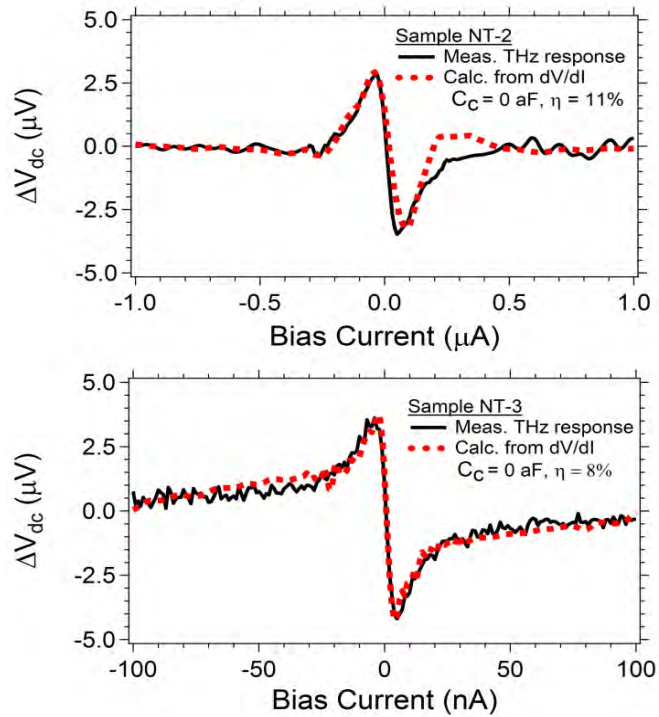


Figure 5.7 – Measured voltage change due to chopped THz source of samples NT-2 and NT-3 plotted against that calculated from Equation 5.2 using the measured low-frequency $I-V$ curve and the specified optical coupling efficiency η , for contact capacitance $C_c = 0$.

samples have internal dc resistances that are small compared to their other circuit dc resistances. We therefore define R_c in the transmission line model illustrated in Figure 2.4 to be $2R_c = dV/dI - R_q - R_{int}$, where $R_{int} = r_{int} \ell$, with r_{int} the internal resistance per unit length.

We use an audio frequency lock-in amplifier to measure the low-frequency voltage change due to the modulation of the incident THz power at the chopping frequency ≈ 100 Hz. At dc and audio frequencies, the sample is biased with a dc current. The high-frequency response due to the non-Ohmic ZBA contact nonlinearity arises from the second-order term of the Taylor series expansion of the I - V curve as explained above. The dc voltage change when chopping between the two THz blackbody sources (hot 650 K and cold 250 K wheel) is proportional to the second derivative of the I - V curve and, assuming the I - V curve at THz is the same as at the audio frequency which dV/dI is measured, is given by Equation 5.2 as

$$\Delta V_{dc} = (1/2) \Delta \langle I_{THz}^2 \rangle d^2V/dI^2 .$$

The change in the mean-squared THz current, $\Delta \langle I_{THz}^2 \rangle$, is computed from the equivalent RC circuit shown in Figure 2.4 using ΔV_{THz} obtained from Equation 4.1. We use AWR Microwave Office software to include the transmission line in the calculation. We plot in Figure 5.7 the measured and predicted results for ΔV_{dc} , first assuming that the contact capacitance $C_c = 0$ and treating power coupling efficiency of the optical system η as an adjustable parameter that provides an overall scale factor for optimal curve agreement at low currents. For both samples NT-2 and NT-3, the inferred value of η from this fitting is reasonable, with $\eta = 11\%$ and 8% , respectively. The good agreement with theory is evident.

We now consider the possible contribution to the measured THz response from bolometric detection. The dc voltage change due to bolometric detection, due to heating of the nanotube when chopping between the THz blackbody sources and neglecting electrothermal feedback, is given as above by Equation 5.1 with $\Delta V_{bolo} = I_{dc}(dR/dT)P_{abs}/G_{th}$. As described above, we estimate $G_{th} \sim 0.1$ nW/K per micron for samples NT-2 and NT-3. dR/dT is determined from the measured $R(T)$, shown in Figure 5.1. For sample NT-1, measured at ≈ 100 MHz and with its small $R_c < R_q$, the I - V contact nonlinearity response is found in the low current range, but for $|I_{dc}| \geq 0.4$ μ A, the bolometric (heating) response is dominant. For samples NT-2 and NT-3, if we assume $\eta = \eta_{max} = 15\%$, as explained in Chapter 4.4, we can determine the maximum possible bolometric response. We take $r_{int} = 1$ k Ω/μ m and we first consider the value of I_{dc} where we observe the greatest THz response. For sample NT-2 at $I_{dc} = 50$ nA, we compute $\Delta V_{bolo,max} \sim 50$ nV. Similarly, for sample NT-3 with $I_{dc} = 3$ nA, we predict $\Delta V_{bolo,max} \sim 0.2$ nV. These values are much smaller than the measured response as well as the calculated response from the contact nonlinearity, Equation 5.2. The bolometric response is expected to increase for larger bias currents, as described by Equation 5.1. However, for both samples NT-2 and NT-3, the device noise increases with increasing bias current, and we do not observe bolometric detection in the current range presently studied. Additionally, the above analysis assumes that all the absorbed THz power is dissipated in the R_{int} of the nanotube, with its associated G_{th} ; however, if the observed dR/dT is predominately due to the contacts and not internal to the nanotube, the power absorption by the comparatively large and thermally anchored contacts, with a larger G_{th} , may result in negligible heating and explain the apparent absence of bolometric response. We

conclude that bolometric detection was possible in sample NT-1 due to its low contact resistance, but this mechanism does not contribute significantly for the THz detection observed for higher resistance samples NT-2 and NT-3.

Most other devices showed similar behavior to that of NT-2 and NT-3, characterized by nonlinear detection at low bias current. However, there were two antenna-coupled single-walled carbon nanotube devices that did indeed show bolometric detection at low temperature, as shown in Figure 5.8, at higher currents for $|I_{dc}| \geq 0.5 \mu\text{A}$, but exhibited dramatically increased noise with increasing bias current. These devices showed significant Joule heating at larger bias current and may possess reduced contact resistances, but a means of determining such properties was not possible with the configuration of these devices. Measurements at rf with large input power of 100 nW and biased at various gate voltages, exhibited both nonlinear and bolometric detection. However, the dc voltage response at decreased input rf power of 1 nW, comparable to the THz power available in our FTIR setup, is decreased and the signal for bolometric detection is too low to detect, as displayed in Figure 5.4b. For all devices studied there was no successful THz detection of either the bolometric or nonlinear type at elevated bath temperature of 77 K.

In comparison, bundles of single-walled carbon nanotubes, possibly understood with a considerably different circuit model than that described in Chapter 2, have been studied by others. These exhibit a contact nonlinearity that gives rise to detection at microwave frequencies (Rodriguez-Morales 2006) and for a few devices at THz (Carrion 2009), but bolometric response appears to dominate for THz detection (Fu 2008, Carrion 2009). The bolometric mechanism is believed to dominate due to a large total contact

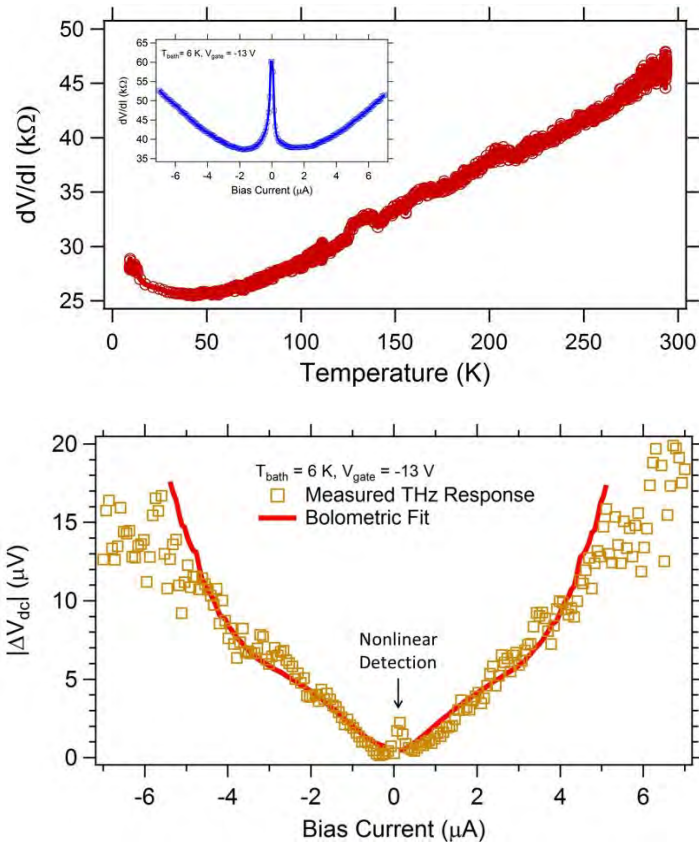


Figure 5.8 – (top) dc characteristics for a nanotube device NT-B showing differential resistance as a function of bath temperature measured with a bias current of 1 nA and gate voltage of -32 V. (inset) differential resistance as a function of dc bias current at a bath temperature of 6 K and gate voltage of -13 V. At larger bias current observe Joule heating and a significant ZBA around zero bias current. (Bottom) Measured THz voltage response as a function of bias current plotted against calculated bolometric detection from the device low-frequency characteristics, optical coupling efficiency η_{max} , and a $G_{th} = 0.4$ nW/K. The bolometric detection noise dramatically increases with increasing bias current. Nonlinear THz detection is also observed around zero bias.

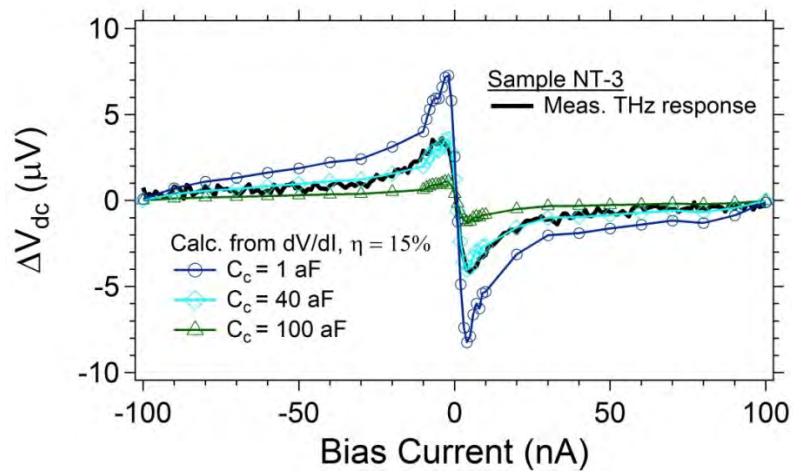


Figure 5.9 – Measured THz voltage response of sample NT-3 plotted against that calculated for nonlinear detection. The calculation uses the measured low-frequency I - V curve, the limiting case of maximum optical coupling efficiency η_{max} , $r_{int} = 1$ k Ω / μ m and various values of C_c in the transmission line circuit model of Figure 4.6. The data are best fit with $C_{c,max} \approx 40$ aF; the actual value is likely smaller.

capacitance, inferred for the bundle to be $\approx 1\text{-}10$ fF, effectively short circuiting the nonlinear contact resistance at THz frequencies, but not at microwave frequencies. We find that the THz detection mechanism of the individual single-walled carbon nanotubes ($R_c > 10$ k Ω) at low bias current arises from the nonlinear I - V curve due to non-Ohmic contacts, and the capacitance C_c does not short circuit R_c , and arises from bolometric detection at higher current for devices with small R_c .

5.6.1 THz Responsivity

A standard figure of merit for THz detectors is the voltage responsivity S_V , defined as the output voltage change divided by the input THz power, $S_V = \Delta V_{dc}/\Delta P_{THz}$ as in Equation 5.3. The internal responsivity S_{int} refers to the THz power coupled into the device, while the external responsivity S_{ext} refers to the available THz power (that which would be coupled into a matched load). S_{ext} is a more relevant quantity than S_{int} , as this is the responsivity that would be achieved in an actual application. We find for samples NT-2 and NT-3 $S_{int} \approx 2$ MV/W and 100 MV/W, respectively, for the maximum nonlinear response ($C_c = 0$). We compute $S_{ext} \approx 10$ kV/W and 15 kV/W for samples NT-2 and NT-3, respectively. We expect for sample NT-1, from the data measured at 100 MHz and assuming that capacitances of the circuit in Figure 2.4 would not limit the response, that $S_{ext} \approx 5$ kV/W for the maximum nonlinear response and ≈ 3 kV/W for the peak bolometric response. These are lower than the values found for samples NT-2 and NT-3 because the nonlinear contact resistance (the ZBA) of sample NT-1 is a much smaller fraction of the total resistance.

TABLE 5.1. Summary of low temperature sample characteristics. R_{ZBA} is the observed ZBA resistance increase around zero dc bias current. THz response due to the nonlinear I - V occurs at low current; bolometric response for sample NT-1 is observed for $|I_{dc}| \geq 0.4 \mu\text{A}$. $C_{c,max}$ is the maximum capacitance determined with a maximum coupling efficiency $\eta_{max} = 15\%$.

Sample	Length (μm)	Frequency	Observed THz Response		R_{ZBA} ($T_b = 4\text{K}$)	$C_{c,max}$ ($\eta = 15\%$)
			Bolometric	I-V nonlin.		
NT-1	5	100 MHz	Yes	Yes	2 k Ω	-
NT-2	1	0.5 THz	No	Yes	15 k Ω	70 aF
NT-3	4.5	0.5 THz	No	Yes	1.8 M Ω	40 aF
NT-B	4.5	0.5 THz	Yes	Yes	60 k Ω	-

5.7 Estimation of Contact Capacitance

The junction/contact capacitance of a nanotube device is important in determining its intrinsic maximum operating frequency. Measuring this value directly at high-frequency is challenging because the single-walled carbon nanotube impedance ($\gtrsim 10$ k Ω) is much greater than the instrument impedance (50 Ω). The effective circuit model for an individual single-walled carbon nanotube was studied in previous measurements of the microwave impedance (Plombon 2007, Nougaret 2010). These studies deduced a lumped-element capacitance between the full single-walled carbon nanotube and the metallic contacts of ≈ 1 -10 fF. This was compared to the lower predicted value of the single-walled carbon nanotube electrostatic capacitance by Burke (Burke 2002). However, the model of the electrostatic capacitance as a lumped element in parallel with the contact resistant is incorrect at THz frequency; the model described earlier, Figure 2.4, should instead be used. Studies of a single-walled carbon nanotube bundle at microwave and THz inferred a total contact capacitance with a similar value ≈ 1 -10 fF (Fu 2008, Carrion 2009) which would limit THz applications.

However, other measurements of C_c include dc measurements of individual semiconducting single-walled carbon nanotubes in the quantum dot regime, inferring $C_c \approx 15$ aF (Park 2001); Yoneya *et al.* estimate 1 aF for multi-walled nanotube islands (Yoneya 2001); Postma *et al.* posit a value of 0.3 aF in a carbon nanotube single-electron transistor (Postma 2001); Tarkiainen *et al.* extract values from 31-111 aF for tunnel junctions from metallic leads to metallic nanotubes (Tarkiainen 2001); Sapmaz *et al.* extracted a value of 1-3 aF for source and drain capacitances on chrome-gold contacted nanotubes (Sapmaz 2006); microwave rectification measurements of a CNT Schottky

diode estimating C_c in the aF range (Cobas 2008); and Tseng and Bokor fabricated back-gated nanotube-Schottky diode devices inferring values of parasitic capacitances and $C_c \approx 5\text{-}27$ aF (Tseng 2010). The small size of the junction and parasitic capacitances, coupled with device resistance of $10\text{ k}\Omega$, implies intrinsic cut-off frequencies in the THz range for carbon nanotube devices.

Comparing the magnitude of the measured nonlinear THz response of our individual single-walled carbon nanotube devices ($R_c > 10\text{ k}\Omega$) to the calculated response based on the measured low frequency I - V curve, we are able to place an upper bound on the magnitude of C_c . This bound is smaller than the previous high-frequency experimental estimates mentioned above and consistent with other studies finding C_c in the aF range. We consider the effect of the contact capacitance C_c between the metal electrodes and the single-walled nanotube in the transmission line circuit model of Figure 4.6. Including C_c will reduce the THz voltage and the value of ΔV_{dc} given by nonlinear detection of Equation 5.2, but does not change the overall shape of ΔV_{dc} vs. I_{dc} seen in Figure 5.7. We consider, for example, sample NT-2, where we are able to fit the measured response for $C_c = 0$ with $\eta = 11\%$. If we now consider the limiting case of $\eta_{\max} = 15\%$ and $r_{int} = 1\text{ k}\Omega$, the data are best fit with $C_{c,\max} \approx 70$ aF. Similarly, for sample NT-3, as shown in Figure 5.9, $C_{c,\max} \approx 40$ aF. These values are the maximum allowed by our model calculation and hence represent an upper bound on C_c ; the actual value is likely smaller.

5.8 Summary

We have studied the high frequency response of individual carbon nanotubes and find detection at low temperature as a result of a bolometric effect at higher bias current and due to a contact nonlinearity at lower bias current. For nonlinear detection, we conclude that the contact capacitance does not strongly limit the THz performance. With the identified THz detection by an antenna-coupled individual carbon nanotube we can now incorporate this with the Fourier Transform Infrared Spectrometer results described in Chapter 4 to measure the spectral response of the nanotube device. The spectral response is predicted to exhibit THz standing wave resonances on the finite length nanotube. As discussed in the next chapter, this can reveal the plasmon propagation velocity and related Luttinger parameter for the single nanotube and provide a signature of the electron-electron interaction within this 1D system.

Chapter 6

Terahertz Spectral Response of Individual Single-Walled Carbon Nanotubes

6.1 Introduction

A hallmark of the correlated behavior of electrons when confined to one dimension (1D) as predicted by the Luttinger liquid model is the phenomenon of spin-charge separation. In this, the low-energy excitations of a 1D system are charge and spin modes that propagate with independent velocities (Burke 2002, Desphande 2010). The direct experimental observation and verification of this phenomenon has been the subject of many research efforts, as described in Chapter 2. For the case of an individual single-walled carbon nanotube treated as a nanotransmission line, the collective bosonic waves are expected to separate into a charge plasmon wave traveling at a speed faster than the Fermi velocity and three neutral modes that propagate at the Fermi velocity. Standing wave resonances formed by coupling terahertz radiation to the plasmon mode within a micron-length carbon nanotube allow for the measurement of the plasmon propagation velocity and verification of this model. Combining the high-frequency model depicted in Chapter 2 with the samples fabricated using the techniques described in Chapter 3 within

the measurement setup detailed in Chapter 4 and utilizing the detection scheme explained in Chapter 5, we probe a signature of the electron-electron interaction within this 1D system.

6.2 Background Spectral Response

In order to extract the 1D behavior of the carbon nanotube itself and remove possible contributions from the antenna or FTIR optical system, we must determine the background spectral response of the entire system without the nanotube. We do so by measuring the device voltage response of an impedance-matched, antenna-coupled broadband Nb bolometer as a function of mirror displacement within our FTIR setup. This produces an interferogram which is Fourier-transformed to yield the spectral response, as explained in Chapter 4. Since the Nb microbridge response itself is approximately frequency independent, this spectrum reflects the response of our optical THz measurement system and the chosen antenna geometry. The typical spectrum for the bowtie and log-spiral antennas studied follow a sharp increase and gradual peak, followed by a slow decay with increasing frequency, as shown in Figure 4.3. The bowtie frequency response is narrower. For an individual single-walled nanotube in place of the Nb microbridge within the FTIR system, we expect to find features corresponding to standing wave resonances on top of the system background response. Using the measured antenna background response for a log-spiral antenna in our system, we can construct the predicted normalized response of the antenna-coupled nanotube, as shown in Figure 6.1 for the case of a 1 micron long nanotube with an assumed Luttinger parameter $g = 0.65$.

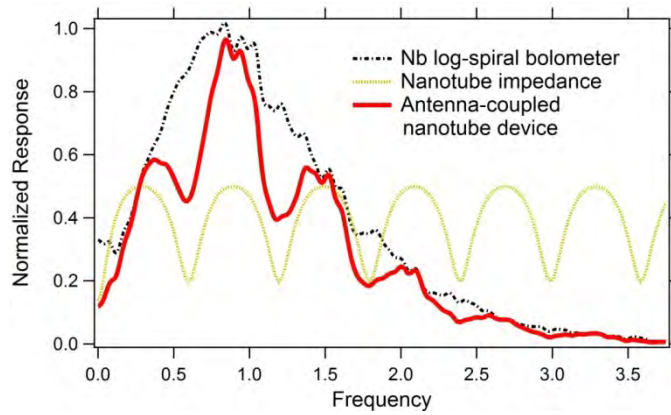


Figure 6.1 – The measured log-spiral antenna response combined with the calculated nanotube impedance/current resonance yields the predicted response of a 1 micron long antenna-coupled single-walled carbon nanotube device in a log-spiral antenna geometry for a Luttinger parameter $g = 0.87$.

The location of these features in the frequency domain and their separation reveal the propagation velocity of a plasmon wave and the related g value.

6.3 Carbon Nanotube Device Interferogram

We exploit the nonlinear THz detection mechanism in the FTIR system described in the previous chapter to obtain an interferogram of a nanotube. Initially it would seem biasing the antenna-coupled nanotube device at the conditions that give maximum THz detection is best; however, a major challenge with attempting to obtain an interferogram of an antenna-coupled carbon nanotube device is device noise, which can change with bias conditions. The THz signal which produces the interferogram displays very small variations as a function of mirror displacement. The bias conditions producing maximum detection can increase the magnitude of the voltage detected but often also lead to decreased noise performance. There are significant fluctuations around an average detected voltage value which conceal the variations due to the mirror displacement we seek to determine. Thus, an optimization approach which maximizes detection while reducing noise is critical. Once an optimum bias is determined, we employ considerable averaging, low scan rate, and long scan times to enhance the detectable interferogram signal.

6.3.1 Noise in Carbon Nanotubes

All electronic and optical devices possess random fluctuations, known as noise, in their output electrical signal. Many types of electric noise are known to exist for a wide range

of physical systems. Their origins vary, but the result is substantial fluctuations in resistance or device THz response. Common categories of noise are Johnson noise, shot noise, flicker noise, and random telegraph signal noise. Johnson noise is thermal in origin and results from the thermal distribution of charge carrier velocities and was briefly discussed in the previous chapter. Shot noise is due to the discrete electrical charge and is produced by statistical current fluctuations across a junction. Flicker noise, or $1/f$ noise, is a low frequency phenomenon where the noise power spectrum obeys an inverse frequency power law. Flicker noise occurs in nearly all electronic devices, and a universal physical cause has yet to be identified. Random telegraph noise, also known as burst or bi-stable noise, describes a situation where a sudden step-like transition switching occurs between two discrete system states.

Small 1D systems are predicted to be exceptionally noisy (Staliunas 2001). Noise in single-walled carbon nanotubes has been investigated by several groups. It has been reported that nanotubes exhibit anomalously large bias-dependent $1/f$ noise (Collins 2000). The observed noise magnitude reported is significant when compared to devices with similar resistances and can be ten orders of magnitude larger than the noise observed in conventional conductors. Typical sources of noise in metals are electromigration or defect propagation. However, for covalently bonded system, such as a carbon nanotubes, one might expect that the lattice ions are immobile and any structural fluctuations of lattice defects possess large characteristic energies, precluding this source of noise (Vitusevich 2011). Conversely, due to small nanometer-sized nanotube structure, all the atoms in the system constitute surface atoms. Any surface fluctuations of an individual atom, even though seemingly minor, will have significant contribution to the overall

noise. In addition to these intrinsic noise sources, there are several extrinsic noise mechanisms which may contribute to the large observed noise in carbon nanotubes. Any external source that can affect the sensitive one-dimensional flow of current by interacting with even a single nanotube atom will greatly contribute to the observed noise. There can be random tunneling electron fluctuations at the electrical barriers formed at the metal-nanotube contacts. Any surface adsorbents or contaminants on the lattice surface may greatly affect the nanotube electronic behavior and also add to the generation of noise (Ulbricht 2009). The motion of charged defects residing in nearby dielectrics, such as the substrate or electron tunneling into the nanotube at the dielectric/nanotube interface or from surface contaminants, can also act as significant noise sources (Tobias 2007). Trapped charges in the substrate result in substantial noise for graphene devices. Water molecules have been identified as sources of long-range impurity scattering in graphene (Kaverzin 2012). Furthermore, the noise spectrum has been seen to increase as a function of carrier concentration or carrier mobility for carbon nanotubes (Gasparyan 2010, Sydoruk 2014). The noise in carbon nanotube devices is observed to increase dramatically with bias conditions, such as bias current and gate voltage. Measurements on the spatial dependence of the electron energy distribution in carbon nanotubes found that the diffusive transport in a 1 micron long nanotube is due to ~3-6 defects along the length, which produce elastic scattering. Local inelastic scattering was found to be able to be turned “on” and “off” for different gate voltage values (Bronn 2013). The gate voltages at which the most inelastic scattering occurs are at seemingly irregular values, which explains the behavior we observe in Figure 6.2 where nanotube THz detection is maximum at random values.

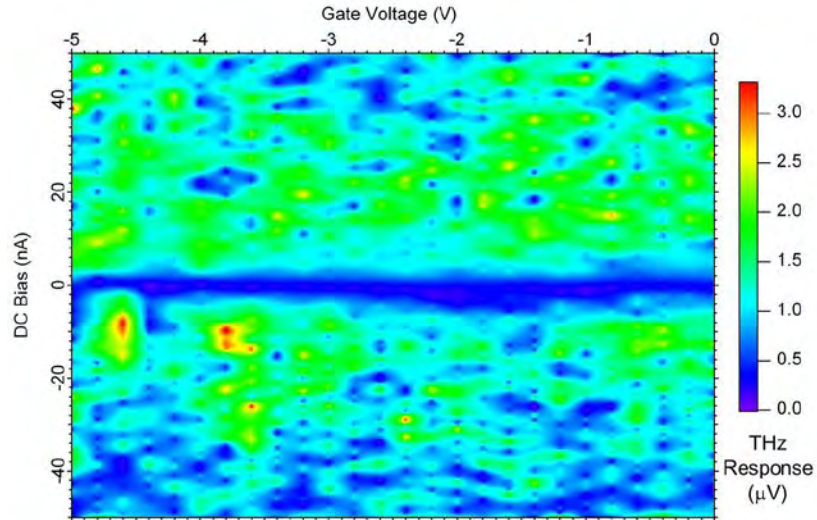


Figure 6.2 – Contour plot of device response to find bias conditions which maximize detected THz response. The conditions producing maximal detection can be at seemingly irregular values of dc bias current and applied gate voltage.

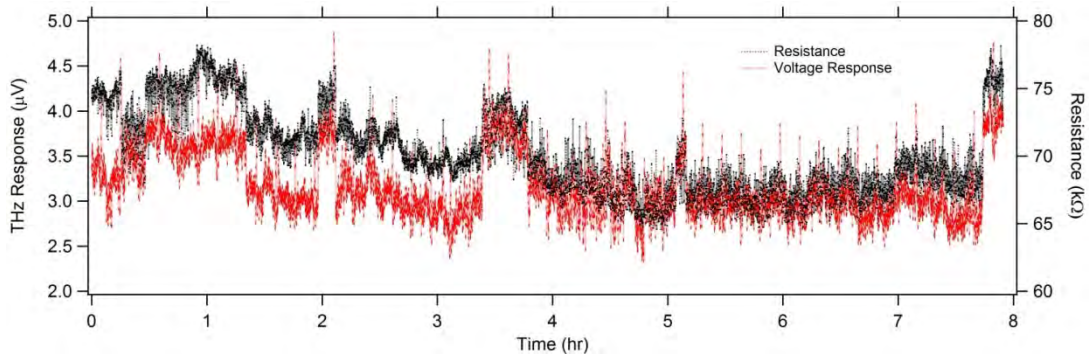
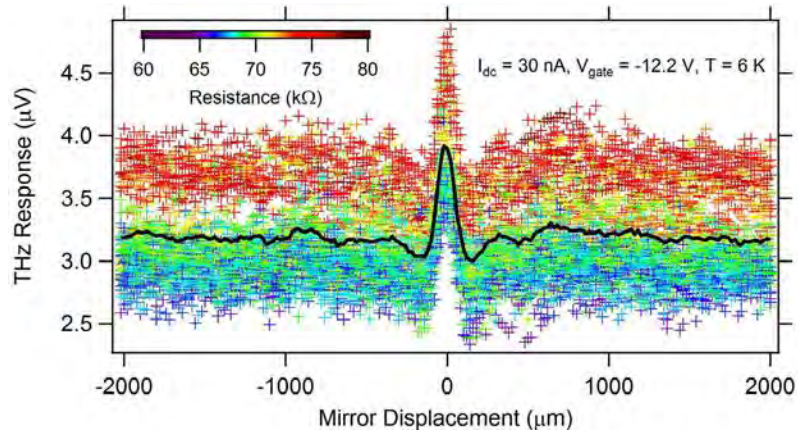


Figure 6.3 – Individual and averaged interferograms for an antenna-coupled single-walled carbon nanotube device (top) as a function of mirror displacement and (bottom) as a function of time showing the variation in THz response and resistance.

Physical mechanisms to fully explain the varied observed noise in carbon nanotubes have yet to be determined. Nevertheless, this fact presents a significant experimental challenge when measuring small signals in such noisy devices. Reproducibility of any given nanotube device is generally difficult and an inherent challenge since small uncontrollable and unnoticeable changes to the nanotube or nanotube environment can have significant contributions to its electrical behavior and thus THz detection. In the current work, we locate the optimum biasing conditions of gate voltage, bias current and temperature to maximize the THz signal above the noise present in our antenna-coupled nanotube devices. However, this can often also lead to increased device resistances and decreased THz coupling. We measure and average many interferograms to reduce the noise. However, other issues during the long time required for each interferogram measurement can complicate the results of this averaging. This includes drift in temperature as well as telegraph noise in the device resistance and detected THz signal at fixed bias conditions. Figures 6.2 and 6.3 show the optimum biasing scheme and the change over time for a typical antenna-coupled nanotube device.

6.4 Expected Response

Combining the spectral response for a bowtie antenna, shown in the inset of Figure 4.3, with the calculated response for a low resistance nanotube device as shown in Figure 2.5, yields the “expected” spectral response shown in Figure 6.1. These periodic features, i.e., the dips in response, deviating from the antenna and optical system spectral background correspond to predicted standing-wave resonances along the finite-length nanotube. Each dip corresponds to a maxima in the input impedance or, equivalently,

minima in the THz current through the contact resistance. As shown in Chapter 2, the ratio of the contact resistance R_c to characteristic impedance Z_{char} can noticeably change the shape of these periodic resonances. Namely, for $R_c < Z_{char}$ input impedance minima occur at integral multiples of a half wavelength and input impedance maxima occur at odd multiples of a quarter wavelength. For $R_c > Z_{char}$, the reverse is true, where the input impedance maxima occur at half wavelengths and input impedance minima occur at odd multiples of a quarter wavelength. For true real-world devices, R_c can have a large range of values, which is especially relevant when detecting using the nonlinear detection of the ZBA at low bias. For the devices discussed in this chapter we are in the $R_c > Z_{char}$ limit. Thus, since the variation in input impedance will modify the power transmission into the nanotube and the THz current that flows through the nonlinear junction, we expect maximum power coupling for our devices at quarter wavelength and minimum power coupling at half wavelength. The spectral responses are analyzed by attempting to identify these minima of power coupling or current flow, characterized as a dip in the spectral response. The frequency location of such a feature or the spacing of repetitive dips yields the frequency spacing $\Delta f = \frac{v_F}{2Lg}$ which can thus reveal g through knowledge of the length of the nanotube device and the known Fermi velocity is $v_F = 8 \times 10^5$ m/s (Zhong 2008). For the calculated response shown in Figure 6.1, the frequency spacing of 0.6 THz for the 1 micron long nanotube with $R_c < Z_{char}$, gives a g value of 0.65.

The equivalent circuit model used to represent the antenna as a voltage source can influence the expected resonance behavior within the nanotube. The THz voltage has an impedance equal to that of the antenna ($\approx 100 \Omega$) which is much less than the nanotube resistance ($> 10 \text{ k}\Omega$), so it approximates a voltage source. As shown in the insets of Figure

6.4, treating the antenna as an antisymmetric or as a symmetric voltage source and the relative ratio of the potentially unequal contact resistances on each end of the nanotube will affect the input impedance of the nanotube, and thus THz coupling into the nanotube, as well as the THz current flowing through each contact resistance, the source of the nonlinear detection. Figure 6.4 depicts simulations using AWR Microwave Office for contact resistances greater than the characteristic impedance for four different symmetric and asymmetric cases of voltage source and contact resistance. For the asymmetric voltage case, with a single THz voltage source of value V , we find the expected resonant structure introduced earlier. This is characterized by features in the current at integral multiples of half wavelength with an altered THz current passing through each contact resistance. The ratio of the THz current magnitudes increases for asymmetric contact resistances. For the symmetric voltage source case, we consider two voltage sources on opposing sides of the nanotube, one positive $V/2$ and the other negative $-V/2$, each exciting half of the THz voltage to the nanotube. When the contact resistances on each side of the nanotube are equal, the currents through each contact resistance are equal and the resonances only occur for *odd* multiples of half wavelength, rather than all multiples of half wavelength for the symmetric case. Based on the dc resistance measurements of the devices at positive and negative dc current bias, we observe that there are often slight differences in the resistance based on current direction (Figure 5.6), which would indicate imbalance in the two contact resistances. For increasingly unequal contact resistances, the resonance behavior at even multiples of half wavelength reappears. Nonlinear THz detection senses the THz current that passes through the contact resistances. The resonant behavior in the THz current will manifest itself as dips in the spectral response.

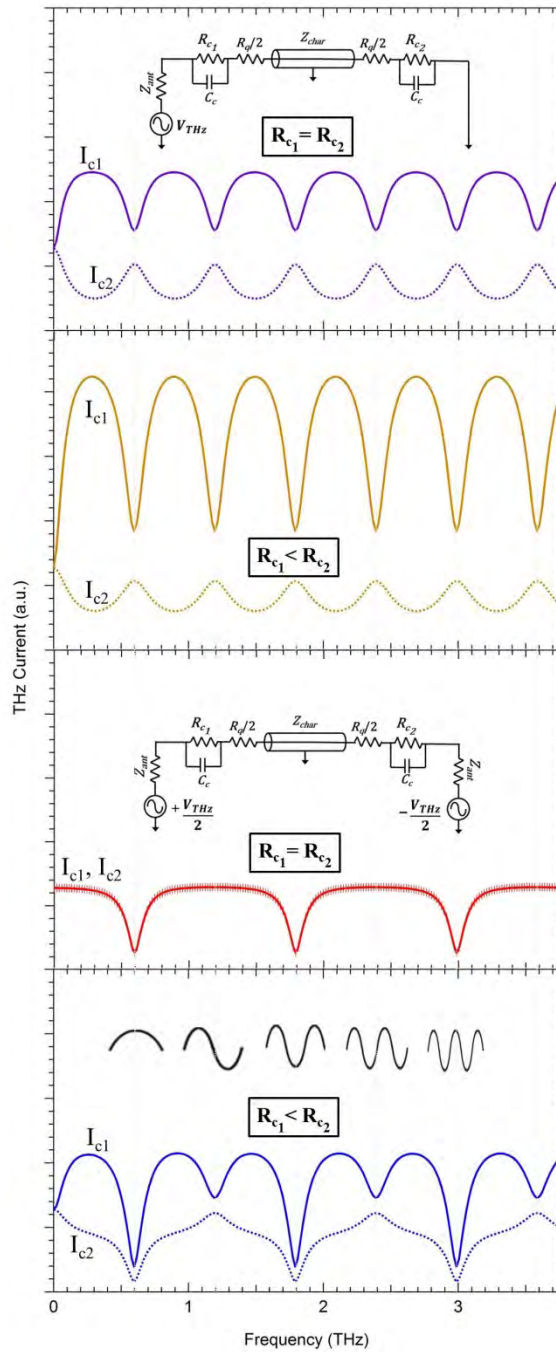


Figure 6.4 – Simulation of the THz current as a function of frequency flowing through equal or unequal contact resistances of a carbon nanotube transmission line model with treatment of the antenna as an antisymmetric or a symmetric voltage source. The ratio of the contact resistances modifies the input impedance of the nanotube affecting the THz coupling into the nanotube as well as the THz current flowing through each contact resistance and thus THz response. The contact resistances are greater than the characteristic impedance of the nanotube and the shapes of the resonances are shown in the fourth panel. Features in the THz current are found for integral multiples of half-wavelength except for the case of symmetric voltage source and equal contact resistances.

6.4.1 Spectral Response Results

The dc properties and THz response as a function of bias current at low temperature for sample NT-2, a ≈ 0.9 micron long bowtie antenna-coupled individual single-walled carbon nanotube, were introduced in Chapter 5. Using a bias current of 100 nA within the ZBA for nonlinear detection and a gate voltage $V_{gate} = -5$ V, we measure an interferogram at low temperature as shown in Figure 6.5. In addition to the average result of ~ 100 scans, we also plot each individual data point during each scan to show the variation. Figure 6.5 shows the normalized spectral response achieved from a zero-padded Fourier transform of the scan average, as well as the standard deviation for each frequency data point from the collection of scans. As discussed above, nanotubes possess much intrinsic noise, as seen in the variation from scan to scan, so many averages of individual scans are required to obtain a reasonable interferogram. However, a drawback of this approach is that the nanotube may have drifts or shifts in electrical behavior/properties during these long scan runs, as shown earlier in Figure 6.3 for a different device. Initially the device may be biased at high detection conditions, but these may then transition to conditions providing poor detection. Several other interferograms of NT-2 were taken at differing bias conditions and exhibited the same behavior. Figure 6.5 shows that there is a prominent dip in the spectral response at $f \approx 0.6$ THz when compared to the expected background response of the bowtie antenna and optical system, as described in Chapter 4. This dip in response corresponds to a half-wavelength resonance on this carbon nanotube with high-resistance contacts, resulting in a larger input impedance and decreased coupling to the nanotube at this frequency and decreased THz current through the

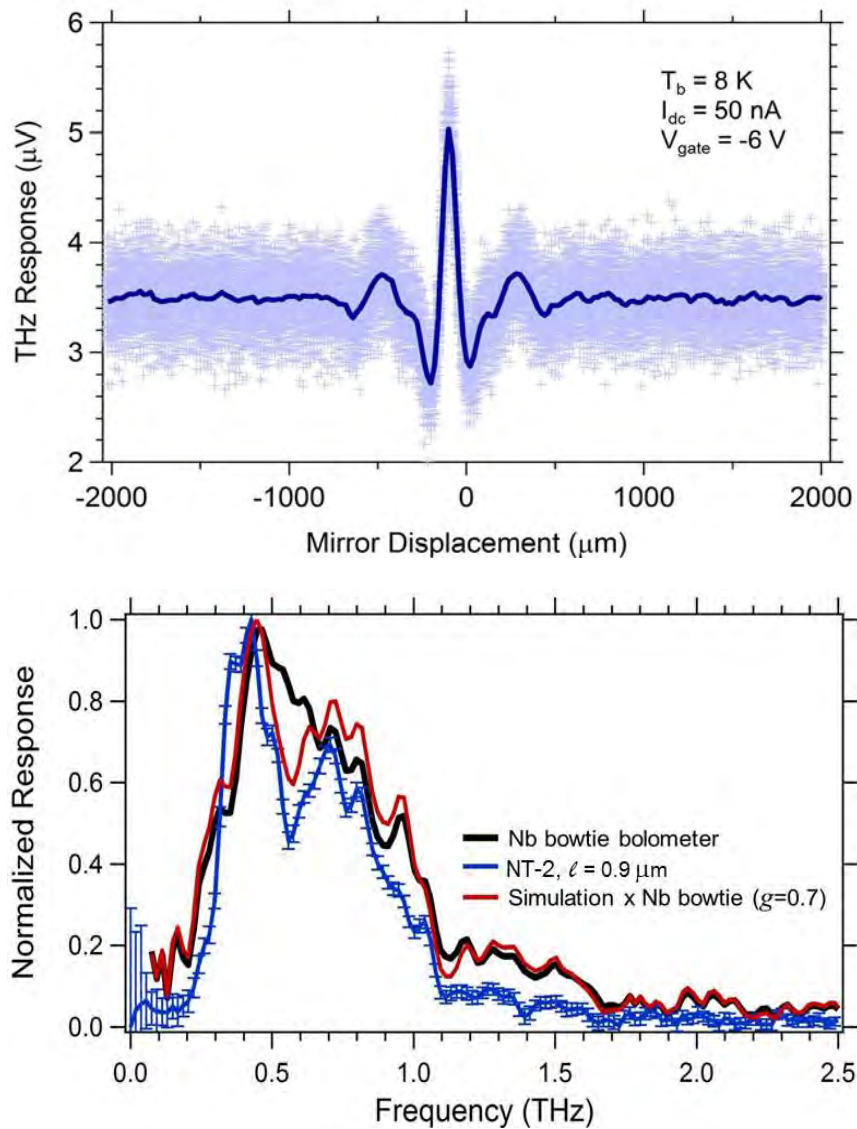


Figure 6.5 – Interferogram and spectral response of a ≈ 0.9 micron antenna-coupled single-walled carbon nanotube device denoted as sample NT-2 including the individual interferogram scan variation and standard deviation of the spectral response. The background spectral response of the optical system due to a superconducting Nb microbridge bolometer with a bowtie antenna geometry is also shown. In addition, a simulation of the nanotube response for a Luttinger parameter $g \approx 0.7$ multiplying the Nb response is plotted. A prominent feature in the nanotube spectral response is observed at a frequency of ≈ 0.6 THz and is interpreted as corresponding to a half-wavelength resonance on the nanotube with high-resistance contacts.

nanotube ZBA. The location of this dip in frequency is robust and the several measurements at different biasing conditions show the same dip behavior as shown in Figure 6.5. Using this measured value of $f_1 \approx 0.6$ THz as the first resonance in the frequency spacing equation $\Delta f = \frac{v_F}{2Lg}$ from Chapter 2, with the nanotube length of ≈ 0.9 micron obtained with SEM imaging, yields a $g \approx 0.7$. This corresponds to a propagation velocity $v_p \approx 1.1 \times 10^6$ m/s.

We have performed simulations using AWR Microwave Office treating the nanotube as a transmission line with the characteristic values of resistance, kinetic inductance, etc. as described in Chapter 2, using the effective total capacitance per unit length of the transmission line as the fitting parameter. We can determine the total capacitance per unit length value which will produce an impedance maximum at $f \approx 0.55$ THz. This C_{tot} can then be inserted into the equation from Chapter 2 $g = \sqrt{\frac{C_{tot}}{4C_Q}}$ to determine the corresponding g value. We can also multiply the results of this simulation, which assumes equal contact resistances and symmetric antenna voltage source, with the normalized spectral response and plot it together with measured spectral response as the red narrow line in Figure 6.5. We find good agreement between the measured THz response data and simulation with a value of $C_{tot} \approx 200$ aF/ μm . We also find a $g \approx 0.7$ in agreement with above. We note that these simulations of the circuit diagram described earlier do not explicitly include effects from the gate electrode which would presumably affect the capacitance value.

The limited bandwidth of the bowtie antenna and optical system does not allow us to observe any of the higher order resonances, which would be expected to also occur at

1.2 THz (full wavelength), 1.8 THz (three-halves wavelength), etc, which are beyond this bowtie antenna's present bandwidth. However, as explained in section 6.4, using the symmetric voltage source model and assuming approximately equal contact resistances, we would not expect to observe the full wavelength resonance at 1.2 THz. We thus want to measure samples that are longer, resulting in smaller frequency spacing between resonances, and also other antenna geometries which would present greater bandwidth. However, longer nanotube samples are more resistive and are likely to have greater complexity of the response due a larger probability of possessing defects or contamination in addition to increased intrinsic noise.

We have measured several other individual single-walled carbon nanotube samples of varying length and electrical properties using their nonlinear THz detection. The results of these measurements can be classified into five general categories:

1. samples exhibiting a feature in the spectral response (as observed in NT-2) corresponding to a detectable resonance on the nanotube corresponding to a Luttinger parameter g value of ≈ 0.7
2. samples which showed a feature in the spectral response corresponding to a $g \approx 1$ (sample NT-6)
3. a few samples which showed a feature in the spectral response corresponding to a $g \approx 0.3$ (sample NT-7)
4. samples producing interferograms which generate spectra that are too noisy to reliably determine any reproducible resonant features (sample NT-3)
5. samples which did not show any feature in the spectral response, possibly due to very small signal from the resonances (sample NT-8 in Figure 6.10)

perhaps due to a large carbon nanotube internal resistance that damps out resonances

6. samples which did not produce a well-defined interferogram (i.e., no central peak) despite reasonable nonlinear detection

We next briefly discuss a representative sample for several of these categories. Table 6.1 highlights the relevant properties and measured and simulated values for several of the devices studied.

A second sample measured that falls into the first category is comparable in length to NT-2, measuring ≈ 1.1 micron long. This sample is at the center of a bowtie antenna with a sidegate and shows similar behavior with a dip ≈ 0.6 THz, as in Figure 6.6. This dip, or drop in THz current through the contact resistance, is observed in this sample, denoted NT-4; this corresponds to a $g \approx 0.65$. Furthermore, this exact same sample has been measured in a similar FTIR system at the University of North Florida in the lab of Prof. Daniel Santavicca that also shows a dip in the spectral response at a frequency of ≈ 0.6 THz, as shown in Figure 6.6. The fact that this sample can reproduce the same behavior after a long period of time in a separate FTIR measurement is a very strong indication of the intrinsic nature of this behavior. A second feature is not clearly found at 1.2 THz, which may again be an indicator that contact resistances are nearly equal for a symmetric voltage source model of the antenna, as explained in section 6.4, and that this possible dip at 1.2 THz of the THz current is suppressed. Another sample to highlight in this category is NT-5, a ≈ 3.2 micron long nanotube within a log spiral antenna geometry and bottom gate. This is shown in the inset of Figure 6.7, illustrating the interferogram average and corresponding Fourier transform spectral response. This

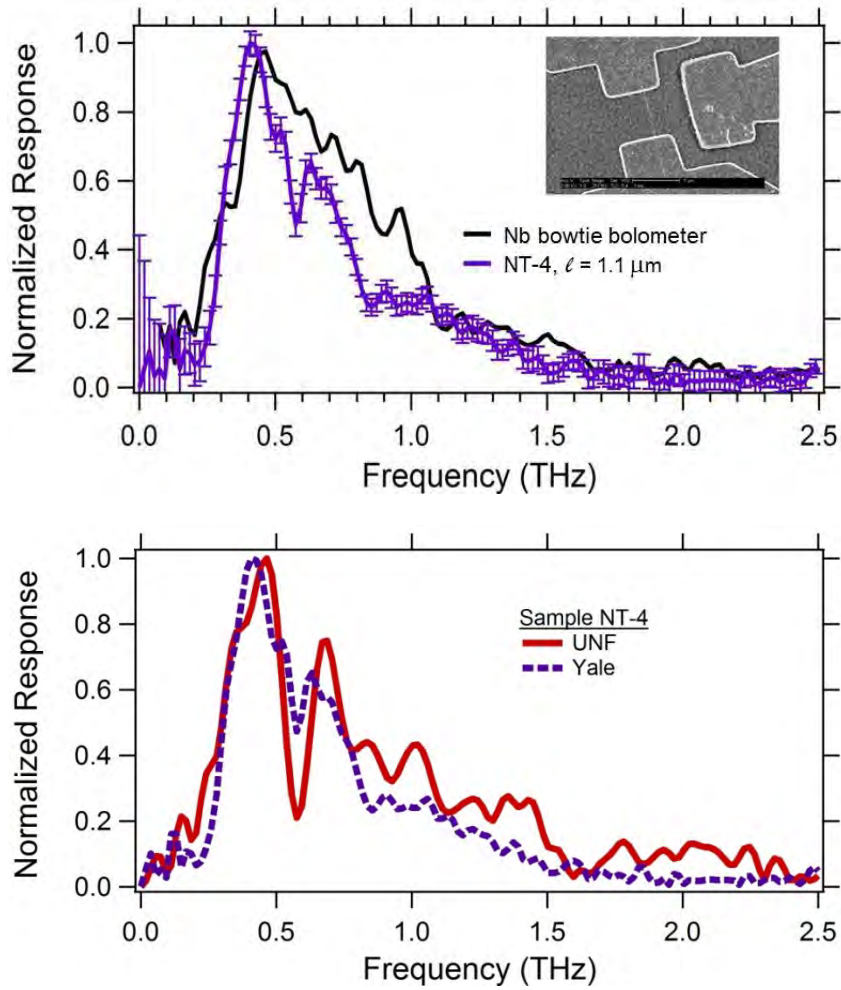


Figure 6.6 – (top) Spectral response of ≈ 1.1 micron long sample NT-4 measured at $I_{\text{bias}} = 30$ nA and $V_{\text{gate}} = -3$ V exhibiting a prominent dip at ≈ 0.6 THz corresponding to $g \approx 0.7$. (bottom) Response of sample NT-4 measured in the FTIR system at University of North Florida with $I_{\text{bias}} = 80$ nA that also shows a significant feature in the spectral response at the same frequency.

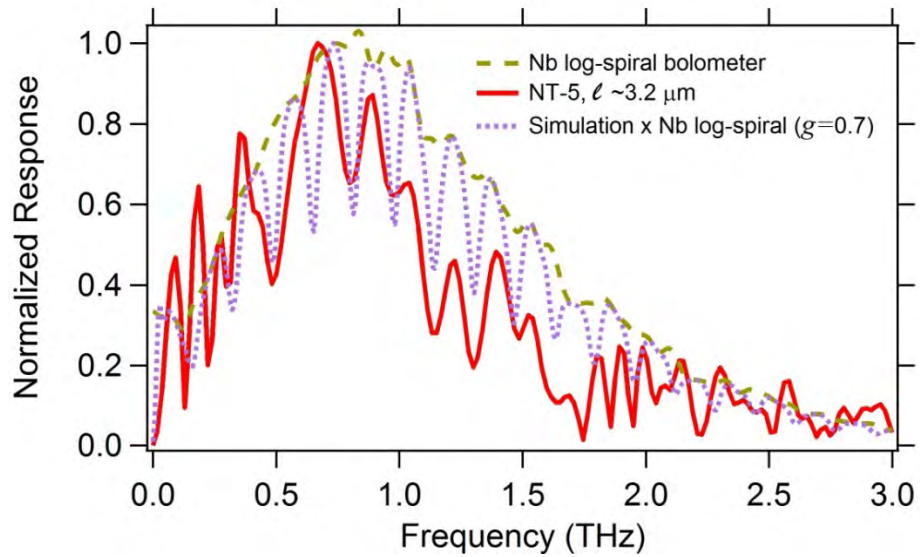


Figure 6.7 – Spectral response of ≈ 3.2 micron long sample NT-5 in a log-spiral antenna geometry measured at $I_{\text{bias}} = 5$ nA and $V_{\text{gate}} = -32$ V. A periodic resonance behavior is observed that can be fit with $g \approx 0.7$.

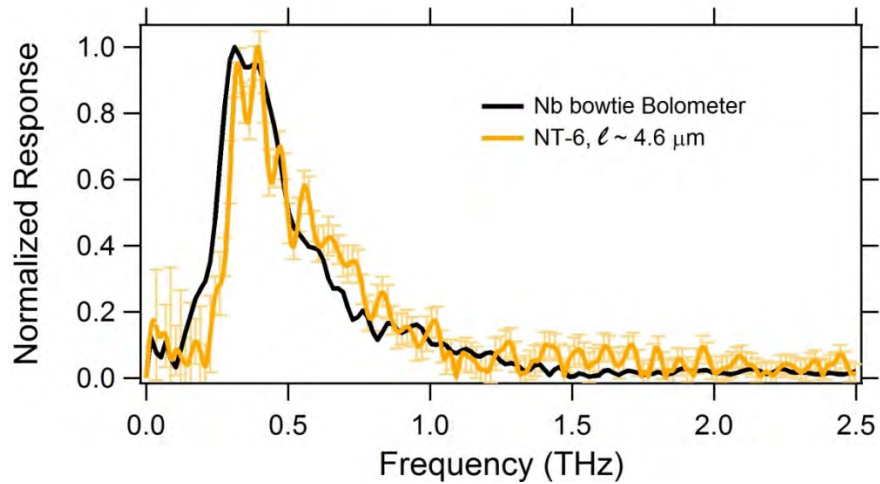


Figure 6.8 – Spectral response of ≈ 4.6 micron long sample NT-6 in a bowtie antenna geometry measured at $I_{\text{bias}} = 20$ nA and $V_{\text{gate}} = -0.6$ V exhibiting a periodic behavior corresponding to $g \approx 1$.

sample, due to its increased length and greater bandwidth antenna, shows the periodicity of the dip feature in the spectral response. Measured at a bias current of $I_{dc} = 5$ nA and $V_{gate} = -32$ V, the frequency spacing of the dip features for this device is $\Delta f \approx 0.17$ THz, also corresponding to a $g \approx 0.7$. Microwave Office simulations of this device's properties with the frequency spacing confirmed this value of g , as shown by the dotted line in the figure.

A sample to discuss from the second category mentioned above is a ≈ 4.6 micron long nanotube device in a bowtie antenna, denoted as NT-6, shown in Figure 6.8. This was measured at $I_{dc} = 20$ nA and $V_{gate} = -0.6$ V. Several other measurements at other bias conditions, such as 100 nA and -10 V, show similar behavior, but increased noise. This ≈ 4.6 micron long device, a ≈ 3 micron bowtie antenna device, and a ≈ 2.3 micron log-spiral antenna device each showed respective frequency spacings of 0.084 THz, 0.13 THz, and 0.18 THz, all corresponding to $g \approx 1$.

A very few samples showed subtle features that corresponded to lower g values, such as shown in Figure 6.9. This is in the third category of samples observed. This sample, denoted NT-7, is a ≈ 3.2 micron long nanotube in a log-spiral antenna with no nearby gate electrode. It was measured at $I_{dc} = 100$ nA and displays a slight dip within the maximum detection region at $f \approx 0.46$ THz, corresponding to a $g \approx 0.28$.

Many other samples measured fell into the remaining categories and displayed only limited bandwidth, smaller than that expected for the antenna type, with no indications of any resonance within this frequency range. This could possibly be due to misalignment as discussed in Chapter 4 or due to an increased contact capacitance. C_c

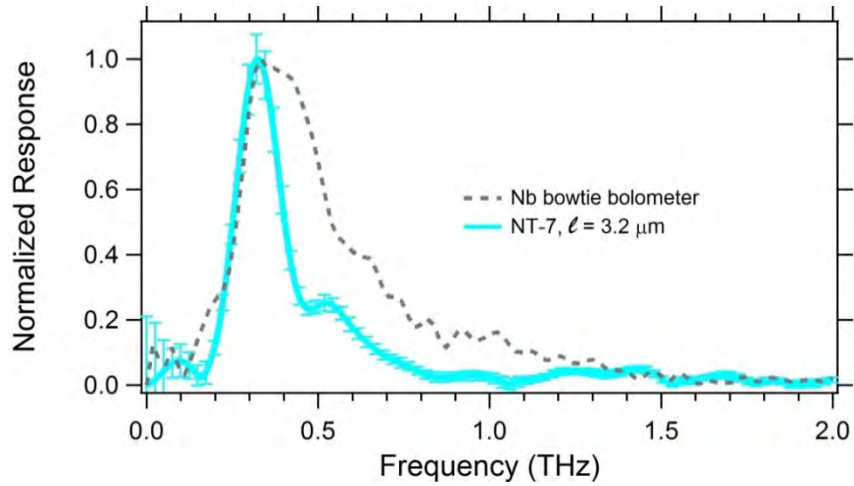


Figure 6.9 – Spectral response of ≈ 3.2 micron long sample NT-7 in a bowtie antenna geometry measured at $I_{\text{bias}} = 100$ nA with no gate electrode revealing a slight feature at ≈ 0.46 THz possibly corresponding to $g \approx 0.28$.

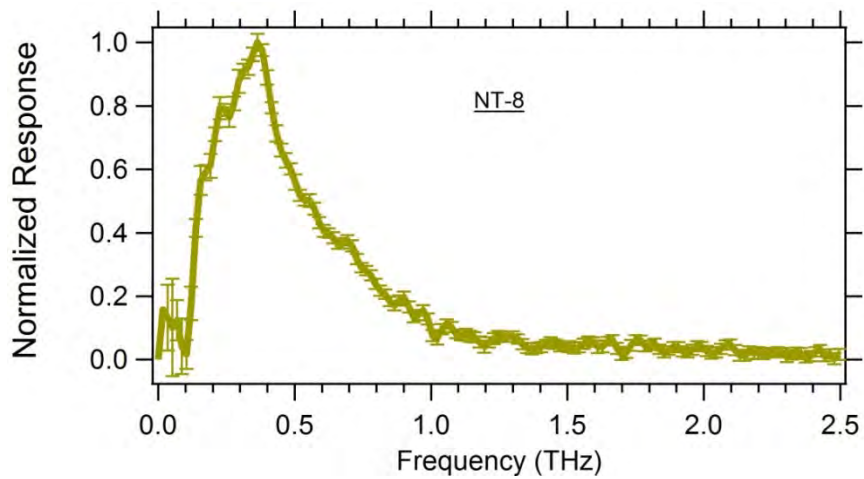


Figure 6.10 – Spectral response of ≈ 2.5 micron sample NT-8 in a log-spiral antenna geometry measured at $I_{\text{bias}} = 100$ nA with no gate electrode revealing no significant features.

becomes more relevant at higher frequency. If $C_c \sim 10$ aF, at a frequency of 2 THz the magnitude of the shunt impedance would be ~ 8 k Ω , significantly less than the ~ 20 k Ω or greater contact resistance in the ZBA. Thus, the nonlinear detection by the nanotube via the nonlinear contact resistance would be expected to be shunted as the frequency increases, which explains the observed drop in device response at higher frequency. Other samples produced reasonable interferograms, but the corresponding spectra were too noisy to reliably determine any reproducible features that could be attributed to the resonances. This was often the case for extremely high resistance samples, such as NT-3, or for spectra where no features were observed, such as in Figure 6.10. Yet other devices did not show any THz response at all. The very few samples that exhibited bolometric detection at higher bias current were much too noisy to produce any meaningful interferograms for spectral analysis.

A comparison of all the samples measured is shown on a single graph, Figure 6.11, where the antenna and gate geometry is indicated. Plotting the resonant frequency spacing as a function of the inverse length of the device we can determine the average g value and see the three different categories for the g values measured. As illustrated in the equation $\Delta f = \frac{v_F}{2Lg}$ introduced in Chapter 3, the slope of a line in this plot is related to the Luttinger parameter g as $\frac{v_F}{2g}$. Three trends are clearly evident by fitting these to straight lines and can be used to determine the Luttinger parameter. Several samples have $g = 1$, representing the non-interacting case with propagation at the Fermi velocity. These samples would agree with the measurements and results obtained by Zhong *et al.* (2008). The bulk of our data is distinctly in between these two cases, $g = 0.3$ and $g = 1$, and allows us to conclude that the single-walled carbon nanotube samples measured in the

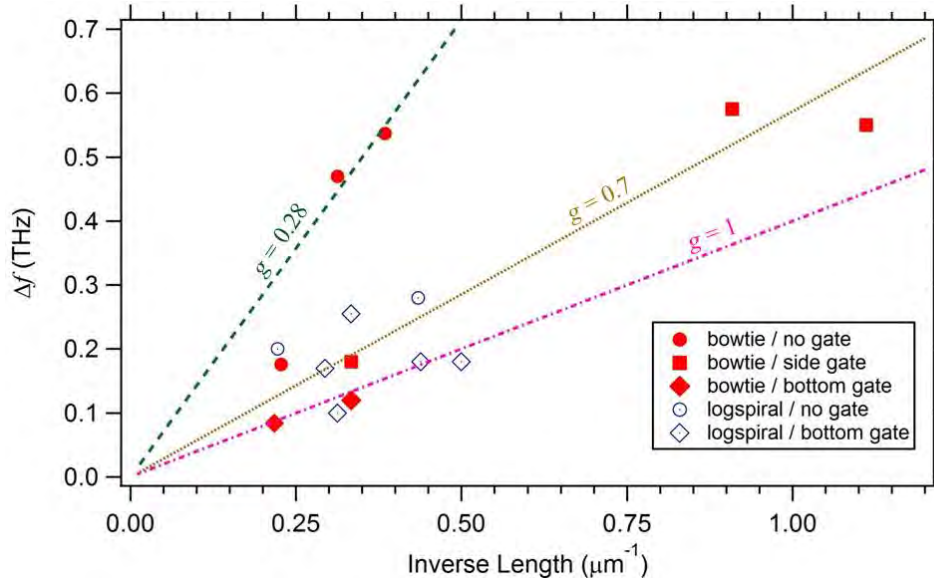


Figure 6.11 – Observed frequency spacing for antenna-coupled single-walled carbon nanotube devices determined from features in their respective measured spectral response plotted as a function of inverse length. The antenna and gate geometries are specified. These devices can be categorized into three groups corresponding to Luttinger parameters g of 0.28, ≈ 0.7 and 1.

Table 6.1 - Summary of sample characteristics for antenna-coupled individual single-walled carbon nanotube devices discussed in text. R is the nanotube dc resistance in the ZBA corresponding to the specified biasing conditions, Δf is the measured frequency spacing determined from features in the THz spectral response using nonlinear detection, the Luttinger parameter g is calculated the half-wavelength resonant condition between the length and frequency spacing, and C_{tot} is from transmission line simulations to fit the observed frequency spacing features.

Sample	Length	Contact Structure		Biasing conditions		R (k Ω)	Δf (THz)	g	C_{tot} (aF/ μ m)
		Antenna	Gate	I_{bias}	V_{gate}				
NT-2	0.9 μ m	bowtie	side-gate	50 nA,	-6 V	40	0.55	0.74	240
NT-4	1.1 μ m	bowtie	side-gate	30 nA	-3 V	50	0.6	0.65	150
NT-5	3.2 μ m	log-spiral	bottom-gate	5 nA	-32 V	700	0.18	0.7	200
NT-6	4.6 μ m	bowtie	bottom-gate	20 nA	-0.6 V	31	0.09	1	350
NT-7	3.2 μ m	bowtie	no gate	100 nA	-	32	0.46	0.28	30
NT-8	2.5 μ m	log-spiral	no gate	100 nA	-	39	-	-	-

geometries discussed are indeed described by Luttinger liquid theory as 1D conductors possessing a faster propagation speed for the charge mode due to electron-electron interactions. However, the magnitude of the strength for these electron-electron interactions is not as great as predicted or observed in other experiments, which predict a $g \approx 0.3$ for single-walled carbon nanotubes (Kane 1998, Bockrath 1999, Ilani 2006). Only two samples studied may fit the predicted case of $g \approx 0.3$. However, as explained in Chapter 2 and illustrated in Table 2.1, there is tremendous variation in the theoretical and experimental g values found for carbon nanotube and other 1D systems. Furthermore, some believe that g cannot trivially be related to intricate microscopic parameters of the system, and thus the theories may not accurately predict the value of g (EA Kim private communication). For example, Auslaender *et al.* also examined spin-charge separation in 1D and note that the microscopic details are very difficult to determine, especially due to their dependence on the carrier density, which controls the ratio between the Coulomb interaction and the kinetic energy (Auslaender 2005). Another study of the tunneling into a quantum wire found a g value of 0.55, but claims an assumed linearity that yields a common velocity for all the charge excitations of the system regardless of energy. The authors declare that this may not be a well-founded assumption and go on to express that this highlights a gap in the theoretical understanding of interacting 1D systems where a complete microscopic description of kinetics and energy relaxation in the strongly interacting limit does not presently exist (Barak 2010).

6.5 Beyond the Luttinger Liquid Picture

The observed value of $g \approx 0.7$ for many of our nanotube samples is larger than the theoretically accepted and measured value of $g \approx 0.3$ from theory (Kane 1998, Bockrath 1999) or experiments which only found $g = 1$ (Zhong 2008). The explanations of these previous reports in the literature of the velocity of charge modes in 1D systems may apply to our samples as well. One of the few experiments undertaken to explore spin-charge separation was by Jompol *et al.* (Jompol 2009) who performed a challenging experiment to probe spin-charge separation in Luttinger liquid of 1D wires formed using split gates on a 2D electron gas which can be squeezed by a negative gate voltage. They investigated the power-law tunneling conductance as a function of temperature and voltage in the ZBA, as others had done previously and we did for our nanotube devices in Chapter 2.2.2. Using the power-law exponents obtained from these tunneling conductance measurements, they extract $g \approx 0.28$. In addition, they used the application of a magnetic field to probe spin-charge separation in their 1D system and find distinct spin waves and charge waves. The spin waves are found to travel at the Fermi velocity while the charge waves propagate at a speed $\approx 40\%$ faster. The ratio of these speeds yields the Luttinger parameter $g \approx 0.7$. The values found are very similar to our results, despite the distinct system being studied. Furthermore, it is important to note that the two different measurement schemes by this group on the same devices produce different values of g . The investigation of the ZBA tunneling conductance exponent gives a much smaller value of g than the value extracted from the charge wave propagation velocity. The authors provide several possible explanations, including the possibility that impurities or imperfections in the wires make the effective length of each wire shorter than the lithographic defined length, that the ZBA power-law treatment regime should be

modified, or that the difference may be a reflection of different physics dominating the two experimental regimes. The effective length for the resonances observed in our study is not a viable explanation for our observed discrepancy to the theoretical value. Take NT-2 for example. With the measured dip at $f \approx 0.6$ THz, assuming a shorter effective nanotube length would correspond to a larger g value, further from the predicted value.

Similar to our study of standing wave resonances on a carbon nanotube, Lee *et al.* report on the real space imaging of 1D standing waves as direct evidence of a Luttinger liquid in metallic single-walled carbon nanotubes using scanning tunneling microscope topography and position-resolved scanning tunneling spectroscopy (Lee 2004). They observe two electronic standing waves produced by spin-charge separation and find a Luttinger parameter of ≈ 0.55 . They explain the discrepancy between this value and the predicted theoretical value of ≈ 0.3 by stating that the underlying metallic substrate significantly reduces the effective Coulomb interaction range of the 1D electrons in the nanotube, screening the Coulomb interaction to some degree, and increasing the g value accordingly. This screening by the gate electrode is a possible explanation for the increased Luttinger parameter value observed in some of our results. As shown in Figure 6.11, for two of the samples studied that did not have a side-gate electrode or for which the sample was shielded from the side-gate electrode show a g value closer to the predicted value. This may indicate that the side- or bottom-gate electrode is indeed a source of electron screening. Testing this further would be appealing, but it is difficult since a typical nanotube device is truly quasi-metallic, as discussed in Chapter 1. Thus, it is challenging to guarantee that the device will be doped away from the energy gap without a gate connection. Furthermore, the transmission line model employed assumes a

conducting ground plane in proximity to the nanotube. Future studies of nanotubes in varying contact conditions with alternative substrates may further elucidate this possible effect.

The Luttinger liquid theory has proven to be a useful paradigm for description of 1D quantum fluids in the low energy limit. However, the linear Luttinger liquid theory description lacks intrinsic mechanisms of relaxation and equilibration. There have been several theoretical studies which examine the decay of a plasmon into the neutral modes in a carbon nanotube (Chen 2010) or take into account other higher-order processes in descriptions that go beyond the Luttinger liquid picture (Barak 2010, Imambekov 2012). Chen *et al.* evaluated the intrinsic rate of energy loss of a plasmon in a disorder-free clean finite-length arm-chair carbon nanotube connected to two metal leads subjected to a THz electrical field. In the typical Luttinger liquid model, the absence of coupling between the bosonic spin and charge modes precludes the possibility of plasmon decay. However, they find that conservation of energy and momentum does indeed allow for a plasmon to decay into the neutral bosonic excitations modes of an electron liquid when facilitated by backscattering processes. Moreover, during this plasmon decay, excitations of neutral modes generated during plasmon decay can propagate in two distinct directions, forward or backward in the 1D system. However, a plasmon that has decayed into neutral modes that continue to propagate in the same direction can then recombine into a plasmon, further complicating the scenario. The decay of a plasmon into the neutral modes may be an explanation for the surprising results found by Zhong *et al.* (2008) with a measured propagation velocity exactly equal to the Fermi velocity, corresponding to the noninteracting $g = 1$ case. For longer nanotube samples, there is a greater likelihood of a

scattering event to occur during the transit time of the ballistic resonances. This may also apply to our experiment. Thus, we find for several of the longer nanotube devices studied that $g \approx 1$.

Beyond the low-energy limit, nonlinearity of the dispersion relation between energy and momentum becomes significant and other higher-order processes must be taken into account. A new theory is in the development stage which re-represents the linear Luttinger liquid theory in terms of fermionic quasiparticles that may be more useful than the bosonization treatment (Imambekov 2012). This and the plasmon decay processes mentioned above can lead to a finite particle lifetime of the excitation. So the total effective propagation velocity of the overall excitation with a finite lifetime could be a combination of the neutral mode velocity which coincides with the Fermi velocity v_F and a faster velocity v_p , which may explain a more complicated parameter of g with a value that corresponds to an average of these two velocities or that the underlying basis of spin-charge separation may need to be reevaluated (Schmidt 2010).

6.6 Conclusions and Future Work

Carbon nanotubes are materials exhibiting fascinating electrical properties and providing a laboratory to study 1D electron behavior. Electrons in a 1D system are unable to rearrange themselves to minimize electron-electron interactions, motivating a need for a new description of electron states in carbon nanotubes that is expected to dramatically differ from 3D. The Luttinger liquid picture describes low-energy electron excitations in a 1D system with strong electron-electron interactions and predicts a power-law tunneling of electrons as well as spin-charge separation. The Luttinger interaction

parameter g quantifies the strength of electron-electron interactions. While the theory of spin-charge separation is well developed for 1D systems and there is general agreement on the 1D nature of individual single-walled carbon nanotubes, the experimental results have been lacking or conflicting. Signatures of spin-charge separation can be revealed in the differing propagation velocities of the spin and charge modes, also referred to as the neutral and plasmon modes, which naturally arise from the modelling of a carbon nanotube as a transmission line. We fabricated micron long antenna coupled single-walled carbon nanotube devices to study in an FTIR spectrometer in order to excite THz standing wave resonances to ascertain the charge mode propagation velocity.

For an individual single-walled carbon nanotube, we have been able to determine the thermal conductivity as a function of length and temperature. Using rf detection we observe both bolometric and nonlinear responses in two different bias regimes. We have been able to exploit the nonlinear detection at THz frequencies to investigate the fundamental properties of the nanotube. We find an upper limit on the contact capacitance to a nanotube. Using the carbon nanotube nonlinear contact resistance known as the ZBA to produce nonlinear detection of a THz signal, we analyze the spectral response and find signatures of resonances which indeed correspond to a plasmon mode propagation velocity faster than the Fermi velocity for many samples. The propagation velocity for many of the devices studied corresponds to a Luttinger interaction parameter $g \approx 0.7$. This value is larger than the theoretical prediction, which may be a result of the device geometry employed. However, this is also distinct from previous experimental reports that only found $g = 1$ and did not discern any indications of the faster propagation velocity. Only a few devices agreed with the predicted $g \approx 0.3$. The discrepancy might

reveal the need to go beyond the simple Luttinger liquid picture for the decay of the plasmon mode into neutral modes. Further work on these experiments employing better averaging, improved signal to noise, and lower resistance devices may improve the findings. A successful measurement of an interferogram using bolometric detection or on suspended nanotubes may also reveal further indications of Luttinger liquid behavior. These experiments have focused on probing an exciting fundamental physics question through the use of an experimentally accessible 1D system, and the results can have implications for the use of carbon nanotubes in actual high-frequency devices operating into the THz range, such as nanoscale transistors or interconnects.

Future work can use the techniques described in this dissertation for investigating the transport phenomena of other novel conducting nanosystems. Analogous to carbon, boron has been theorized to form stable hollow cylindrical structures that arise from triangular boron sheets (Tang 2007). Boron sheets themselves would be an extremely interesting new area to study. Boron nanotubes, similar to their carbon counterpart, are predicted to possess many remarkable properties. They are even expected to outperform carbon nanotubes in several ways (Bezugly 2011). For example, irrespective of the lattice structures or chirality, boron nanotubes are predicted to always be metallic with higher conductivities than carbon nanotubes. So far, boron nanotube synthesis has been limited. Ciuparu *et al.* reported the first creation of boron nanotubes (Ciuparu 2004) and more recently there have been accounts describing the observation of an all-boron fullerene (Zhai 2014). The successful synthesis of long boron nanotubes using a reliable method paralleling the CVD growth techniques of carbon nanotubes would lead to an explosion of new research, just as occurred following the discovery of carbon nanotubes. Electrical,

thermal, and optical experimental studies of boron nanotubes, including the THz regime, would be fascinating and herald in a completely new area of exploration and potential applications. New models of a boron nanotube as a transmission line and within the Luttinger liquid framework would be exciting. Just as with carbon nanotubes, exciting standing wave resonances on a boron nanotube could reveal Luttinger liquid behavior in this nanoscale system. If tangible boron nanotubes are shown to have much lower internal resistance, similar high-frequency experiments to those described in this work, but measured in the highly developed microwave regime, may have the ability to uncover the subtle effects beyond the simple Luttinger liquid picture. These boron nanotubes may even possess properties making them viable for very sensitive THz detectors. The development of carbon nanotube devices operating at THz frequencies could be advantageous from a technology standpoint.

The parent material to carbon nanotubes, graphene has itself been the subject of much focus from an interesting physics perspective in addition to applications. Using graphene as the active element in a THz detector has been proposed (McKitterick 2013, Du 2014). Due to the very small heat capacity of an atomically thin sheet, graphene and carbon nanotubes may produce exceptionally fast and sensitive bolometric detectors, when merged with the very strong temperature dependent resistance of proximity-induced superconductivity (Kasumov 1999). The THz setup used would be a good system for examining graphene or carbon nanotubes contacted by superconducting leads. Further understanding of the non-Ohmic contact to a carbon nanotube or graphene could also introduce other very sensitive detectors based on nonlinear detection mechanism. For a sample with perfect transmission and only the quantum of resistance at the interface, it

would be interesting to investigate the dissipation of energy, such as whether it occurs in the contacts, in the quantum channel or in some combination of the two.

The techniques described here can also be used to explore the potential competition between strong electron-electron repulsion of a 1D system and the phonon-mediated attractive electron-electron interaction of a Cooper pair that can arise from superconductivity. Employing superconducting contacts to a nanotube has been shown to proximitize the nanotube and allow for the flow of supercurrents in such a small system (Kasumov 1999). Theoretical studies of such systems have been reported (Fazio 1999, Karnaukhov 2002), but experimental tests are lacking. Furthermore, there have also been reports of intrinsic superconductivity in as-grown and doped carbon nanotubes (Kociak 2001, Kasumov 2003, Tang 2001, Murata 2008, Shi 2012). Investigating these reports and comparing the conventional superconductivity representation with the bosonic waves of the 1D Luttinger liquid picture would add to the understanding and future evolution of these concepts based on electron-electron interaction.

The collection of combinations conceivable by uniting novel nanosystems (such as carbon nanotubes, graphene or boron nanotubes) possessing exotic behavior (such as superconductivity or Luttinger liquid physics) with new measurement schemes (such as electrothermal studies in the THz regime) present a wide array of exciting unexplored areas to examine in the future. In addition to answering fundamental physics questions, discoveries from such work may also offer valuable technological applications that will have a major impact on the world.

Bibliography

Ajayan, P.M. and Q. Z. Zhou, "Applications of Carbon Nanotubes," *Top. Appl. Phys.* 80, 391–425 (2001).

Ando, T. and T. Nakanishi, "Impurity Scattering in Carbon Nanotubes," *J. Phys. Soc. Jpn.* 67 1704 (1998).

Ando, T., T. Nakanishi, and R. Saito, "Berry's Phase and Absence of Back Scattering in Carbon Nanotubes," *J. Phys. Soc. Jpn.* 67 2857 (1998).

Auslaender, O. M. *et al.*, "Spin–charge separation and localization in one dimension," *Science* 308, 88–92 (2005).

Auslaender, O.M. *et al.*, "Tunneling Spectroscopy of the Elementary Excitations in a One-Dimensional Wire" *Science* 295, 825 (2002).

Auslaender, O.M., A. Yacoby, R. de Picciotto, K. W. Baldwin, L. N. Pfeiffer, and K. W. West, "Tunneling spectroscopy of the elementary excitations in a one-dimensional wire," *Science*, vol. 295, pp. 825–828 (2002).

Bachtold, A. *et al.* "Suppression of tunneling into multiwall carbon nanotubes," *Phys. Rev. Lett.* 87, 166801 (2001).

Bae, D.J. *et al.*, "Transport phenomena in an anisotropically aligned single-wall carbon nanotube film," *Phys. Rev. B* 64, 233401 (2001).

Barak, G., H. Steinberg, L. N. Pfeiffer, K. W. West, L. I. Glazman, F. von Oppen, and A. Yacoby, "Interacting electrons in one dimension beyond the Luttinger-liquid limit," *Nature Phys.* 6, 489 (2010).

Bethune, D.S., *et al.*, "Atoms in carbon cages: the structure and properties of endohedral fullerenes" *Nature* 366, 123 (1993).

Bezugly, V., *et al.* "Highly conductive boron nanotubes: transport properties, work functions, and structural stabilities," *ACS nano* 5.6: 4997-5005 (2011).

- Biercuk, M.J., S. Ilani, C.M. Marcus, and P.L. McEuen, “Electrical Transport in Single-Walled Carbon Nanotubes.” In Carbon Nanotubes, Topics in Applied Physics 111, 455 Dresselhaus and Dresselhaus eds. (2008).
- Binnig, G., H. Rohrer, Ch. Gerber, and E. Weibel, Phys. Rev. Lett. 49, 57–61 (1982).
- Bockrath, M. *et al.*, “Luttinger-liquid behaviour in carbon nanotubes,” Nature 397, 598–601 (1999).
- Bockrath, M., “Carbon Nanotubes: Electrons in One Dimension,” Doctoral Dissertation, University of California, Berkeley (1999).
- Brintlinger, T., Y.-F. Chen, T. Dürkop, E. Cobas, M.S. Fuhrer, J.D. Barry, and J. Melngailis “Rapid Imaging of Nanotubes on Insulating Substrates” Applied Physics Letters 81, 2454 (2002).
- Bronn, N. and Mason, N., “Spatial dependence of electron interactions in carbon nanotubes,” PRB 88 161409R (2013).
- Burke, P.J. “Luttinger liquid theory as a model of the gigahertz electrical properties of carbon nanotubes,” IEEE Trans. On Nanotech. 1(3) 129-144 (2002).
- Burke, P.J., “AC Performance of Nanoelectronics: Towards a Ballistic THz Nanotube Transistor,” Solid State Electronics 48 (10), 1981-1986 (2004).
- Burke, P., *Selected Topics in Electronics and Systems: Nanotubes and Nanowires*, Vol. 44, World Scientific (2007).
- Caldwell, R., “Synthesis and electronic transport in single-walled carbon nanotubes of known chirality,” Doctoral Dissertation, Columbia University (2011).
- Carrion, E., M. Muthee, J. Donovan, R. Zannoni, J. Nicholson, E. Polizzi and K.S. Yngvesson, Proceedings of the 20th International Symposium on Space Terahertz Technology, Charlottesville, pp. 110-119 (2009).
- Carrion, E., M. Muthee, Z. Chen, J. Nicholson, E. Polizzi, and K.S. Yngvesson. “Single Wall Carbon Nanotube (SWCNT) Devices as THz detectors and Mizers,” Proc. 21th Intern. Symp. Space Terahertz Technol., Oxford, March 23-25 (2010).
- Chai, Y., *et al.*, “Low-Resistance Electrical Contact to Carbon Nanotubes With Graphitic Interfacial Layer,” IEEE Trans. on Electron Devices, 59 1 (2012).
- Chamon, C., and E. Fradkin, “Distinct universal conductances in tunneling to quantum Hall states: The role of contacts,” Phys. Rev. B 56, 2012 (1997).

Chen, Z., J. Appenzeller, J. Knoch, and P. Avouris "The Role of Metal–Nanotube Contact in the Performance of Carbon Nanotube Field-Effect Transistors" *Nano Lett.*, 5 (7), pp 1497–1502 (2005).

Chen, W., A. V. Andreev, E. G. Mishchenko, and L. I. Glazman, "Decay of a plasmon into neutral modes in a carbon nanotube," *Phys. Rev. B* 82, 115444 (2010).

Chudow, J.D., D.F. Santavicca, C.B. McKitterick, D.E. Prober and P. Kim, "Terahertz detection mechanism and contact capacitance of individual metallic single-walled carbon nanotubes," *Appl. Phys. Lett.* 100, 163503 (2012).

Ciuparu, D., R. F. Klie, Y. Zhu, L. Pfefferle "Synthesis of Single Wall Pure Boron Nanotubes," *J. Phys. Chem. B*, 108, 3967–3969 (2004).

Cobas E., and M. S. Fuhrer, "Microwave rectification by a carbon nanotube Schottky diode," *Appl. Phys. Lett.*, 93, 043120 (2008).

Collins, P.G., M.S. Fuhrer & A. Zettl. "1/f noise in carbon nanotubes." *Appl. Phys. Lett.* 76, 894 (2000).

Compton R.C., *et al.*, "Bow-tie antennas on a dielectric half-space: Theory and experiment," *IEEE Trans. Antennas Propag.* 35, 622 (1987).

Connelly, B.C., "Quantitative Characterization of Steady and Time-Varying, Sooting, Laminar Diffusion Flames using Optical Techniques" Doctoral Dissertation, Yale University (2009).

Cooley, J.W. and J.W. Tukey, "An Algorithm for the Machine Calculation of Complex Fourier Series," *Mathematics of Computation*, Vol. 19, No. 90 pp. 297-301 (1965).

Cowley, A.M. and H.O. Sorensen, "Quantitative Comparison of Solid State Microwave Detectors," *IEEE Trans.on Microwave Theory and Techniques*, Vol. MTT-14, No. 12, (1966).

Cuniberti, G., M. Sassetti, M., and B. Kramer, "Ac conductance of a quantum wire with electron-electron interactions," *Phys. Rev. B*, vol. 57, no. 3, pp. 1515–1526 (1998).

Datta, S., *Electron transport in mesoscopic systems*, Cambridge university (1995).

Dekker, C. "Carbon nanotubes as molecular quantum wires." *Physics today* 52, 22-30 (1999).

Derycke, V., R. Martel, J. Appenzeller, and Ph. Avouris, "Carbon nanotube inter- and intramolecular logic gates," *Nano Lett.* 1, 453 (2001).

Deshpande, V.V., M. Bockrath, L.I. Glazman and A. Yacoby, *Nature* 464, 209 (2010).

- Devoret, M.H., *et al.*, “Effect of the electromagnetic environment on the Coulomb blockade in ultrasmall tunnel junctions,” *Phy. Rev. Letter.* 64, 1824 (1990).
- Dóra, B., M. Gulácsi, F. Simon, and H. Kuzmany, “Spin Gap and Luttinger Liquid Description of the NMR Relaxation in Carbon Nanotubes,” *Phys. Rev. Lett.* 99, 166402 (2007).
- Du, X., D.E. Prober, H. Vora, and C.B. McKitterick, “Graphene-based Bolometers,” *Graphene and 2D Materials* 1 1 (2014).
- Dyson, J.D., “The equiangular spiral antenna,” *IRE Trans. Antennas Propag.* 7, 181 (1959).
- Kim, Eun-Ah. Private communication, Correlated Electron Systems Gordon Conference, Mount Holyoke, MA (2012).
- Egger, R., and G. Gogolin, “Effective Low-Energy Theory for Correlated Carbon Nanotubes,” *Phys. Rev. Lett.* 79, 5082 (1997).
- Egger, R., “Luttinger liquid behavior in multi-wall carbon nanotubes,” *Phys. Rev. Lett.* 83, 5547 (1999).
- Egger, R. *et al.*, “Bulk and Boundary Zero-Bias Anomaly in Multiwall Carbon Nanotubes,” *Phys. Rev. Lett.* 87, 066401 (2001).
- Endo, M., M. S. Strano, and P. M. Ajayan, “Potential Applications of Carbon Nanotubes”, *Carbon Nanotubes*, 111, 13-61 (2008).
- Ferguson, B. and X.-Ch. Zhang, “Materials for terahertz science and technology,” *Nature Materials* 1, 26 (2002).
- Filipovic, D.F., S.S. Gearhart, and G.M. Rebeiz. “Double-slot antennas on extended hemispherical and elliptical silicon dielectric lenses.” *IEEE Transactions on Microwave Theory and Techniques* 41(10) 1738-1749 (1993).
- Finnie, P., *et al.* “Charge contrast imaging of suspended nanotubes by scanning electron microscopy,” *Nanotechnology*, 19 335202 (2008).
- Fisher, M.P.A, L.I. Glazman. *Transport in one-dimensional Luttinger liquid. In: Mesoscopic Electron Transport*, ed. by L.L. Sohn, L.P. Kouwenhoven, and G. Schoen. NATO ASI Series, Vol. 345, Kluwer Academic Publishers (1997).
- Friedel, R. and P.B. Israel, In *Edison's Electric Light: The Art of Invention*, JHU Press (2010).

- Fu, K., R. Zannoni, C. Chan, S. H. Adams, J. Nicholson, E. Polizzi and K. S. Yngvesson, "Terahertz detection in single wall carbon nanotubes," *Appl. Phys. Lett.* 92, 033105 (2008).
- Galeazzi, M., and D. McCammon, "Microcalorimeter and bolometer model," *J. Appl. Phys.* 93, 4856 (2003).
- Gao, B., A. Komnik, R. Egger, D.C. Glattli, A. Bachtold, "Evidence for Luttinger-liquid behavior in crossed metallic single-wall nanotubes," *Phys. Rev. Lett.* 92, 216804 (2004).
- Gasparyan, F., "Low-Frequency Noise in Field-Effect Devices Functionalized With Dendrimer/Carbon- Nanotube Multilayers," *Armenian Journal of Physics*, vol. 3, issue 4, pp. 312-341 (2010).
- Geim, A.K. and K.S. Novoselov, "The rise of graphene," *Nature Materials* 6, 183 (2007).
- Geim, A.K., and P. Kim, "Carbon wonderland," *Scientific American* 298 (4), 68-75 (2008).
- Gershenson, E. G. Goltsman, I. Gogidze, Y. Gusev, A. Elantiev, B. Karasik, and A. Semenov. *Sov. Superconductivity* 3, 2143 (1990).
- Gonzalez, F.J. and G.D. Boreman, "Comparison of dipole, bowtie, spiral and log-periodic IR antennas," *Infrared Physics & Technology* 46, 418–428 (2005).
- Hamada, N., S. Sawada, A. Oshiyama, "New one-dimensional conductors: Graphitic microtubules" *Phys. Rev. Lett.* 68, 1579 (1992).
- Hanson, G.W., "Fundamental Transmitting Properties of Carbon Nanotube Antennas", *IEEE Transactions on Antennas and Propagation*, Vol. 53, No. 11, pp. 3426–3435 (2005).
- Hartmann, R. R., Kono, J., and Portnoi, M. E., "Terahertz science and technology of carbon nanomaterials," *Nanotechnology* 25 322001 (2014).
- Hata, K., N.D. Futaba, K. Mizuno, T. Namai, M. Yumura, S. Iijima, "Water-Assisted Highly Efficient Synthesis of Impurity-Free Single-Walled Carbon Nanotubes," *Science* 306, 1362 (2004).
- Hayashi, T., Y.A. Kim, T. Natsuki, and M. Endo, "Mechanical Properties of Carbon Nanomaterials" *ChemPhysChem*, Volume 8, Issue 7, 999–1004, (2007).
- Herres W., and J. Gronholz "Understanding FTIR Data Processing" (1985).
- Homma, Y., S. Suzuki, Y. Kobayashi, M. Nagase, and D. Takagi, "Mechanism of bright selective imaging of single-walled carbon nanotubes on insulators by scanning electron microscopy," *Appl. Phys. Lett.* 84, 1750 (2004).

Homma, Y., D. Takagi, S. Suzuki, K. Kanzaki, and Y. Kobayashi, "Electron-microscopic imaging of single-walled carbon nanotubes grown on silicon and silicon oxide substrates," *J. Electron. Microsc.* 54, i3 (2005).

Hone, J., *Carbon Nanotube: Thermal Properties Dekker Encyclopedia of Nanoscience and Nanotechnology* 603 (2004).

Hone, J. *et al.*, "Quantized Phonon Spectrum of Single-Wall Carbon Nanotubes," *Science* 289, 1730 (2000).

Hong, B.H., *et al.*, "Quasi-Continuous Growth of Ultralong Carbon Nanotube Arrays," *J. Am. Chem. Soc.* 127 (44), pp 15336–15337 (2005).

Hortensius, H.L., A. Ozturk, P. Zeng, E.F.C. Driessen, and T.M. Klapwijk, "Microwave-induced nonequilibrium temperature in a suspended carbon nanotube," *Appl. Phys. Lett.* 100, 223112 (2012).

Huang, S., *et al.*, "Growth Mechanism of Oriented Long Single Walled Carbon Nanotubes Using "Fast-Heating" Chemical Vapor Deposition Process," *Nano Letters* 4 (6), pp 1025–1028 (2004).

Huang, L., *et al.*, "Long and Oriented Single-Walled Carbon Nanotubes Grown by Ethanol Chemical Vapor Deposition," *J. Phys. Chem. B*, 108 (42), pp 16451–16456 (2004).

Hunger T., B. Lengeler, and J. Appenzeller, "Transport in ropes of carbon nanotubes: Contact barriers and Luttinger liquid theory," *Phys. Rev. B*. vol, 69, 195406 (2004).

Ihara, Y., P. Wzietek, H. Alloul, M. H. Rümmeli, Th. Pichler, and F. Simon, "Incidence of the Tomonaga-Luttinger liquid state on the NMR spin-lattice relaxation in carbon nanotubes," *EPL* 90, 17004 (2010).

Iijima, S., "Helical microtubules of graphitic carbon," *Nature* 354, 56–58 (1991).

Iijima, S., and T. Ichihashi, "Single-shell carbon nanotubes of 1-nm diameter," *Nature* 363, 603 (1993).

Ilani, S., and P.L. McEuen, "Electron Transport in Carbon Nanotubes," *Annual Review of Condensed Matter Physics* 1, 1-25 (2010).

Ilani, S., L.A.K. Donev, M. Kindermann, and P.L. McEuen, "Measurement of the quantum capacitance of interacting electrons in carbon nanotubes," *Nature Phys.* 2, 687-691 (2006).

Imambekov, A., T.L. Schmidt, and L.I. Glazman "One-dimensional quantum liquids: Beyond the Luttinger Liquid Paradigm," *Rev. Mod. Phys.*, 84(3) 1253–1306 (2012).

- Ishii, H., *et al.*, “Direct observation of Tomonaga-Luttinger liquid state in carbon nanotubes at low temperatures,” *Nature* 426, 540–544 (2003).
- Jarillo-Herrero, P., “Quantum Transport in Carbon Nanotubes,” Doctoral Dissertation, TU Delft (2005).
- Javey, A., J. Guo, Q. Wang, M. Lundstrom, H. Dai, “Ballistic carbon nanotube field-effect transistors” *Nature* 424, 654 (2003).
- Jezouin, S., *et al.*, “Tomonaga–Luttinger physics in electronic quantum circuits,” *Nat Commun.* 4: 1802 (2013).
- Jishi, R.A., M.S. Dresselhaus and G. Dresselhaus, “Electron-phonon coupling and the electrical conductivity of fullerene nanotubules,” *Phys. Rev. B*, 48, 11385-11389 (1993).
- Jompol, Y. *et al.* “Probing spin–charge separation in a Tomonaga-Luttinger liquid,” *Science* 325, 597–601 (2009).
- Kane, C.L. and Fisher, M.P.A., “Transport in a one-channel Luttinger liquid,” *Phys. Rev. Lett.* 68, 1220–1223 (1992).
- Kane, C.L., L. Balents, and M. P. A. Fisher, “Coulomb Interactions and Mesoscopic Effects in Carbon Nanotubes,” *Phys. Rev. Lett.* 79, 5086 (1997).
- Kane, C.L., L. Balents, and M.P.A. Fisher, “Coulomb Interactions and Mesoscopic Effects in Carbon Nanotubes,” *PRL* 79, 5086 (1997).
- Kane, C.L., L. Balents and M.P.A. Fisher, “Coulomb Interactions and Mesoscopic Effects in Carbon Nanotubes,” *Phys. Rev. Lett.* 79, 5086–5089 (1998).
- Karnaukhov, I.N. and A.A. Ovchinnikov, “Strongly interacting Luttinger liquid and superconductivity in an exactly solvable model,” *Physical Review B* 66.10: 104518 (2002).
- Kasumov, A. *et al.*, “Supercurrents through single-walled carbon nanotubes,” *Science* 284, no. 5419: 1508-1511 (1999).
- Kasumov, A. *et al.*, “Quantum transport through carbon nanotubes: Proximity-induced and intrinsic superconductivity,” *Physical Review B* 68.21: 214521 (2003).
- Kaverzin A.A., A.S. Mayorov, A. Shytov, and D.W. Horsell. “Impurities as a source of flicker noise in graphene,” *Phys. Rev. B* 85, 075435 (2012).
- Kibis, O.V., *et al.*, “Generation of Terahertz Radiation by Hot electrons in Carbon Nanotubes”, *Nano Lett.*, 7 (11), pp 3414–3417 (2007).

- Kim, N.Y. *et al.*, “Tomonaga-Luttinger Liquid Features in Ballistic Single-Walled Carbon Nanotubes: Conductance and Shot Noise,” *Phys. Rev. Lett.* 99, 036802 (2007).
- Kociak, M. *et al.*, “Superconductivity in ropes of single-walled carbon nanotubes” *Phys. Rev. Lett.* 86, 2416 (2001).
- Kong, J., A.M. Cassel, and H. Dai, “Chemical vapor deposition of methane for single-walled carbon nanotubes,” *Chem. Phys. Lett.* 292:567 (1998).
- Kong, J. *et al.*, “Synthesis of individual single-walled carbon nanotubes on patterned silicon wafers,” *Nature* 395, 878–881 (1998).
- Kroto, H.W., J.R. Heath, S.C. O'Brien, R.F. Curl, and R.E. Smalley, “C60: Buckminsterfullerene,” *Nature* 318 (6042): 162–163 (1985).
- Kumar M. and Y. Ando, “Chemical Vapor Deposition of Carbon Nanotubes: A Review on Growth Mechanism and Mass Production” *Journal of Nanoscience and Nanotechnology* Vol. 10, 3739–3758, 2010
- Landau, L.D. & Lifshitz, E. M. *Course of Theoretical Physics* Vol. 9, 1–27 (Pergamon, 1980).
- Landau, L.D., “The Theory of the Fermi Liquid,” *Sov. Phys. JETP* 3, 920 (1957).
- Landi, B.J., *et al.*, “Carbon nanotubes for lithium ion batteries,” *Energy Environ. Sci.*, 2, 638-654 (2009).
- Lauret, J.S., *et al.*, “Ultrafast Carrier Dynamics in Single-Wall Carbon Nanotubes,” *Phys. Rev. Lett.* 90, 057404 (2003).
- Lee, J., *et al.*, “Real space imaging of one-dimensional standing waves: Direct evidence for a Luttinger liquid,” *Phys. Rev. Lett.* 93, 166403 (2004).
- Léonard, F. *The Physics of Carbon Nanotube Devices*. William Andrew: New York (2008).
- Li, S. *et al.*, “Carbon nanotube transistor operation at 2.6 GHz”, *Nano Lett.* 4 (4), 753-756 (2004).
- Li, J., Y. He, Y. Han, K. Liu, J. Wang, Q. Li, S. Fan, and K. Jiang, “Direct Identification of Metallic and Semiconducting Single-Walled Carbon Nanotubes in Scanning Electron Microscopy” *Nano Lett.*, 12 (8), pp 4095–4101 (2012).
- Liang, J., D. Akinwande and H.-S.P. Wong, “Carrier Density and quantum capacitance for semiconducting carbon nanotubes”. *J. Appl. Phys.*, 104, 064515 (2008).

- Lim, S.C., *et al.*, “Contact Resistance Between Metal and Carbon Nanotube Interconnects: Effect of Work Function and Wettability,” *Appl. Phys. Lett.* 95, 264103 (2009).
- Liu, F., M. Bao, K.L. Wang, C. Li, B. Lei, and C. Zhou, “One-dimensional transport of In₂O₃ nanowires,” *Appl. Phys. Lett.*, vol. 86, 213101 (2005).
- Lu R., Xu, G., and Wu J.Z., “Effects of thermal annealing on noise property and temperature coefficient of resistance of single-walled carbon nanotube films,” *Appl. Phys. Lett.* 93, 213101 (2008).
- Luttinger, J.M., “An exactly solvable model of many-Fermion system,” *J. Math. Phys.*, vol. 4, no. 9, p1154, (1963).
- Malapanis, A., *et al.*, “Current-induced cleaning of adsorbates from suspended single-walled carbon nanotube diodes,” *Appl. Phys. Lett.* 98, 263108 (2011).
- Mann, D. *et al.*, “Ballistic transport in metallic nanotubes with reliable Pd Ohmic contacts,” *Nano Lett.* 3(11) pp1541-1544 (2003).
- Maruyama, S. *et al.*, “Low-temperature synthesis of high-purity single-walled carbon nanotubes from alcohol,” *Chem. Phys. Lett.* 360:229 (2002).
- Maslov, D.L. and M. Stone, “Landauer conductance of Luttinger Liquids with leads,” *Phys. Rev. B*, 52 R5539-42 (1995).
- McEuen, P.L., M. Bockrath, D.H. Cobden, Y.-G. Yoon, and S.G. Louie, “Disorder, Pseudospins, and Backscattering in Carbon Nanotubes,” *Phys. Rev. Lett.* 83, 5098 (1999).
- McEuen, P.L., “Transport in One Dimension,” Doctoral Dissertation, Yale University (1991).
- McKitterick, C.B., D.E. Prober, and B.S. Karasik, “Performance of Graphene Thermal Photon Detectors,” *Journal of Applied Physics* 113 044512 (2013).
- Mishchenko, E.G., *et al.*, “Zero-Bias Anomaly in Disordered Wires,” *Phys. Rev. Lett.* 87, 246801 (2001).
- Monthieux, M. and V. L. Kuznetsov, “Who should be given the credit for the discovery of carbon nanotubes?” *Carbon*, 44 (11) 1621–1623, (2006).
- Müller, A., S.K. Das, P. Kögerler, H. Bögge, M. Schmidtman, A.X. Trautwein, V. Schünemann, E. Krickemeyer, W. Preetz, H. U. Güdel, “A New Type of Supramolecular Compound: Molybdenum-Oxide-Based Composites Consisting of Magnetic

Nanocapsules with Encapsulated Keggin-Ion Electron Reservoirs Cross-Linked to a Two-Dimensional Network,” *Angew. Chem. Int. Ed.* 39, 3413–3417 (2000).

Murata, N., *et al.*, “Superconductivity in thin films of boron-doped carbon nanotubes.” *Physical review letters* 101.2:027002 (2008).

Mutthee, M., “Terahertz Radiation From Single Walled Carbon Nanotubes” Master's Thesis, UMass (2011).

Nakayama, Y., “Synthesis, Nanoprocessing, and Yarn Application of Carbon Nanotubes,” *Jpn. J. Appl. Phys.* 47, 8149 (2008).

Ngai, D.H., C.-Y. Hou, E.-A. Kim, “Proposal for Extracting the Luttinger Liquid Velocity in Carbon Nanotubes,” APS March Meeting (2011).

Nougaret, L., G. Dambrine, S. Lepilliet, H. Happy, N. Chimot, V. Derycke, and J.-P. Bourgoin, “Gigahertz characterization of a single carbon nanotube,” *Appl. Phys. Lett.* 96 (042109) (2010).

Park, J.-Y., S. Rosenblatt, Y. Yaish, V. Sazonova, H. Usunel, S. Braig, T. A. Aria, P. W. Bower and P. L. McEuen, “Electron-phonon scattering in metallic single-walled carbon nanotubes,” *Nano Lett.* 4, 517–520 (2004).

Parkash, V. and A. K. Goel, “Quantum capacitance extraction for carbon nanotube interconnects,” in *Proceedings of the 20th International Conference on Microelectronics (ICM '08)*, pp. 292–295 (2008).

Plombon, J.J., K.P. O'Brien, F. Gstrein, and M. Dubin, “High-frequency electrical properties of individual and bundled carbon nanotubes,” *Appl. Phys. Lett.*, vol. 90, no. 6, p. 063 106, (2007).

Ponomarenko, V.V., “Frequency dependences in transport through a Tomonaga-Luttinger liquid wire,” *Phys. Rev. B*, vol. 54, no. 15, pp. 10 328–10 331 (1996).

Pop, E. and H. Dai., “Electrical and thermal transport in metallic single-wall carbon nanotubes on insulating substrates,” *J. Appl. Phys.* 101, 093710 (2007).

Portnoi, M.E., *et al.* “Terahertz applications of carbon nanotubes.” *Superlattices and Microstructures* 43, 399–407 (2008).

Postma, H.W.C., Jonge, M., Yao, Z. & Dekker, C. “Electrical transport through carbon nanotube junctions created by mechanical manipulation.” *Phys. Rev. B* 62, R10653–R10656 (2000).

Postma, H.W.C., T. Teepen, Z. Yao, M. Grifoni, C. Dekker, “Carbon nanotube single-electron transistors at room temperature,” *Science* 293, 76 (2001).

- Pozar, D. M., *Microwave Engineering*, 3 Ed., Wiley, New York, 2005.
- Prasher, R., P. Bhattacharya, and P.E. Phelan, “Thermal Conductivity of Nanoscale Colloidal Solutions (Nanofluids),” *Phys. Rev. Lett.* 94, 025901 (2005).
- Purewal, M. S., B.H. Hong, A. Ravi, B. Chandra, J. Hone, and P. Kim, “Scaling of Resistance and Electron Mean Free Path of Single-Walled Carbon Nanotubes,” *Phys. Rev. Lett.* 98 (18), 186808 (2007).
- Radushkevich, L.V. and Lukyanovich, V.M., *Russian Journal of Physical Chemistry* 26, 88-95 (1952).
- Rauf, H., T. Pichler, M. Knupfer, J. Fink, and H. Kataura, “Transition from a Tomonaga-Luttinger Liquid to a Fermi Liquid in Potassium-Intercalated Bundles of Single-Wall Carbon Nanotubes,” *Phys. Rev. Lett.* 93, 096805 (2004).
- Reese, M.O., D.F. Santavicca, D.E. Prober, A.B. True and C.A. Schmuttenmaer, “Niobium direct detectors for fast and sensitive terahertz spectroscopy,” *Rev. Sci. Instrum.* 78, 086111 (2007).
- Richards, P.L., “Bolometers for infrared and millimeter waves,” *J. Appl. Phys.* 76, 1 (1994).
- Rinzan, M., *et al.* “Carbon nanotube quantum dots as highly sensitive terahertz-cooled spectrometers,” *Nanoletters* 12, 3097–3100 (2012).
- Rodriguez-Morales, F., R. Zannoni, J. Nicholson, M. Fischetti, K.S. Yngvesson and J. Appenzeller, “Direct and heterodyne detection of microwaves in metallic single wall carbon nanotubes,” *Appl. Phys. Lett.* 89, 083502 (2006).
- Rutherglen, C., and P. Burke, “Nanoelectromagnetics: Circuit and electromagnetic properties of carbon nanotubes,” *Small*, vol. 5, no. 8, pp. 884–906 (2009).
- Rutledge, D.B. and M.S. Muha, “Imaging antenna arrays,” *IEEE Trans. Antennas Propagat.* 30, 535-540 (1982).
- Sablikov V.A. and B. S. Shchamkhalova, “Dynamic transport of interacting electrons in a mesoscopic quantum wire,” *J. Low Temp. Phys.*, vol. 118, no. 5/6, pp. 485–494 (2000).
- Saito R., M. Fujita, G. Dresselhaus, M. S. Dresselhaus, “Electronic structure of chiral graphene tubules” *Appl. Phys. Lett.* 60, 2204 (1992).
- Saito, R., Gene Dresselhaus, Mildred S. Dresselhaus, *Physical Properties of Carbon Nanotube*, Imperial College Press (1998).

Salahuddin, S., M. Lundstrom, and S. Datta, "Transport effects on signal propagation in quantum wires," *IEEE Trans. Electron Devices*, vol. 52, no. 8, pp. 1734–1742 (2005).

Sandler, N.P., C. de C. Chamon, and E. Fradkin, "Andreev reflection in the fractional quantum Hall effect," *Phys. Rev. B* 57, 12324 (1998).

Santavicca, D.F., A.J. Annunziata, M.O. Reese, L. Frunzio and D.E. Prober, "A far-infrared Fourier transform spectrometer with an antenna-coupled niobium bolometer," *Supercond. Sci. Technol.* 20, S398-S402 (2007).

Santavicca, D.F., M.O. Reese, A.B. True, C.A. Schmuttenmaer and D.E. Prober, "Antenna-coupled niobium bolometers for terahertz spectroscopy," *IEEE Trans. Appl. Supercond.* 17(2), 412 (2007).

Santavicca D.F., and D.E. Prober, "Terahertz resonances and bolometric response of a single-walled carbon nanotube," *Proc. 33rd Int. Conf. on IR, Millimeter and THz Waves* (2008).

Santavicca, D.F., J.D. Chudow, D.E. Prober, M.S. Purewal and P. Kim, "Energy loss of the electron system in individual single-walled carbon nanotubes," *Nano Lett.* 10, 4538 (2010).

Santavicca, D.F., J.D. Chudow, D.E. Prober, M.S. Purewal and P. Kim, "Bolometric and nonbolometric radio frequency detection in a metallic single-walled carbon nanotube," *Appl. Phys. Lett.* 98, 223503 (2011).

Santavicca, D.F., "Bolometric response of superconducting microbridges and single-walled carbon nanotubes" Doctoral Dissertation, Yale University (2009).

Sapmaz, S., C. Meyer, P. Beliczynski, P. Jarillo-Herrero, and L.P. Kouwenhoven, "Excited State Spectroscopy in Carbon Nanotube Double Quantum Dots," *Nano Lett.* 6 (7), pp 1350–1355 (2006).

Schmidt, T.L., Imambekov, A., and Glazman, L.I., "Spin-charge separation in one-dimensional fermion systems beyond Luttinger liquid theory," *Phys. Rev. B* 82, 245104 (2010).

Sedlmayr, N., P. Korell, and J. Sirker, "Two-band Luttinger liquid with spin-orbit coupling: Applications to monatomic chains on surfaces," *Phys. Rev. B* 88, 195113 (2013).

Sfeir, M.Y., F. Wang, L. Huang, C.C. Chuang, J. Hone, S.P. O'Brien, T.F. Heinz, and L.E. Brus, "Probing electronic transitions in individual carbon nanotubes by Rayleigh scattering," *Science* 306(5701), pp 1540–1543 (2004).

- Shi, W., *et al.* “Superconductivity in Bundles of Double-Wall Carbon Nanotubes.” *Scientific reports* 2 (2012).
- Shiraishi, M. and M. Ata, “Tomonaga–Luttinger-liquid behavior in single-walled carbon nanotube networks,” *Sol. State Commun.* 127, 215 (2003).
- Siegel, P.H., “Terahertz Technology,” *IEEE Trans. Micro. Theory Tech.* 50, 910-928 (2002).
- Smith, B.C., “Fundamentals of Fourier Transform Infrared Spectroscopy” CRC Press (2013).
- Sonin, E.B., “Tunneling into 1D and Quasi-1D Conductors and Luttinger-Liquid Behavior,” *Journal of Low Temperature Physics*, Volume 124, Issue 1-2, pp 321-334 (2001).
- Staliunas, K., “Spatial and temporal noise spectra of spatially extended systems with order–disorder phase transitions,” *Int. J. Bifurcation Chaos*, 11, 2845 (2001).
- Suzuki, S., *et al.* “Low-Acceleration-Voltage Electron Irradiation Damage in Single-Walled Carbon Nanotubes,” *Jpn. J. Appl. Phys.* 43 L1118 (2004).
- Svensson, J. & Campbell, E. E. B., “Schottky barriers in carbon nanotube-metal contacts,” *Journal of applied physics*, 110(11) (2011).
- Sydoruk, V.A., *et al.* “Low-frequency Noise in Individual Carbon Nanotube Field-Effect Transistors with Top, Side and Back Gate Configurations:Effect of Gamma Irradiation,” *Nanotechnology* 25 035703 (2013).
- Tanaka, T., K. Mori, E. Sano, B. Fugetsu, H. Yu, “The Luttinger-liquid behavior in single-walled carbon nanotube networks,” *Physica E* 44: 997–1001 (2012).
- Tang, Z.K., *et al.*, “Superconductivity in 4 angstrom single-walled carbon nanotubes” *Science* 292, 2462 (2001).
- Tang, H. and S. Ismail-Beigi, “Novel Precursors for Boron Nanotubes: The Competition of Two-Center and Three-Center Bonding in Boron Sheets,” *Phys. Rev. Lett.* 99, 115501 (2007).
- Tarkiainen, R., M. Ahlskog, J. Penttilä, L. Roschier, P. Hakonen, M. Paalanen, and E. Sonin, “Multiwalled carbon nanotube: Luttinger versus Fermi liquid” *Physical Review B* 64, 195412 (2001).
- Tarkiainen,R., *et al.*, “Multiwalled carbon nanotube: Luttinger versus Fermi liquid,” *Phys. Rev. B* 64, 195412 (2001).

- Tarkiainen, R., L. Roschier, M. Ahlskog, M. Paalanen, and P. Hakonen. "Low-frequency current noise and resistance fluctuations in multiwalled carbon nanotubes," *Physica E* 28, pages 57–65 (2005).
- Thorwart, M., M. Grifoni, G. Cuniberti, H. W. Ch. Postma, and C. Dekker, "Correlated Tunneling in Intramolecular Carbon Nanotube Quantum Dots," *Phys. Rev. Lett.* 89, 196402 (2002).
- Tobias, D., "1/f noise and Luttinger liquid phenomena in carbon nanotubes," Doctoral Dissertation, University of Maryland (2007).
- Tomonaga, S., "Remarks on Bloch's method of sound waves applied to many-Fermion problems," *Prog. Theor. Phys.*, vol5, no.4, pp544–569, (1950).
- Treacy, M.M.J., T.W. Ebbesen, and J.M. Gibson, "Exceptionally high Young's modulus observed for individual carbon nanotubes," *Nature*, 381, 678 (1996).
- Tseng Y.-C. and J. Bokor, "Characterization of the junction capacitance of metal-semiconductor carbon nanotube Schottky contacts," *Appl. Phys. Lett.* 96, 013103 (2010).
- Ulbricht, H., "Interaction kinetics of atoms and molecules on carbon nanotube surfaces." *Surface Science* 603.10: 1853–1862 (2010).
- Vijayaraghavan, A., "Applications of chirality-sorted individual single-wall carbon nanotube devices," *J. Mater. Chem.*, 22, 7083–7087 (2012).
- Vitusevich, S. and Gasparyan, F., "Low-Frequency Noise Spectroscopy at Nanoscale: Carbon Nanotube Materials and Devices" INTECH Open Access Publisher (2011).
- Wakeham, N., *et al.*, "Gross violation of the Wiedemann-Franz law in a quasi-one-dimensional conductor," *Nature Comm.* 2, 396 (2011).
- Wallace, P.R., "The Band Theory of Graphite," *Physical Review* 71, 622 (1947).
- Wang, X., *et al.*, "Fabrication of Ultralong and Electrically Uniform Single-Walled Carbon Nanotubes on Clean Substrates." *Nano Letters* 9 (9): 3137–3141 (2009).
- Wertime, T.A., *The Discovery of the Element Carbon*, Osiris, Vol. 11, The University of Chicago Press, (1954).
- Wiesbeck, W. *et al.*, "Basic Properties and Design Principles of UWB Antennas," *Proceedings of the IEEE*, Vol. 97, No. 2, (2009).
- Wong, H.-S.P., and D. Akinwande, *Carbon Nanotube and Graphene Device Physics*, Cambridge University Press (2011).

Yan, H., R. Xu, X. Hong, Y. Sun, L. Feng, *et al.*, “Zero-bias anomaly in one-dimensional ultrathin metallic nanowires,” *AIP Advances* 2, 032143 (2012).

Yao, Z., C. L. Kane, C. Dekker, “High-field electrical transport in single-wall carbon nanotubes” *Phys. Rev. Lett.* 84, 2941 (2000).

Yao, Z., Postma, H. W. Ch., Balents, L. & Dekker, C. Carbon nanotube intramolecular junctions. *Nature* 402, 273–276 (1999).

Yao, Z., C. Dekker, Ph. Avouris, “Carbon nanotube intramolecular junctions,” *Top. Appl. Phys.* 80, 147 (2001).

Yi, W. *et al.*, “Tunneling into Multiwalled Carbon Nanotubes: Coulomb Blockade and the Fano Resonance,” *Phys. Rev. Lett.* 91, 076801 (2003).

Yoneya, N., E. Watanabe, K. Tsukagoshi, and Y. Aoyagi, “Coulomb blockade in multiwalled carbon nanotube island with nanotube leads” *Appl. Phys. Lett.* 79, 1465 (2001).

Yu, Z. & Burke, P.J., “Microwave Transport in Metallic Single-Walled Carbon Nanotubes,” *Nano Lett.* 5, 1403 (2005).

Zhai, H.J., *et al.* “Observation of an all-boron fullerene,” *Nature Chemistry*, 6(8):727–731 (2014).

Zhang, Y., Z. Jiang, J. P. Small, M. S. Purewal, Y. –W. Tan, M. Fazlollahi, J. D. Chudow, J. A. Jaszczak, H. L. Stormer, and P. Kim, “Landau Level Splitting in Graphene in High Magnetic Fields” *Phys. Rev. Lett.*, 96, 136806 (2006).

Zhong, Z.H., N.M. Gabor, J.E. Sharping, A.L. Gaeta, P.L. McEuen, “Terahertz time-domain measurement of ballistic electron resonance in a single-walled carbon nanotube,” *Nat. Nanotechnol.* 3, 201 (2008).

Zoican-Loebick, C., R. Podila, J. Reppert, J. Chudow, F. Ren, G.L. Haller, A.M. Rao and L.D. Pfefferle, “Selective Synthesis of Subnanometer Diameter Semiconducting Single-Walled Carbon Nanotubes” *J. Am. Chem. Soc.*, 132 (32), pp 11125–11131 (2010).